

Appendix II: eRHIC Ring-Ring Design

G. Bassi, J. Beebe-Wang, J.S. Berg, M. Blaskiewicz, J.M. Brennan, K.A. Drees, A. Fedotov, W. Fischer, H. Hahn, Y. Hao, A. Hershcovitch, Y. Luo, C. Montag, R.B. Palmer, B. Parker, S. Peggs, V. Ptitsyn, S. Seletskiy, T. Shafan, V. Smaluk, K. Smith, S. Tepikian, F. Willeke, Q. Wu, W. Zhang

II.1 Ring-Ring Design Concept

The ring-ring design provides a path towards a machine design with a nominal luminosity in the $10^{33} \text{ cm}^{-2}\text{sec}^{-1}$ regime, upgradable to $10^{34} \text{ cm}^{-2}\text{sec}^{-1}$. The nominal ring-ring design described here uses existing technologies almost exclusively, thus greatly reducing the technical risk of the design. This results in reduced project cost, and a fast commissioning process, thus providing useable physics data after a short amount of time.

This design meets the requirements as outlined in the EIC White Paper [1]:

1. A center-of-mass energy from 20 to 140 GeV, realized by proton energies ranging from 50 to 275 GeV, and electron energies up to 18 GeV. This upper electron energy limit has been chosen to limit the total synchrotron radiation power to 10MW while still providing high luminosities at the highest center-of-mass energies. For center-of-mass energies of 30 GeV and above the electron energy is at least 5 GeV, as suggested by detector designers.
2. A luminosity of up to $1.1 \times 10^{33} \text{ cm}^{-2}\text{sec}^{-1}$, depending on center-of-mass energy.
3. Arbitrary spin patterns in the electron ring, realized by full-energy injection of polarized electron bunches with the desired spin direction (“up” or “down”) and frequent bunch replacement to ensure a high degree of polarization.
4. A transverse momentum acceptance for scattered protons from 200 MeV/c to 1.3 GeV/c in at least one transverse plane, realized by limiting the divergence angle of the proton beam at the interaction point (IP). Proton β -functions at the IP are chosen such that 50% of all scattered protons with a transverse momentum of 200 MeV/c can be detected by Roman Pots, which limits the achievable luminosity in this configuration. Increasing this lower limit of detectable transverse momentum allows us to decrease the horizontal β -function at the IP substantially, thus increasing the maximum luminosity by a factor of two or more.

The basic assumptions of this design are:

1. The electron ring is installed in the existing RHIC tunnel to minimize costly civil engineering. To prevent synchrotron radiation from the electron ring dipoles from hitting the superconducting RHIC magnets, the electron ring will be installed at a different elevation, most likely above the hadron ring.
2. There is only one interaction region, with one detector. Luminosities and beam-beam parameters quoted are based on a single beam-beam interaction per turn. This does not preclude later operations with two detectors, with the associated effect on luminosity.

3. Electron and hadron beams have identical beam sizes at the interaction point, with the horizontal beam size being larger than the vertical. At the interaction point the two beams intersect at a full crossing angle of 22 mrad in the horizontal plane. The resulting luminosity loss will be largely restored by crab cavities in the hadron beamline. Crab cavities in the electron ring are foreseen as well to avoid synchro-betatron resonances in the electron beam, though their pure geometric effect is negligible.
4. Hadron beam parameters are a moderate extrapolation of what has been achieved at RHIC, with the exception of the number of bunches which will be increased 3-fold, from 110 to 330.
5. A recirculating linac inside the RHIC tunnel serves as polarized full-energy injector for the electron storage ring. In the interest of risk reduction and cost saving we propose to use existing 1.3 GHz SRF technology virtually identical to the European XFEL, LCLS-2 at SLAC, and the proposed ILC.

Alternatively, a 650 MHz ERL-linac similar to that described in Section 2 but with more tightly packed cavities could be used as an injector, with 6 GV of total accelerating voltage installed in two adjacent straight sections of the RHIC tunnel. Two conventional recirculation loops would then suffice to reach 18 GeV. This injector would be upgradeable to the linac-ring scheme by adding additional recirculation loops to account for the lower maximum acceleration voltage achievable in CW energy-recovery mode, and wave guide dampers to deal with the increased average beam current. These upgrade modifications would have to be anticipated in the initial design.

6. The maximum electron beam-beam parameter does not exceed 0.1, a level that has been routinely achieved at the B-factories KEKB [2] and PEP-II [3] even with synchrotron radiation damping decrements that are ten times smaller than in eRHIC. The electron ring will be operated near the integer betatron resonance to minimize the beam-beam effect while simultaneously avoiding depolarizing spin resonances near the half-integer working point.
7. The RF power installed in the electron storage ring is 10 MW, corresponding to a linear synchrotron radiation power load of 4kW/m in the arcs. This linear load is more than a factor of 2 below the corresponding value for PEP-II [3] and KEKB [2].

To reduce overall cost, reusing components of the existing, decommissioned PEP-II storage rings at SLAC is envisioned. This includes all necessary quadrupole and sextupole magnets as well as all dipole correctors needed for the eRHIC electron storage ring, resulting in significant cost savings. This electron storage ring will be installed above the existing RHIC rings to minimize interference with the hadron ring. This is accomplished by sets of dipole magnets in the hadron ring, forming vertical dog legs between the low- β doublets and the arcs. Additional dipole magnets close to the IP and interspersed with the low- β quadrupoles serve to separate the hadron beam from the 4 mrad neutron cone that needs to be detected outside the central detector.

II.2 Beam Parameter and Luminosities

The luminosity of an electron-proton collider is given by:

$$\mathcal{L} = Hf \frac{N_p N_e}{4\pi\sigma_x\sigma_y} \quad (1)$$

where H is a factor reflecting the impact of the Hourglass effect and crossing angle. It is near unity if the bunch lengths are not large compared to the β^* s and the crossing angle is corrected with crab cavities. The factor f is the bunch repetition rate, and N_p and N_e are the numbers of protons and electrons per bunch, and σ_x and σ_y are RMS beam dimensions at the IP (the same for both protons and electrons), given by their geometric emittances $\epsilon_{x,y}$ and $\beta_{x,y}^*$:

$$\sigma_{x,y} = \sqrt{\epsilon_{p,x,y} \beta_{p,x,y}^*} = \sqrt{\epsilon_{e,x,y} \beta_{e,x,y}^*} \quad (2)$$

The repetition rate f is related to the average proton and electron beam currents $I_{p,e}$ by:

$$I_{p,e} = N_{p,e} q f \quad (3)$$

where q is the unit charge. For this ring-ring collider the current limits are taken as 1.35 Amps for the protons and 2.6 Amps for the electrons (based on the PEP-II [4] operation with 2.1 Amps at 9 GeV and 3.2 Amps at 3 GeV).

The numbers of particles per bunch $N_{p,e}$ are constrained by the beam-beam tune shifts $\xi_{x,y,e,p}$ (also known as beam-beam parameters) induced by each beam on the other. Their strength is given by:

$$\xi_{p,e,x,y} = \frac{r_{p,e}}{2\pi} \frac{N_{e,p}}{\epsilon_{p,e} \gamma_{p,e}} \frac{1}{1 + K_{x,y}} \quad (4)$$

where $r_{p,e}$ are the classical radii of the protons or electrons, $K_x = \sigma_x/\sigma_y$ and $K_y = \sigma_y/\sigma_x$.

Combining Equations (1) through (4), eliminating the emittances, gives:

$$\mathcal{L} \propto H \sqrt{\gamma_e \gamma_p I_e I_p (1 + K_x)(1 + K_y)} \left(\frac{\xi_{x,p} \xi_{y,p} \xi_{x,e} \xi_{y,e}}{\beta_{x,p}^* \beta_{y,p}^* \beta_{x,e}^* \beta_{y,e}^*} \right)^{1/4} \quad (5)$$

The beam-beam parameters ξ_p for the protons are bounded by beam stability considerations at $\xi_p \lesssim 0.015$, while the electrons in a ring-ring EIC can, with sufficient synchrotron radiation damping, have $\xi_e \lesssim 0.1$.

Equation (5) also shows that luminosity is increased with flat beams ($K_x = \sigma_x/\sigma_y \gg 1$). In this proposal K_x rises with energy to ≈ 20 . This is being achieved by employing β_x/β_y between 6 and 140, and also emittance ratios $\epsilon_x/\epsilon_y = 2.6$ for protons and up to 6 for electrons. For electrons, this asymmetry comes about naturally when the $x - y$ coupling is reduced. For the protons IBS also generates such an asymmetry, but initially horizontal noise is required.

Lastly, and crucially, Equation (5) shows that high luminosity requires low β^* s. These are limited by dynamic aperture from large chromaticity C contributions by the low- β quadrupoles given, very approximately, by:

$$C \approx \frac{L^*}{4\pi\beta^*} \quad (6)$$

where L^* is the distance from the interaction point (IP) to the low- β quadrupoles. So for low β^* , it is important to bring the focus as close to the IP as possible.

The β^* s, together with limits on the beam divergences, set requirements on the geometric emittances, to satisfy the relationship:

$$\sigma' = \sqrt{\frac{\epsilon}{\beta^*}} \quad (7)$$

The constraints on these divergences are described in the next section. Combining these with Equation (4) gives:

$$\beta^* \propto \frac{N}{\xi (1 + K) (\sigma')^2} \frac{1}{\gamma} \quad (8)$$

So for fixed divergences σ' , beam-beam tune shifts ξ , and particles per bunch N , the attainable β^* is lower, and the luminosity higher, at higher energies. It also follows from Equation (7) that, as β^* is lowered, the emittances must be reduced, and as the emittances are reduced, then the particles per bunch N must be reduced, and to maintain the currents I , the number of bunches must be increased.

The logic here is the same as that for $e^+ e^-$ colliders: luminosity is increased by using flat beams, low emittances, low- β focus magnets as close as possible to the IP, low charges per bunch, and many bunches. This use of more, smaller bunches, with fixed current, means that though the average backgrounds will be the same, per backgrounds per bunch crossing are reduced.

II.2.1 Baseline Parameters

Table 0-1 shows parameters for energies giving the highest luminosity, for both this baseline and also for the final upgrade. Both the β^* and emittances ϵ , of both the protons and electrons, are greater in the horizontal (x) than in the vertical plane (y), resulting in very flat beam profiles at the Interaction Point (IP). Unequal emittances are natural for the electrons in a storage ring, but for the protons, have to be generated by application of noise in the horizontal direction. Experimentally, it is known that such asymmetries have long lifetimes in RHIC.

As the center-of-mass energy increases, the proton energy is raised from 30 GeV to 275 GeV. The electron energy rises from 3.3 GeV to 10.1 GeV at a center-of-mass energy of 100 GeV, then stays constant except for the highest center-of-mass energy of 140 GeV where it is 17.8 GeV.

Over most of the center-of-mass energy range, the number of protons per bunch is chosen to be one half of that in the present RHIC, enabling longitudinal emittances also half of what has been achieved in RHIC. The number of electrons per bunch is chosen to keep the electron current below one half of 2.6 A, the projected maximum for the luminosity upgrade.

Table 0-1 gives parameters for a center-of-mass energy of 100 GeV which gives the highest luminosities for the baseline and upgrade. A full table of the baseline parameters is given in Table 0-2.

Figure 0-1 shows the emittances and β -functions vs the proton energies. All but β_{xp} fall linearly with energy as given by Equation (8), as do both the emittances. In contrast, β_{xp} rises with energy to limit the horizontal beam divergence.

Table 0-1 Parameters at energies giving the highest luminosities.

| | Baseline | | Upgrade | |
|---|----------|----------|---------|----------|
| | Proton | Electron | Proton | Electron |
| Center-of-Mass Energy [GeV] | 100 | | 100 | |
| Energy [GeV] | 250 | 10.1 | 250 | 10.1 |
| Bunches | 330 | | 1332 | |
| Particles/bunch [10^{10}] | 11.1 | 30.5 | 5.6 | 15.2 |
| Norm Horizontal Emittance [10^{-6} m] | 4.7 | 476 | 2.5 | 250 |
| Norm Vertical Emittance [10^{-6} m] | 1.8 | 76 | 0.11 | 5 |
| β_x [cm] | 566 | 416 | 283 | 208 |
| β_y [cm] | 4.2 | 7.4 | 2.1 | 3.7 |
| Horizontal Divergence [mrad] | 0.056 | 0.08 | 0.06 | 0.08 |
| Vertical Divergence [mrad] | 0.40 | 0.23 | 0.14 | 0.08 |
| Horizontal Beam-beam Parameter | 0.015 | 0.099 | 0.015 | 0.098 |
| Vertical Beam-beam Parameter | 0.002 | 0.033 | 0.006 | 0.095 |
| IBS Lifetime [hour] (long./transv.) | 9.8/11.5 | | 1.4/0.3 | |
| Q_{cool} for 100 m [nC] | N/A | | 38 | |
| Synch Radiation [MW] | 4.9 | | 9.9 | |
| Bunch Length [cm] | 8.0 | 0.8 | 4.0 | 0.8 |
| Hourglass [%] | 84 | | 86 | |
| Luminosity [10^{33} cm $^{-2}$ s $^{-1}$] | 1.1 | | 12.4 | |

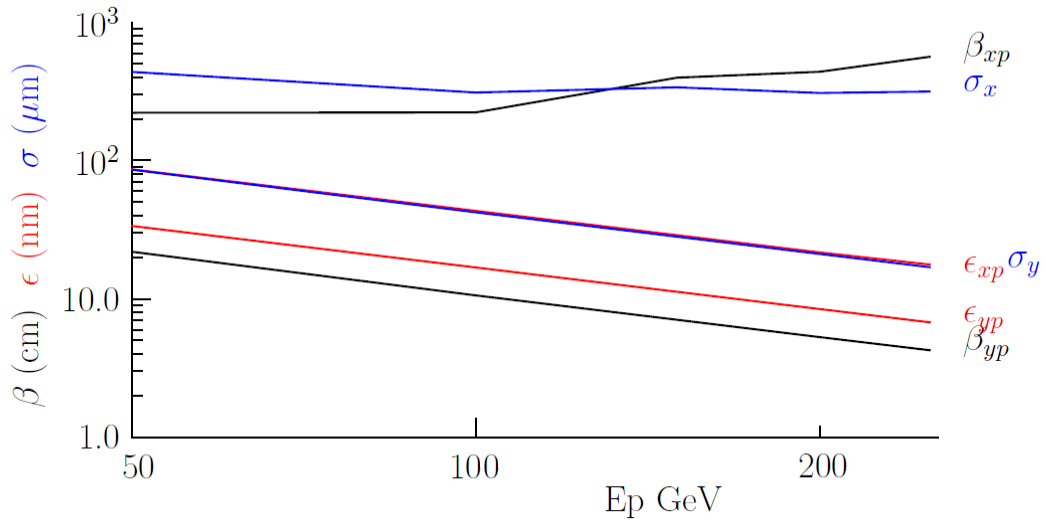


Figure 0-1 Emittances and β s vs. proton energy.

In order to enable detection of scattered protons with a minimum transverse momentum of 200 MeV/c, which at a beam energy of 275 GeV corresponds to a scattering angle of 730 μrad , the RMS divergence angle of the proton beam at the IP must not exceed one tenth of this minimum scattering angle, $\sigma' < 73\mu\text{rad}$. This limitation can be violated in one plane, provided the beam divergence in the other plane is reduced. Limiting the horizontal RMS beam divergence to 56 μrad allows detection of 50% of all scattered protons with a transverse momentum of 200 MeV/c despite the fact that the vertical RMS beam divergence is much larger. Taking into account the expected forward momentum distribution of the scattered protons in conjunction with the dispersion generated by dipoles in the interaction region this fraction is expected to become even larger, which may in turn allow for a larger horizontal RMS beam divergence, and therefore provide higher luminosity.

The IBS lifetimes for the baseline are all longer than 7 hours allowing reasonable efficiency of operation without any cooling. The parameters for the initial configuration therefore assume emittances as available from the current RHIC injection. To reach higher luminosities, however, magnetized electron cooling will be assumed, allowing smaller emittances, lower β s, and smaller bunches.

Figure 0-2 gives the luminosities vs center of mass energy for this baseline (in blue), together with those for the upgrade (in red), see Section II.15. Figure 0-2 in magenta shows the baseline luminosity with a horizontal divergence of 120 μrad .

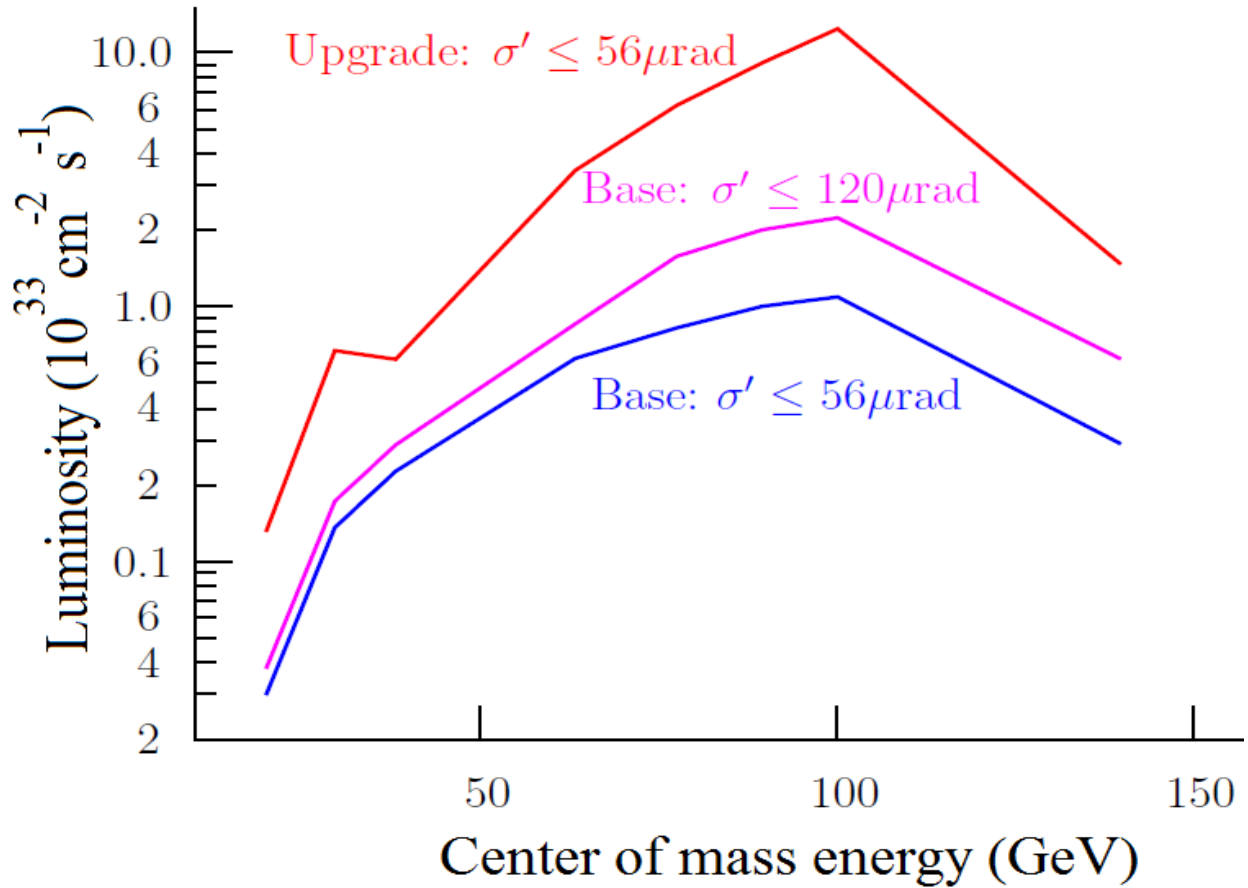


Figure 0-2 Luminosities vs. center-of-mass energy for the baseline with 56 μrad divergence in horizontal (in blue); The alternative with 120 μrad divergence in horizontal (in magenta); and the high luminosity upgrade (in red) with 56 μrad divergence.

Table 0-2 Collider Baseline Parameters.

| | E | N | N_b | ϵ_x (ϵ_{Nx}) | ϵ_y (ϵ_{Ny}) | ϵ_x/ϵ_y | β_x | β_y | σ_x | σ_y | σ_x/σ_y |
|------------|-------|---------------|-------|----------------------------------|----------------------------------|-------------------------|-----------|-----------|-------------------|-------------------|---------------------|
| | [GeV] | [10^{10}] | | [nm] ([μm]) | [nm] ([μm]) | | [cm] | [cm] | [μm] | [μm] | |
| \sqrt{s} | 20.0 | | | | | | | | | | |
| proton | 30 | 4.5 | 330 | 86.8 (2.8) | 56.3 (1.8) | 1.5 | 222.3 | 35.6 | 439 | 142 | 3.1 |
| electron | 3.3 | 22.0 | 330 | 53.1 (346) | 10.72 (70) | 5.0 | 365.6 | 184.0 | 441 | 140 | 3.1 |
| \sqrt{s} | 29.7 | | | | | | | | | | |
| proton | 50 | 9.0 | 330 | 86.8 (4.6) | 33.8 (1.8) | 2.6 | 222.3 | 22.0 | 439 | 86 | 5.1 |
| electron | 4.4 | 31.0 | 330 | 53.1 (457) | 10.72 (92) | 5.0 | 365.6 | 68.2 | 441 | 86 | 5.2 |
| \sqrt{s} | 38.2 | | | | | | | | | | |
| proton | 50 | 15.0 | 330 | 86.8 (4.6) | 33.8 (1.8) | 2.6 | 222.3 | 22.0 | 439 | 86 | 5.1 |
| electron | 7.3 | 30.9 | 330 | 53.1 (758) | 10.72 (153) | 5.0 | 365.6 | 68.2 | 441 | 86 | 5.2 |
| \sqrt{s} | 63.4 | | | | | | | | | | |
| proton | 100 | 15.0 | 330 | 43.4 (4.6) | 16.9 (1.8) | 2.6 | 223.5 | 10.6 | 311 | 42 | 7.4 |
| electron | 10.1 | 31.1 | 330 | 37.5 (738) | 5.76 (113) | 6.5 | 259.9 | 30.0 | 312 | 42 | 7.5 |
| \sqrt{s} | 77.7 | | | | | | | | | | |
| proton | 150 | 14.4 | 330 | 28.9 (4.6) | 11.3 (1.8) | 2.6 | 398.8 | 7.1 | 340 | 28 | 12.0 |
| electron | 10.1 | 30.3 | 330 | 30.6 (603) | 4.70 (93) | 6.5 | 379.4 | 16.4 | 341 | 28 | 12.3 |
| \sqrt{s} | 89.7 | | | | | | | | | | |
| proton | 200 | 12.3 | 330 | 21.7 (4.6) | 8.4 (1.8) | 2.6 | 440.2 | 5.3 | 309 | 21 | 14.6 |
| electron | 10.1 | 30.2 | 330 | 26.5 (522) | 4.24 (83) | 6.3 | 362.0 | 10.3 | 310 | 21 | 14.8 |
| \sqrt{s} | 100.2 | | | | | | | | | | |
| proton | 250 | 11.1 | 330 | 17.7 (4.7) | 6.8 (1.8) | 2.6 | 566.2 | 4.2 | 317 | 17 | 18.7 |
| electron | 10.1 | 30.5 | 330 | 24.2 (476) | 3.86 (76) | 6.3 | 416.4 | 7.4 | 318 | 17 | 18.8 |
| \sqrt{s} | 140.0 | | | | | | | | | | |
| proton | 275 | 14.7 | 330 | 17.4(5.1) | 6.1(1.8) | 2.8 | 664.1 | 4.4 | 339 | 16 | 20.7 |
| electron | 17.8 | 6.3 | 330 | 23.7(828) | 3.79(132) | 6.3 | 488.4 | 7.7 | 340 | 17 | 19.9 |

Collider Baseline Parameters (continued).

| | E | σ'_x | σ'_y | ξ_x | ξ_y | Min. p_t | ΔQ | σ_s | I | P_{SR} | HG | Luminosity |
|------------|-------|-------------|-------------|---------|---------|------------|------------|------------|------|----------|-----|--|
| | [GeV] | [mrad] | [mrad] | | | [MeV] | | [cm] | [A] | [MW] | [%] | [$10^{33} \text{ cm}^{-2} \text{ s}^{-1}$] |
| \sqrt{s} | 20.0 | | | | | | | | | | | |
| proton | 30 | 0.20 | 0.40 | .015 | .007 | 59 | .035 | 13.0 | 0.19 | | 91 | 0.03 |
| electron | 3.3 | 0.12 | 0.08 | .045 | .071 | | .000 | 0.8 | 0.91 | 0.0 | | |
| \sqrt{s} | 29.7 | | | | | | | | | | | |
| proton | 50 | 0.20 | 0.39 | .014 | .007 | 99 | .025 | 13.0 | 0.37 | | 90 | 0.14 |
| electron | 4.4 | 0.12 | 0.13 | .074 | .072 | | .000 | 0.8 | 1.28 | 0.2 | | |
| \sqrt{s} | 38.2 | | | | | | | | | | | |
| proton | 50 | 0.20 | 0.39 | .014 | .007 | 99 | .042 | 13.0 | 0.62 | | 90 | 0.23 |
| electron | 7.3 | 0.12 | 0.13 | .074 | .072 | | .000 | 0.8 | 1.28 | 1.4 | | |
| \sqrt{s} | 63.4 | | | | | | | | | | | |
| proton | 100 | 0.14 | 0.40 | .014 | .005 | 139 | .011 | 12.0 | 0.62 | | 86 | 0.63 |
| electron | 10.1 | 0.12 | 0.14 | .080 | .071 | | .000 | 0.8 | 1.29 | 5.0 | | |
| \sqrt{s} | 77.7 | | | | | | | | | | | |
| proton | 150 | 0.09 | 0.40 | .015 | .003 | 128 | .006 | 10.0 | 0.60 | | 88 | 0.83 |
| electron | 10.1 | 0.09 | 0.17 | .099 | .054 | | .000 | 0.8 | 1.25 | 4.9 | | |
| \sqrt{s} | 89.7 | | | | | | | | | | | |
| proton | 200 | 0.07 | 0.40 | .015 | .003 | 140 | .003 | 9.0 | 0.51 | | 86 | 1.01 |
| electron | 10.1 | 0.09 | 0.20 | .099 | .043 | | .000 | 0.8 | 1.25 | 4.9 | | |
| \sqrt{s} | 100.2 | | | | | | | | | | | |
| proton | 250 | 0.06 | 0.40 | .015 | .002 | 140 | .002 | 8.0 | 0.46 | | 84 | 1.10 |
| electron | 10.1 | 0.08 | 0.23 | .099 | .033 | | .000 | 0.8 | 1.26 | 4.9 | | |
| \sqrt{s} | 140.0 | | | | | | | | | | | |
| proton | 275 | 0.05 | 0.37 | .003 | .000 | 141 | .002 | 8.0 | 0.61 | | 85 | 0.29 |
| electron | 17.8 | 0.07 | 0.22 | .076 | .023 | | .000 | 0.8 | 0.26 | 10.0 | | |

RF and IBS Baseline for 330 bunches, an RF frequency of 394 MHz, and a crab cavity frequency of 336 MHz.

| γ | Volts | ϵ_{xN} | ϵ_{yN} | σ_z | dp/p | $eV\text{-sec}$ | N_p | τ_{\parallel} | τ_{\perp} | Q_{100m} | V_1 | HG | Lum. |
|----------|-------|-------------------|-------------------|------------|---------------|-----------------|---------------|--------------------|----------------|-------------------|-------|-----|---------------|
| | [MV] | [μm] | [μm] | [cm] | [10^{-4}] | [eVsec] | [10^{11}] | [hr] | [hr] | [nC] | [MV] | [%] | [10^{33}] |
| 32 | 1.35 | 2.77 | 1.80 | 13 | 14.0 | 0.4 | 0.5 | 8.6 | 14.4 | 0.79 ^a | 3.21 | 91 | 0.03 |
| 53 | 3.94 | 4.62 | 1.80 | 13 | 14.0 | 0.6 | 0.9 | 12.4 | 16.1 | 3.4 ^a | 4.14 | 90 | 0.14 |
| 53 | 3.94 | 4.62 | 1.80 | 13 | 14.0 | 0.6 | 1.5 | 7.4 | 9.7 | 5.6 ^a | 4.14 | 90 | 0.23 |
| 107 | 5.02 | 4.62 | 1.80 | 12 | 9.5 | 0.7 | 1.5 | 7.2 | 10.0 | 30 ^b | 5.85 | 86 | 0.63 |
| 160 | 8.11 | 4.62 | 1.80 | 10 | 8.1 | 0.8 | 1.4 | 7.6 | 9.6 | 66 ^b | 5.36 | 88 | 0.83 |
| 213 | 8.95 | 4.62 | 1.80 | 9 | 6.6 | 0.8 | 1.2 | 7.3 | 10.4 | 127 ^c | 5.89 | 86 | 1.01 |
| 266 | 13.80 | 4.72 | 1.80 | 8 | 6.5 | 0.8 | 1.1 | 9.8 | 11.5 | 151 ^c | 5.81 | 84 | 1.10 |
| 293 | 15.20 | 5.09 | 1.80 | 8 | 6.5 | 0.9 | 1.5 | 8.9 | 9.9 | 232 ^c | 5.62 | 85 | 0.29 |

Note:

- a. Non magnetic cooling possible with $\approx 1/3$ charge
- b. Magnetic cooling possible
- c. Only Coherent Electron Cooling possible

II.2.2 Interaction Region (IR)

For high luminosity it is necessary to have a small β^* , but for stability and dynamic aperture reasons, a high maximum β , and associated chromaticity, should be avoided. Without magnets, the β rises as L^2/β^* , where L is the distance from the IP. It is thus important to start the focusing as close to the IP as possible. This is most important for the protons with their lower β^* , but also for the electrons. Thus, to keep both maximum β s low, the electron quadrupoles are interleaved with those for the protons.

Figure 0-3 shows the horizontal layout of the IR with 22 mrad beam crossing angle. The lines in red show 10σ proton beam and 15σ electron beam envelopes, respectively. The magnet locations and apertures are also shown. The lines are those with 250 GeV protons and 20 GeV electrons, while the dashes are for 50 GeV protons and 5 GeV electrons. The magenta lines define the outline of the 4 mrad cone in which neutrons can propagate from the IP to the shown neutron detector. The magnet apertures are such as to allow 50% of 5.2 mrad, 1.3 GeV/c transverse momentum protons from the IP to be detected using 'Roman pots' in the free space between Q2 and Q3.

The two beam lines are relatively close, so the early magnets of both beams need to have limited outside radial dimensions, outside of which the fields must be low. The magnets use active shielding as demonstrated at BNL for an ILC IR application [5] (see Figure 0-4a and Figure 0-4b) or, for the dipole B1, a yoke with a hole in it for electrons (see Figure 0-4d).

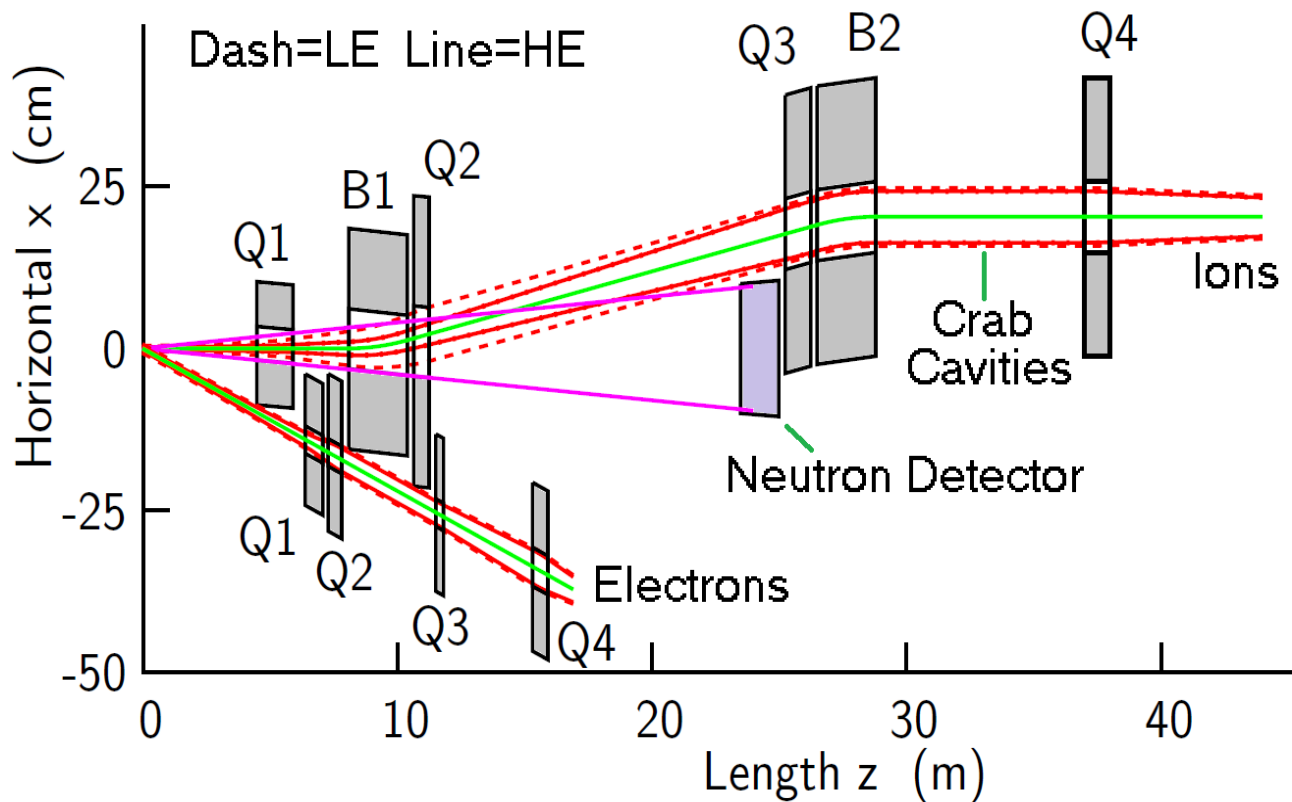


Figure 0-3 Layout of IR magnets and other components.

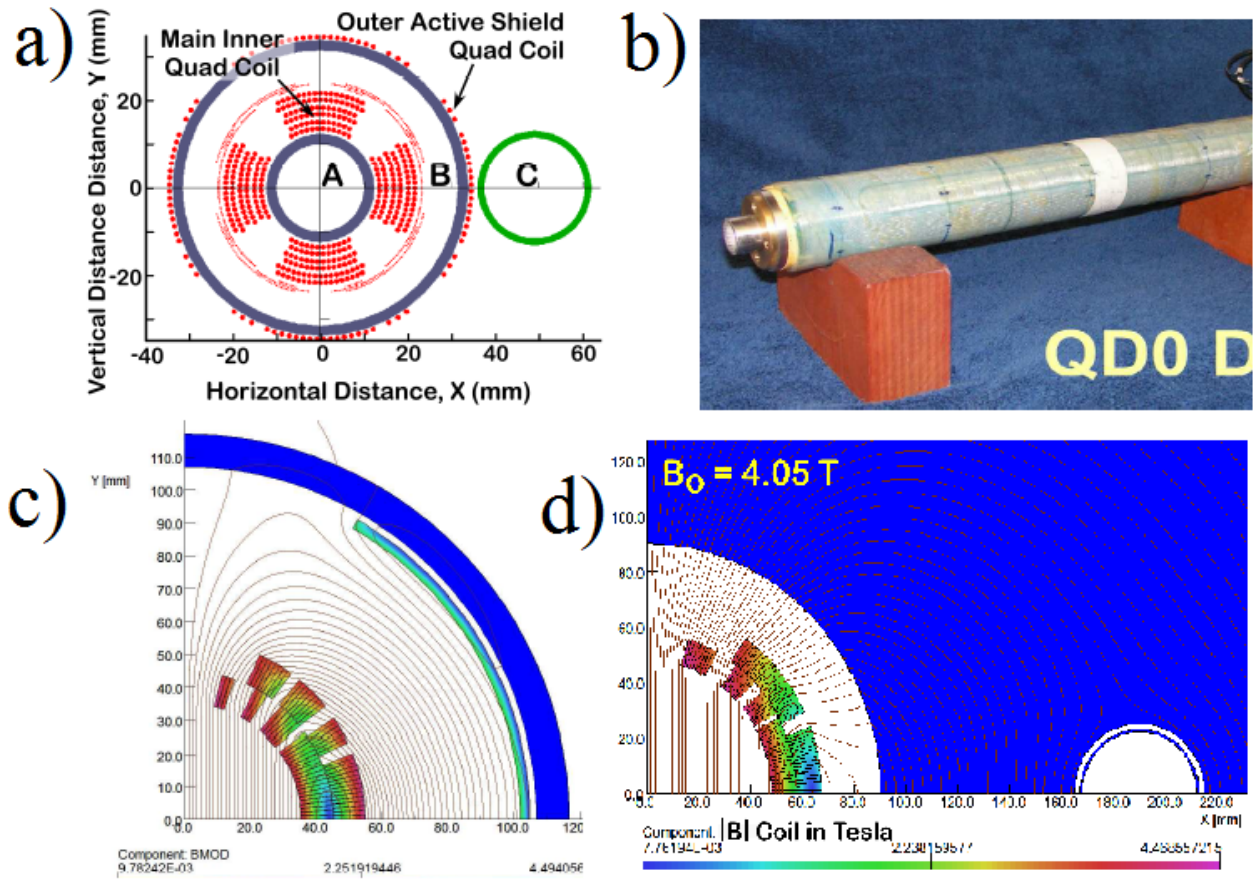


Figure 0-4 Actively shielded magnets: a) Section of a quadrupole with active shielding for an ILC prototype; b) The tested prototype; c) Conceptual design of a dipole with active shielding outside for this Ring-ring IR application; d) Concept for a possibly simpler design of the dipole B1.

In the ILC prototype quadrupole, all coils were direct-wound. In our case, where the fields are higher, it is proposed to wind the primary coils using two layers of Rutherford cable, while the active shielding coils, with lower currents but more acute placement requirements, would use direct winding (see Figure 0-4c).

Table 0-3 gives the dimensions, fields and gradients for 250 GeV proton IR magnets for the large acceptance baseline. All dipoles and quadrupole fields are 4 Tesla or less, making their design, besides their shielding, relatively straightforward.

Figure 0-5 shows β_x (red) and β_y (blue) for the protons versus distance from the IP. The lines are those present at 250 GeV, the dashes are for 50 GeV. In both cases the β s are essentially constant between 25 and 35 m where the crab cavities are located. At 250 GeV this β equals 800 m, but is only approximately 180 m at 50 GeV. This is done to keep the beam size less than or equal to that at 250 GeV, so as not to increase the required crab cavity gap. Since the crab cavity voltage is proportional to the square root of β^* the crab voltage is still lower at 50 GeV. The reduction in β^* is achieved by powering Q2 and adjusting Q3.

Table 0-3 Parameters of IR magnets for Baseline 250 GeV protons.

| Magnet | Start x [m] | Length [m] | Inside Rad. [cm] | B [Tesla] | Grad [Tesla/m] |
|--------|---------------|------------|------------------|-------------|----------------|
| Q1 | 4.5 | 1.41 | 2.81 | (3.98) | 141.7 |
| B1 | 8.11 | 2.3 | 4.65 | 4.0 | |
| Q2 | 10.66 | 0.6 | 5.44 | (1.50) | 27.5 |
| Q3 | 25.26 | 1.0 | 4.49 | (1.54) | 34.3 |
| B2 | 26.51 | 2.3 | 4.49 | 4.00 | |
| Q4 | 37.0 | 1.0 | 4.47 | (1.42) | 31.7 |

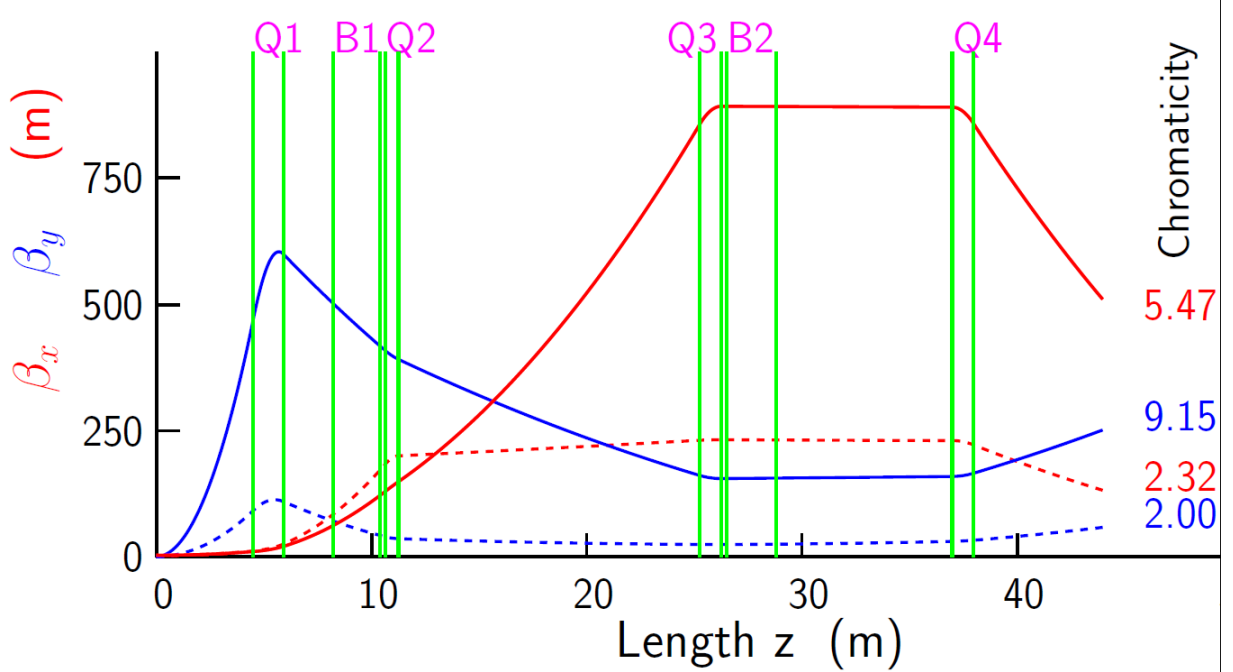


Figure 0-5 Hadron β s vs length in the IR. The indicated chromaticities are only computed from the IP to the end shown.

II.3 Lattice and Optics

II.3.1 Modifications to RHIC

RHIC Injection Kickers

The 28 MHz bunching frequency necessitates new injection kickers in RHIC. Take a full bunch length of $T_b = 15$ ns, a bunch spacing of $T_s = 35$ ns. We assume a strip line kicker of length $L = 1.25$ m. If we assume the kicker pulse starts just as the previous bunch passes and hits its peak just before the injected bunch then the rise time satisfies:

$$T_r \leq T_s - T_b - 2L/c = 12 \text{ ns} \quad (9)$$

We take a rise time of 10 ns which has been achieved in practice. The fall time is relaxed since we will inject along the bunch train. A flattop voltage for the pulser of 30 kV is reasonable. We take a deflection angle of 0.002 rad, as is now the case. If we take a stripline kicker of characteristic impedance 50 Ω and a horizontal plate spacing of 5 cm then the current in each plate will be 600 A. For a 24 GeV proton beam we need a total of 16 such modules. The active length of 19.2 m does not include bellows, pumping ports etc., so a total length of 25 m is taken for the injection kicker. The present injection area in the RHIC tunnel does not allow for a 25 m kicker. The proposed solution is to build a section of beam line and transport the 24 GeV beam to the 8 o'clock straight section and inject upstream or downstream of the experiment. We will need to make sure the injected beam cannot damage the experimental detector during machine setup. For instance we could use movable collimators, which are retracted after injection and before ramping. The main focus of R&D is to make sure the injection pulsers can be manufactured and that their reliability and lifetime are adequate.

II.3.2 Electron Ring Lattice

The Electron Storage Ring for the Ring-Ring eRHIC will make as much use of the PEP-II magnets as possible to reduce the cost. The available PEP-II magnets are shown in Table 0-4 from the document [3]. From this table, for a 20 GeV beam, the strength limit for the quadrupoles is 0.3 m⁻²; for 18 GeV beam, the strength limit is higher.

So far, the electron ring has been designed for a beam energy of 20 GeV, requiring the strongest magnetic fields. Re-matching this lattice for lower energies is relatively straightforward since constraints on magnet strengths are more relaxed due to the lower beam rigidity.

To provide electron-proton collisions over the entire center-of-mass energy range from 20 to 140 GeV, proton energies from 50 to 275 GeV are required. The resulting change in the revolution frequency of the protons will be compensated by adjusting the circumference of the electron ring. This is accomplished by separating beamlines in parts of one arc that increase the pathlength for the electron beam accordingly.

Table 0-4 The available PEP-II quadrupoles and sextupoles from both the LER and HER rings. The Pole Tip field B should be kept below 1 Tesla, since these are warm magnets. Their maximum operating field per magnet type in PEP-II is shown as well.

| Magnet Type | Radius | Pole Tip B | Gradient | Mag. Length | Strength | Count | Machine |
|-------------|--------|--------------|---------------------|-------------|---------------------|-------|---------|
| Quadrupoles | [cm] | [Tesla] | [T/m] | [cm] | [1/m ²] | | |
| 4Q17 | 4.999 | 0.960 | 19.210 | 43.0022 | 0.28795 | 280 | LER |
| 4Q18 | 4.999 | 0.588 | 17.720 | 45.0088 | 0.17643 | 70 | HER |
| 4Q22 | 4.999 | 0.490 | 9.800 | 54.9910 | 0.14690 | 94 | HER |
| 4Q28 | 4.999 | 0.308 | 6.160 | 72.9996 | 0.09234 | 22 | HER |
| 4Q40 | 4.999 | 0.490 | 9.800 | 99.9998 | 0.14690 | 40 | LER,HER |
| 4Q60 | 4.999 | 0.369 | 7.370 | 156.718 | 0.11047 | 4 | HER |
| Sextupoles | [cm] | [Tesla] | [T/m ²] | [cm] | [1/m ³] | | |
| 10SF | 5.999 | 0.270 | 150.104 | 25.50414 | 2.25000 | 72 | HER |
| 10SD | 5.999 | 0.270 | 150.104 | 25.50414 | 2.25000 | 72 | HER |
| 4.5S | 5.999 | 0.335 | 186.130 | 25.50414 | 2.79002 | 152 | LER |

The ARC includes 16 FODO cells shown below using the four 4Q17 PEP-II quadrupoles and two sextupoles. The FODO cells are about 90° phase advance horizontal to reach the emittance of 24 nm. This requires a quadrupole longer than the 4Q17 to keep the pole tip field below 1 Tesla. Since, according to the Table 0-4, 4Q17 is the most populous quadrupole, two are used to get the required strength. Ideally, we would have used 4Q29, but there are not enough available for all the ARCs. Space is left for BPMs, orbit correctors, etc. If more space is needed, the dipole length will be affected which can lead to higher electron radiation at 18 GeV, thus, could effect the luminosity. Figure 0-6 shows a FODO cell.

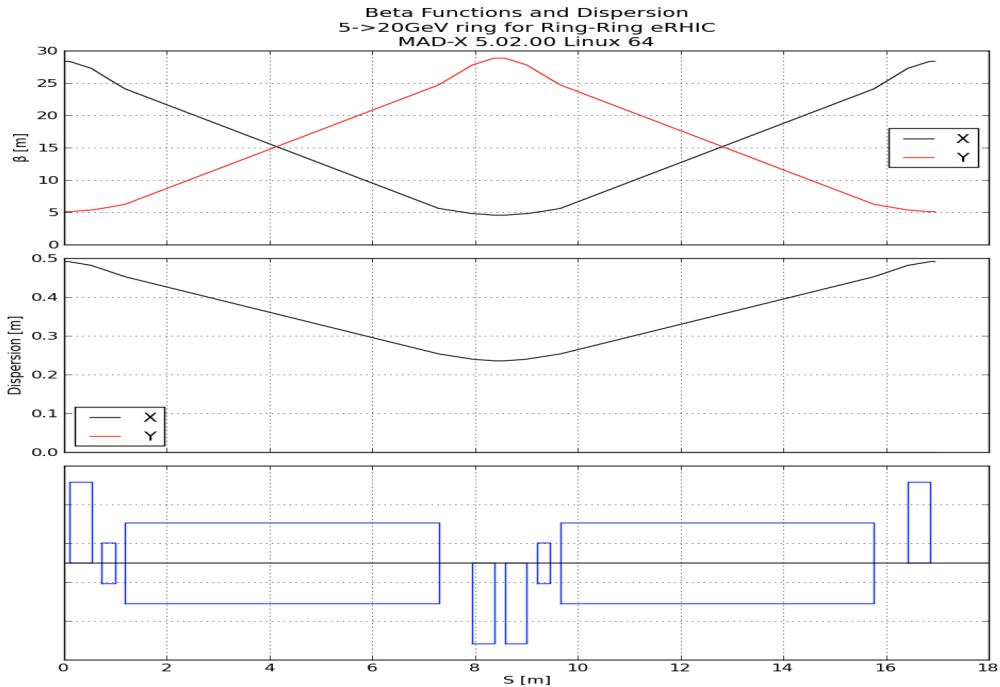


Figure 0-6 The FODO cell used in the ARCs. This cell consists of 2 PEP-II sextupoles, four PEP-II quadrupoles (type 4Q17) and two dipoles of length 6.1067 m long. The total length of the cell is 16.954 m.

The ends of the ARC consist of the dispersion suppressors. Geometrically, they are all identical to be able to collide at all six existing RHIC IPs. Furthermore, there is space provided for the solenoids with the proper amount of bending magnets for the spin rotators. Figure 0-7 shows a schematic of a spin rotator.

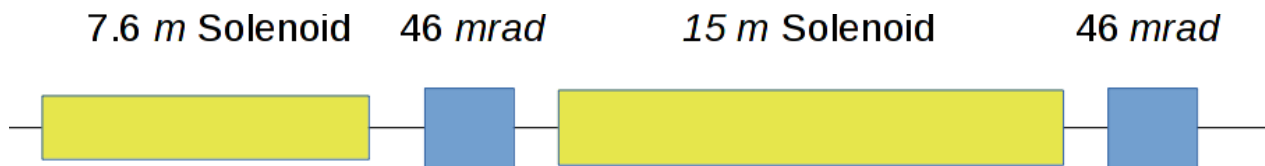


Figure 0-7 Schematic of the spin rotator section consisting of two solenoid sections and two bending magnet sections.

The lengths of the solenoids are chosen so that the maximum magnetic field required is 7 Tesla. The settings for the magnetic fields of the solenoids to achieve longitudinal polarization of the electron beam depend on the beam energy.

The solenoid sections contain 7 quadrupoles and 4 skew quadrupoles. They are arranged to give a transfer matrix of:

$$M = \begin{pmatrix} \omega_{11} & \omega_{12} & 0 & 0 \\ \omega_{21} & \omega_{22} & 0 & 0 \\ 0 & 0 & \omega_{33} & \omega_{34} \\ 0 & 0 & \omega_{43} & \omega_{44} \end{pmatrix} \quad (10)$$

with

$$\omega_{12} = (\omega_{11}\omega_{22} - 1)/\omega_{21} \quad (11)$$

and

$$\omega_{34} = (\omega_{33}\omega_{44} - 1)/\omega_{43} \quad (12)$$

where the 11 quadrupoles are adjusted to produce a transfer matrix M . The six variables ω_{11} , ω_{21} , ω_{22} , ω_{33} , ω_{43} and ω_{44} for each solenoid section are determined by the final optimization of the full IR.

Another requirement to preserve the spin polarization of the electron beam using the solenoids is related to the dispersion through the solenoids. Figure 0-8 shows both solenoids with their ends referenced. Using these references, the following requirements for the dispersion are given as

$$\begin{aligned} 1.4 &= 14.1D'_{x_1} + 11.5D'_{x_2} - 8.2D'_{y_2} - 18.0D'_{x_3} - 25.4D'_{y_3} - 18.0D'_{x_4} + 25.6D'_{y_4} \\ 0.4 &= 37.6D'_{x_3} - 12.9D'_{x_4} - 35.4D'_{y_4} \end{aligned} \quad (13)$$

where D' is the derivative of dispersion inside the solenoid edge. Denoting \widetilde{D}' as the derivative of dispersion from outside the solenoid edge (i.e. MADX [7] value), we have:

$$\begin{pmatrix} D_x \\ D'_x \\ D_y \\ D'_y \end{pmatrix} = \begin{pmatrix} \widetilde{D}_x \\ \widetilde{D}'_x + K_s \widetilde{D}_y / 2 \\ \widetilde{D}_y \\ \widetilde{D}'_y - K_s \widetilde{D}_x / 2 \end{pmatrix} \quad K_s = \frac{B_{sol}}{B\rho} \quad (14)$$

The coefficients in these constraints are energy dependent, assuming 20 GeV beam. In the IRs with no experiments, where no spin rotation is required, the solenoid sections consist only of regular quadrupoles. Also, the length is the same to preserve the geometry.

Figure 0-9 shows a solenoid section with the Ripken-Mais [6] β -functions. The final IR is shown in Figure 0-10.

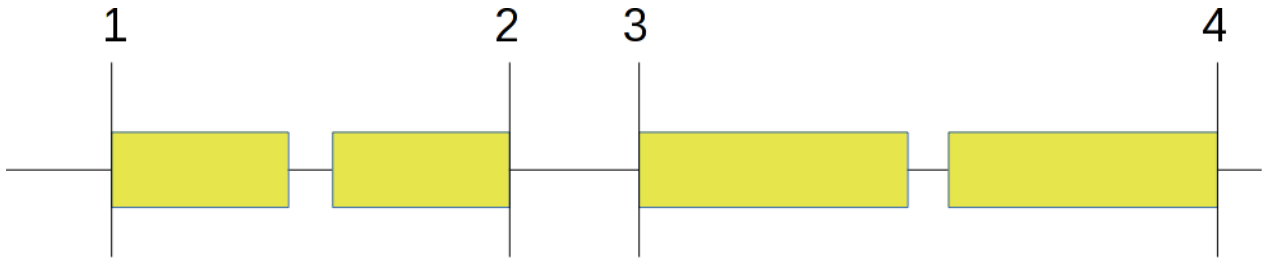


Figure 0-8 A schematic of only the solenoids in an IR. The two solenoids are split into two and their ends are referenced as 1, 2, 3 and 4.

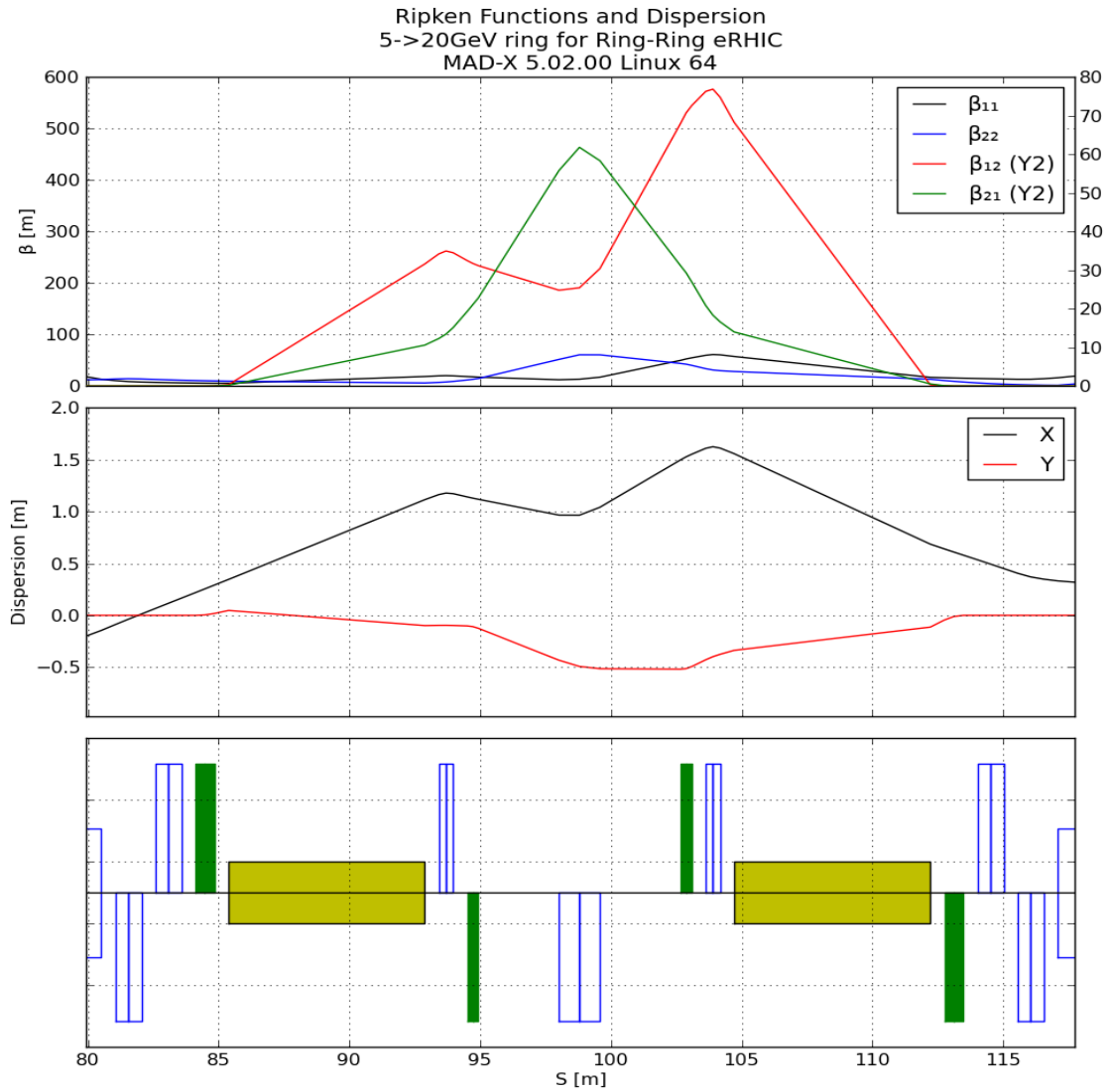


Figure 0-9 The Ripken-Mais functions for a solenoid section. The solenoid is split in two denoted in yellow. The coupling from the solenoid is corrected using 4 skew quadrupoles (green). Seven other quadrupoles are used to simplify the beam transfer matrix.

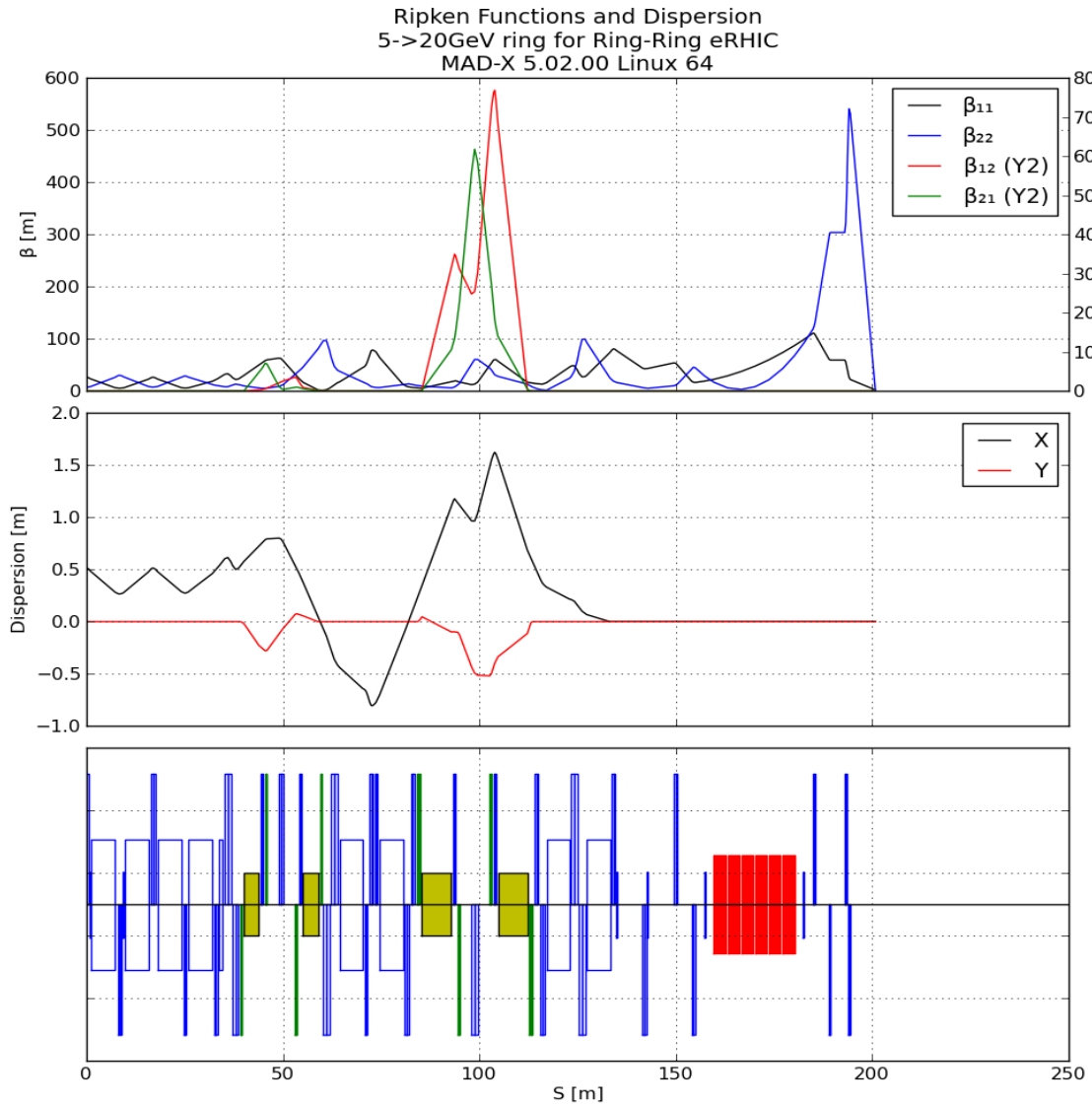


Figure 0-10 The colliding IR optimized for low $\beta^*=(2.035, 0.077)$ m with a flat beam. The two solenoid sections are shown. The included dipoles provide 23 mrad bending. The red sections are possible locations for RF cavities.

The other IRs (IP10, IP12, IP2 and IP4) will be similar except the solenoid sections will be replaced with regular quadrupoles only. An example of one of these sections is shown in Figure 0-11. All are identical geometrically to match the existing Blue RHIC ring IPs. A full ring is shown in Figure 0-12 and Figure 0-13. Much work still needs to be done:

- Adding the super bend wigglers (see Section II.3.3) in the ARCs.
- Adding the orbit correctors, BPMs etc. and checking for sufficient space.
- Correction for chromatic effects and amplitude dependent tune effects without exceeding the strengths of the PEP-II sextupoles.
- Designing for the lower energies 5 GeV, 10 GeV and perhaps others.
- Adding a Robinson-Wiggler with a non-zero dispersion utility.
- Tracking to check dynamic aperture (see Section II.5) and polarization (II.13).

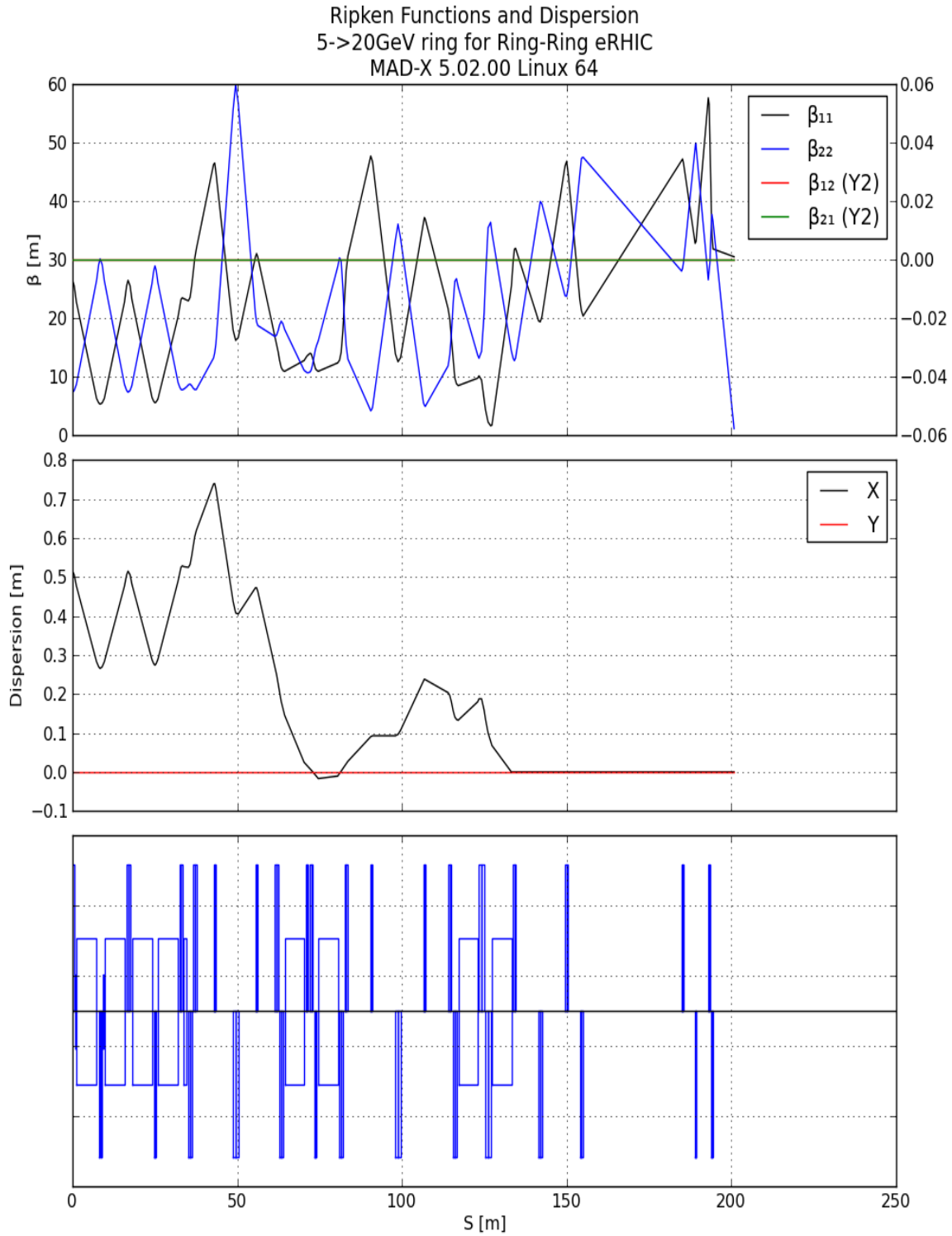


Figure 0-11 A non-colliding IR that does not have a spin rotator section. This utility section has space for RF cavities, amplitude dependent tune correction sextupoles, etc. Some can be tuned for non-zero dispersion and include Robinson-Wigglers, etc.

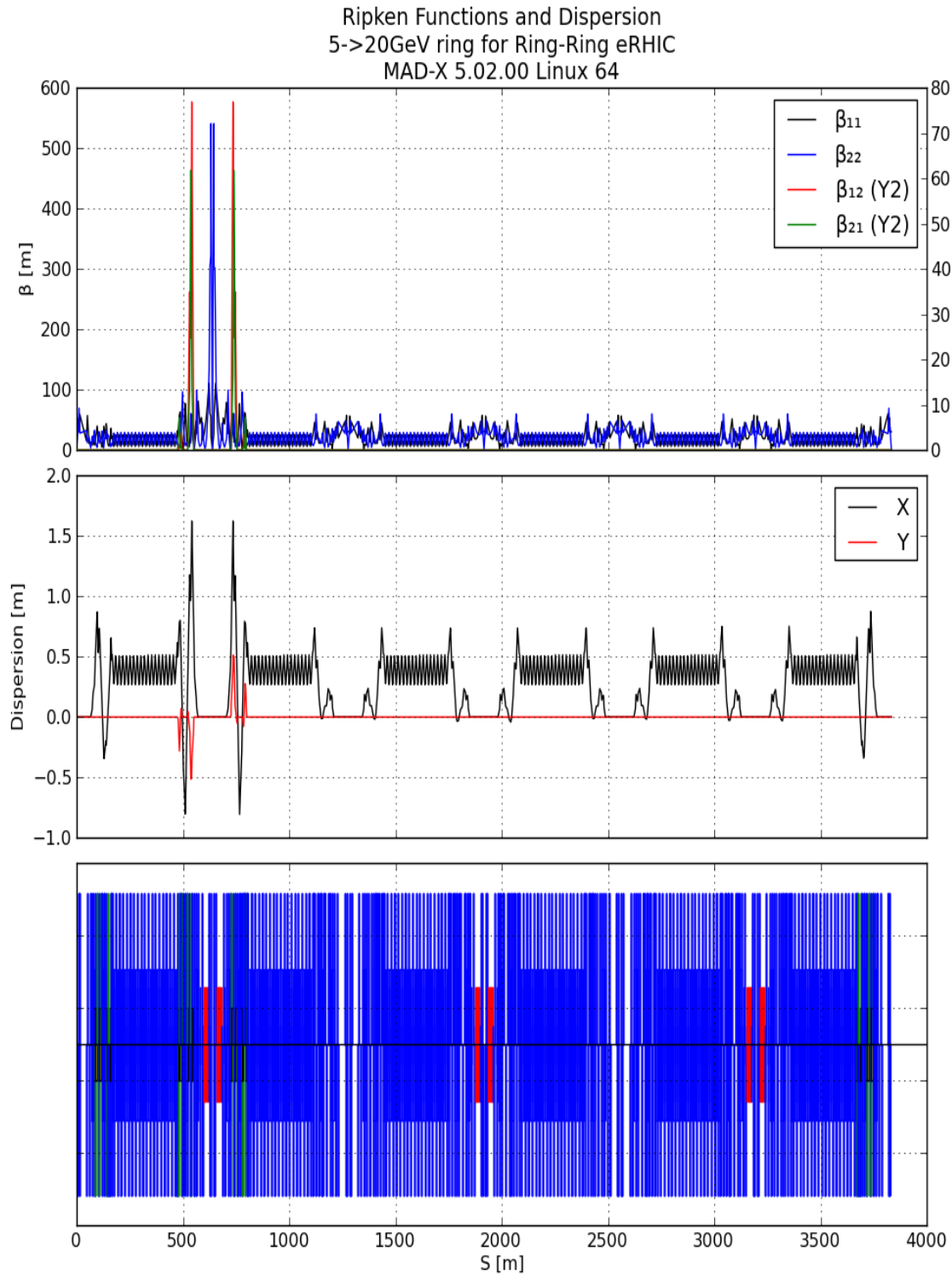


Figure 0-12 A full electron storage ring without the RF cavities being on and no electron radiation. Tunes = (46.12, 45.08), natural chromaticity = (-67.79, -92.52), $\gamma_T = 44.802$ and $\beta_{\max} = (110.7, 540.8)$.

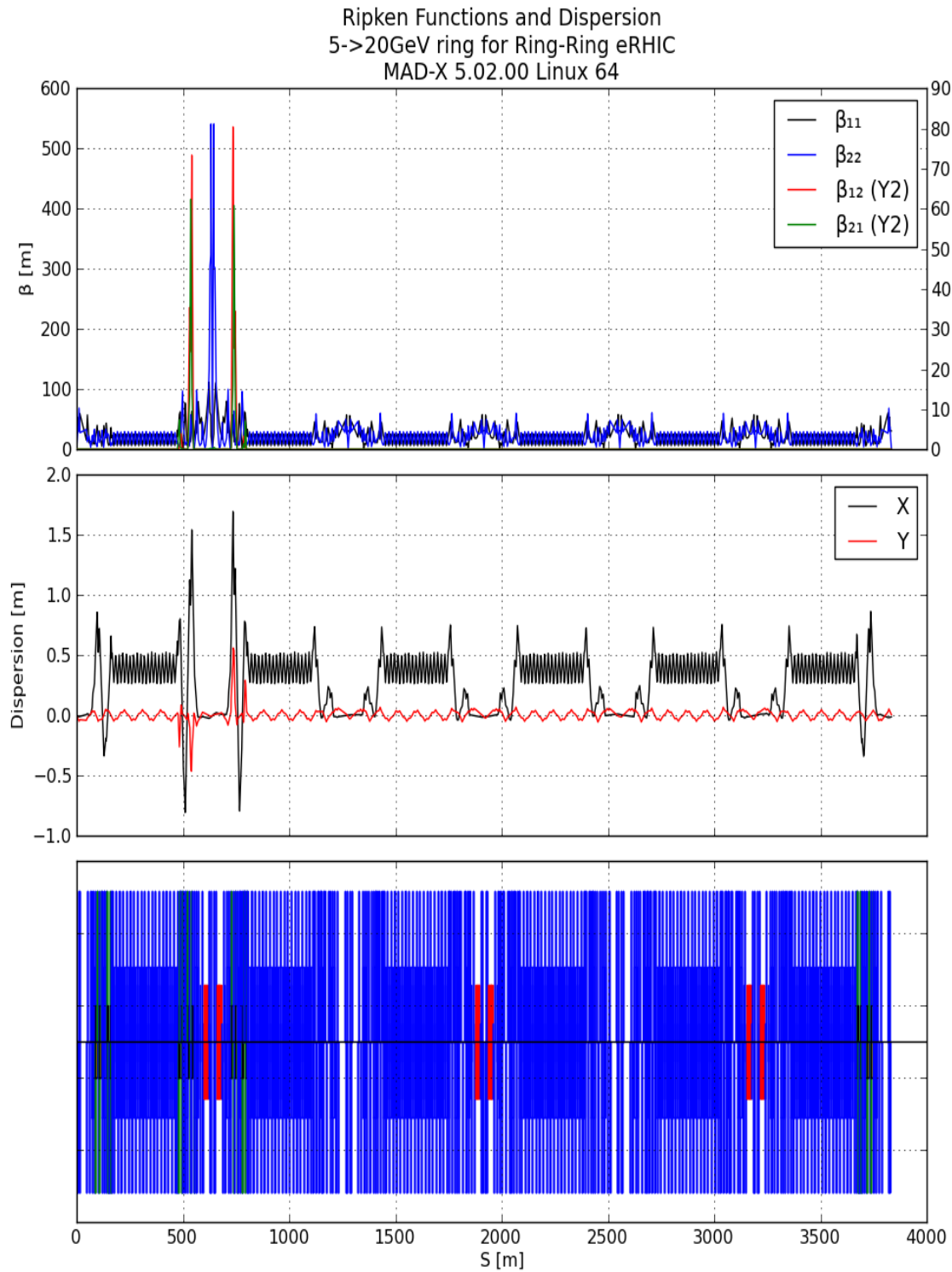


Figure 0-13 Full ring with 36 RF cavities each at 2 MV and electron radiation on at 20 GeV. The Horizontal emittance is 24.81 nm. The energy loss per turn from radiation is 55.164 MeV.

II.3.3 Split Arc Dipoles for Radiation Production at Lower Energies

Radiation damping allows the electron beam to have a large beam-beam tune shift. While sufficient radiation to allow a large beam-beam tune shift is produced at higher energies, if the dipole fields for a high energy lattice are simply scaled down for lower energies, the radiation damping is not large enough to give a substantial increase in beam-beam tune shift.

Our solution to this is to place three dipoles, instead of a single dipole, between the arc quadrupoles. At high energies, all three dipoles have the same field. At lower energies, the central dipole will have a high field, higher than even the field for the high energy beam. This will increase radiation production for the low energy beam. Figure 0-14 shows the dipole configuration and orbits at different energies. There are three costs to this scheme: higher dipole fields are required; the orbits are different for each energy, requiring wider dipoles; and the additional drifts between dipoles reduce the dipole packing fraction, leading to more radiation production at higher energies.

The design requirements for the split arc dipoles are given in Table 0-5. The three dipoles will fit in place of a circular arc of a given length and angle. Not all dipoles in the ring will be split, only those which are standard arc dipoles. The dipoles that aren't split will have fields corresponding to the arc length and bending angle given in Table 0-5. Physical constraints will dictate a minimum drift length between dipoles; the number used here is based on the PEP-II HER dipoles [3]. The maximum dipole field is chosen to keep the dipoles sufficiently far from saturation that the field quality should be nearly identical for the field settings for any energy.

Since the goal of splitting the dipoles is to create transverse damping from radiation to counteract blowup from the beam-beam interaction, we set a target for that transverse damping decrement, defined to be the fractional reduction in transverse emittance per turn from synchrotron radiation, far from equilibrium. For the purposes of this design, we take this damping decrement to be the energy loss per turn divided by $2\beta^2 E$, where β is the relativistic β and E is the total beam energy. The transverse damping decrement may depart from this value, in particular due to Robinson wigglers. The value we choose in Table 0-5 is approximately that of KEKB [2].

Taking the design requirements from Table 0-5, we split each arc dipole to minimize the maximum magnet width. Three rectangular dipoles are used. For our parameters, making the center dipole bend outward at the lowest energy and be as short as possible while staying below the maximum dipole field at that lowest energy gives the design with the smallest dipole width. The resulting parameters are given in Table 0-6.

The dipoles and their orbits are shown in Figure 0-14. The fields required as a function of energy are shown in Figure 0-15. Synchrotron radiation loss is shown in Figure 0-16; below about 11 GeV the split dipoles increase bending to make the radiation loss proportional to beam energy; at higher energies the orbits are the same and the increase in radiation loss arises from the increase in energy. The additional drifts between the dipoles increase the radiation produced compared to the solution where the three dipoles are replaced by a single dipole. Only the arc dipoles are included in this calculation. The Sokolov-Ternov (de-)polarization time [8] is shown in Figure 0-17. As with the radiation, only the arc dipoles are included, and, similarly to the radiation, the (de-)polarization time at high energy is reduced from the single dipole solution due to the additional drifts.

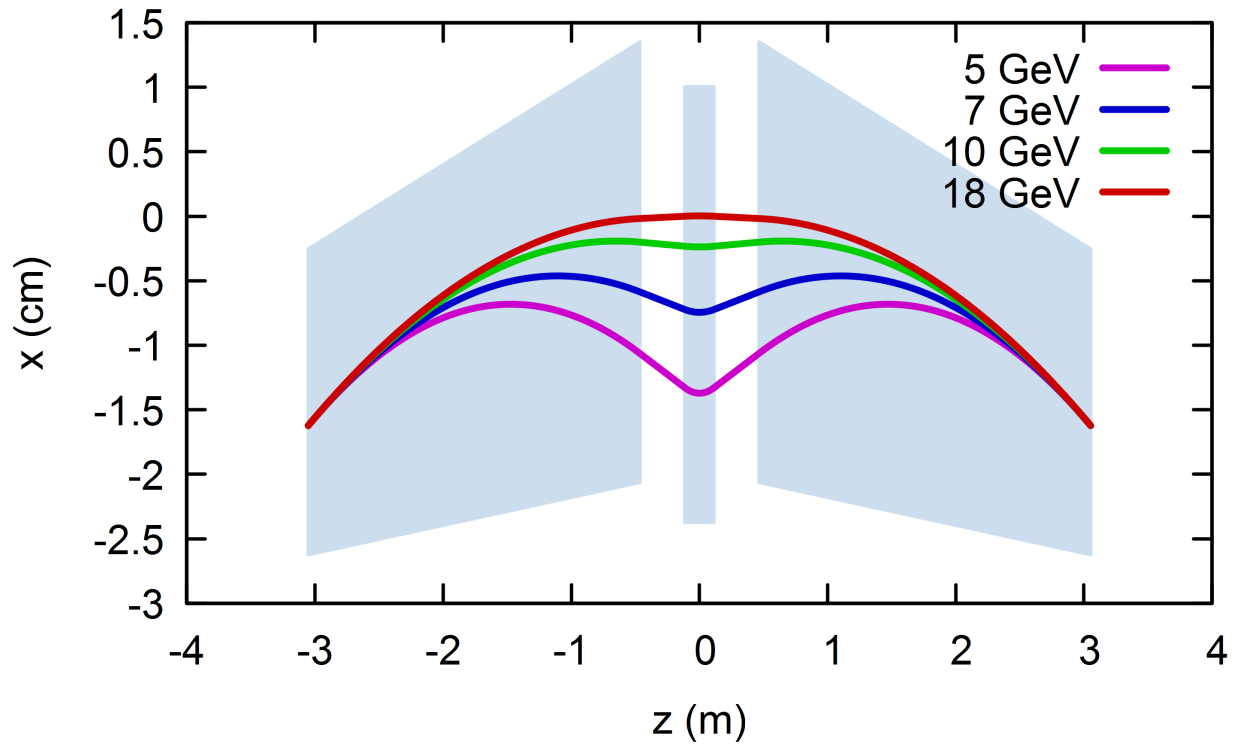


Figure 0-14 Split arc dipoles and orbits for several energies.

Table 0-5: Design requirements for the split dipoles.

| | |
|-------------------------------------|----------------------|
| Circular Arc Length for Dipoles [m] | 6.1067 |
| Bend Angle [rad] | $2\pi / 264$ |
| Number of Split Dipoles in Ring | 216 |
| Drift Between Dipoles [m] | 0.35 |
| Maximum Dipole Field [Tesla] | 1.1 |
| Transverse Damping Decrement | 2.5×10^{-4} |
| Minimum Electron Total Energy [GeV] | 5 |

Table 0-6: Parameters for the split dipoles. Orbit width is the required width of a rectangular magnet to cover the closed orbits at all energies.

| | Length [m] | Bend Angle [mrad] | Field [Tesla] | | Orbit Width [mm] |
|-------|------------|-------------------|---------------|-----------|------------------|
| | | | at 5 GeV | at 18 GeV | |
| Outer | 2.588 | 11.394 | 1.100 | 0.264 | 14 |
| Inner | 0.230 | 1.011 | 0.125 | 0.264 | 14 |

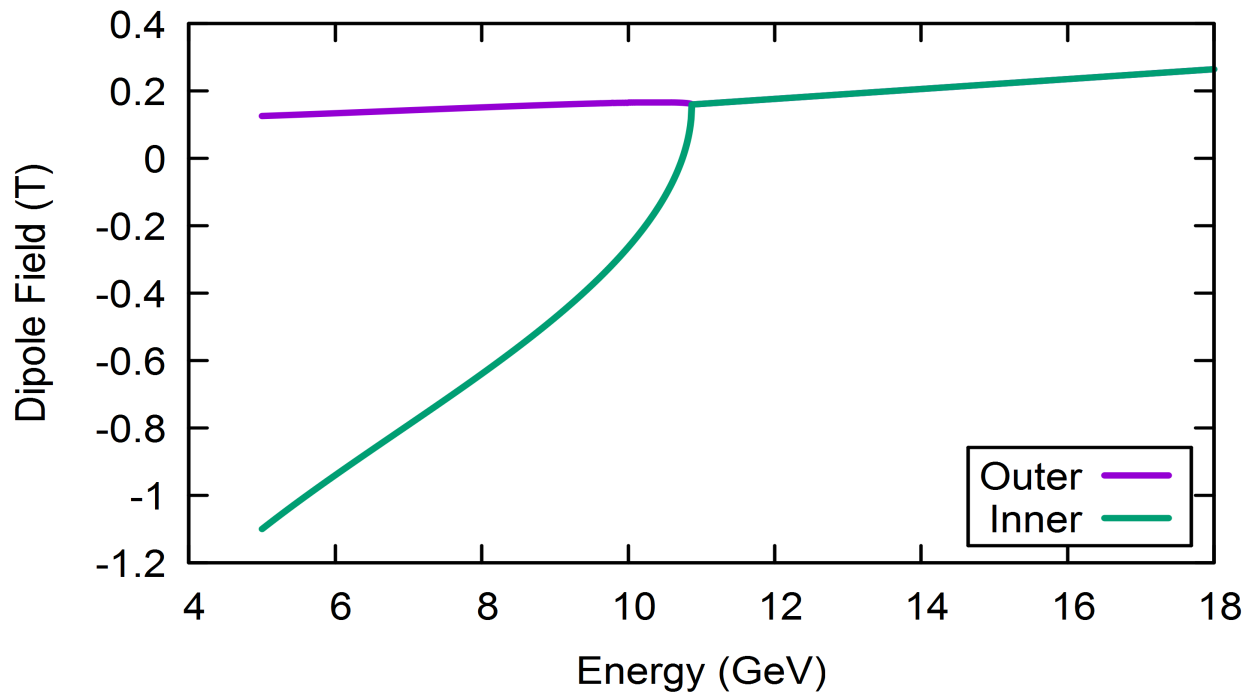


Figure 0-15 Dipole fields as a function of energy.

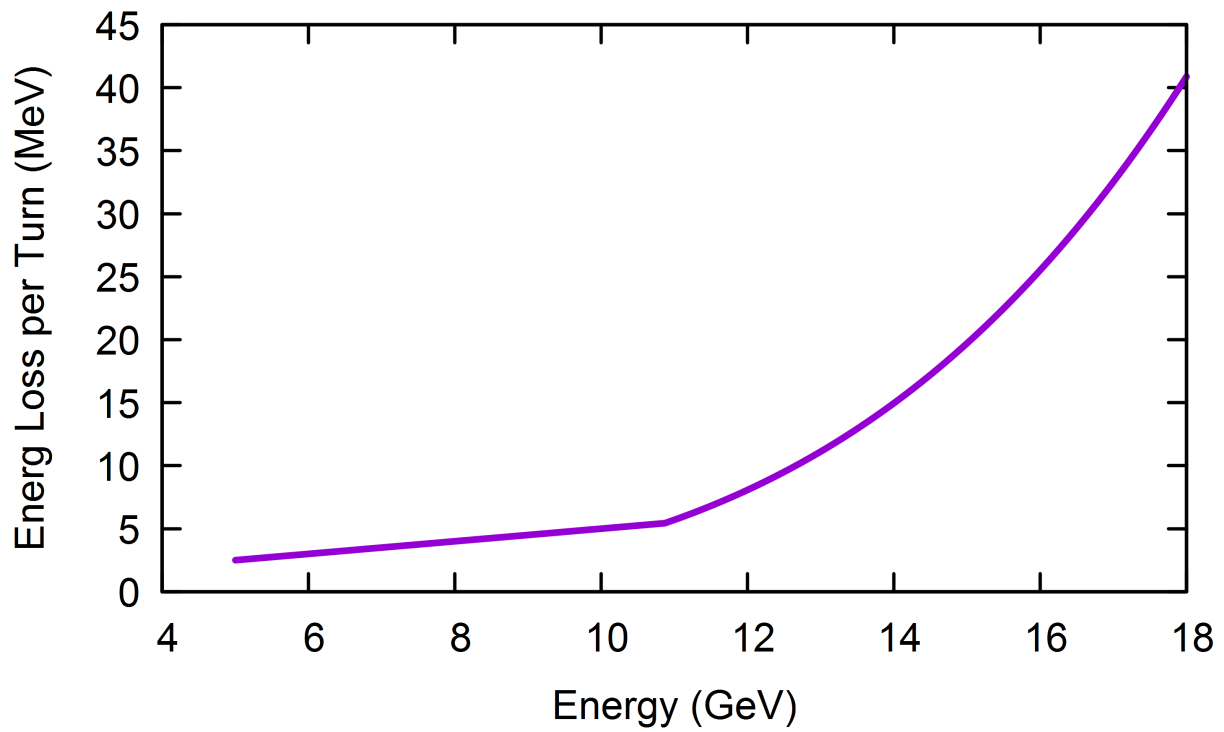


Figure 0-16 Energy loss per particle per turn as a function of energy.

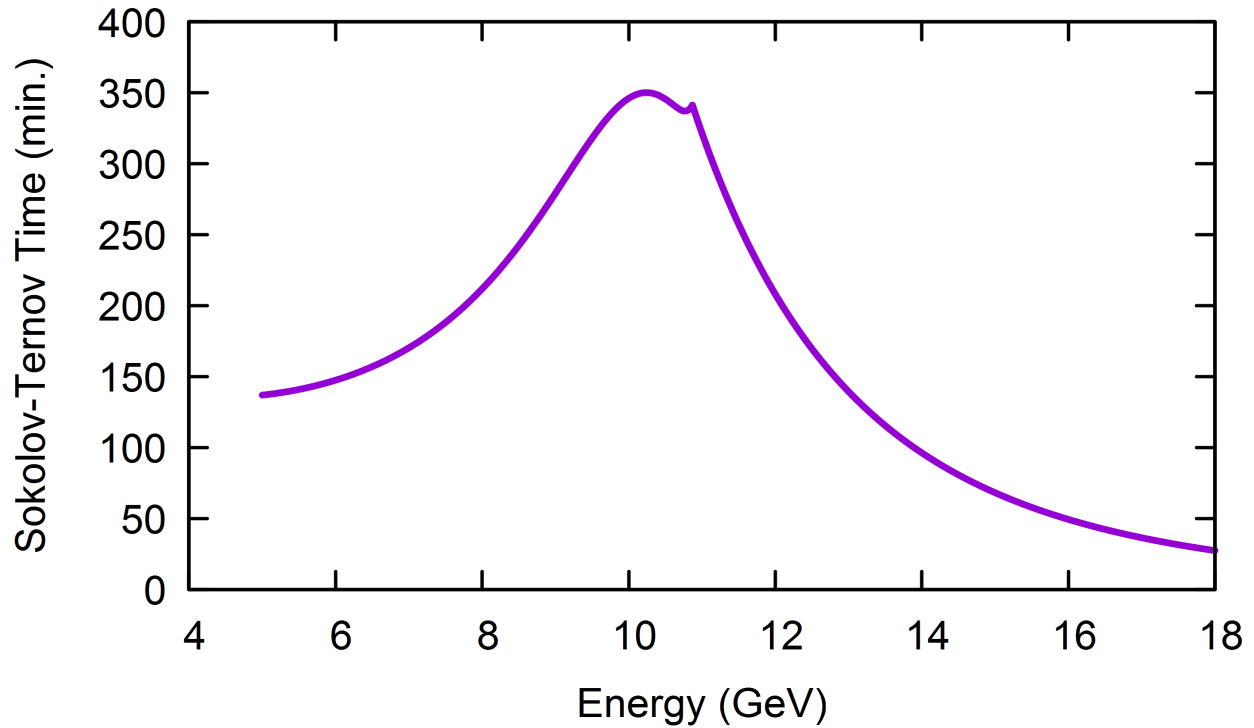


Figure 0-17 Sokolov-Ternov (de-)polarization time as a function of energy.

II.3.4 Proton Interaction Straight Matching

The eRHIC interaction region needs to be integrated into the existing RHIC facility. This task is currently being carried out. No major difficulties are expected.

II.4 Beam-beam Effects and Luminosity

For the analysis of the impact of the beam-beam interaction on the luminosity of the colliding electron and proton beam we refer to Section II.2, where various mechanisms that can lead to a reduction of the luminosity, such as the Hourglass effect and a non-zero crossing angle, are discussed, and the explicit dependence of the luminosity on the beam-beam parameters is given by Equation (5). Here we discuss numerical simulations to assess the impact of the beam-beam interaction on the luminosity and beam stability.

A simple and computationally inexpensive approach to characterizing the impact of the beam-beam interaction on the beam stability is to model the interaction assuming one of the colliding beams “frozen”, or not affected by the other beam. Within this approximation, the beam-beam interaction is studied with weak-strong beam-beam (WSBB) simulations, where the strong beam, not affected by the weak beam, acts as a source of the electromagnetic interaction perturbing the weak beam. Weak-strong beam-beam (WSBB) simulations can be very fast, at the price of neglecting any self-consistent effect or mutual interaction between the colliding beams.

In our case, numerical studies of the beam-beam interaction have been done with strong-strong beam-beam (SSBB) simulations. SSBB Strong-strong beam-beam simulations allow the self-consistent evolution of the colliding beams, thus the study of instability mechanisms acting simultaneously on both beams. The price to pay for strong-strong simulations is a heavy computational load, both in terms of computational speed and memory requirements. While weak-strong simulations can efficiently run on a single processor, strong-strong simulations require multi-processor programming and parallelization.

The strategy we adopt in our studies is to perform SSBB simulations first. If we identify regimes in which one of the colliding beams reaches equilibrium, we perform WSBB simulations for efficient parametric scans.

Strong-strong beam-beam (SSBB) simulations with the parameters listed in Table 0-7 have been done with K. Ohmi's strong-strong beam-beam (SSBB) multi-particle tracking code [9]. The code allows the study of the beam-beam interaction of colliding beams with arbitrary crabbing and crossing angles, via slicing longitudinally the beams and then reducing the beam-beam interaction to "slice collisions", where the electromagnetic fields are obtained by solving the two-dimensional Poisson equation. For a recent application of the SSBB code see [10] where numerical simulations have been compared with experiments to study the performance of crab-cavities at KEKB [2], and see [11] where the luminosity degradation due to incoherent emittance growth and coherent beam-beam instability has been investigated in the Large Hadron Collider.

SSBB simulation results are shown in Figure 0-18, Figure 0-19 and Figure 0-20. No luminosity degradation or coherent beam-beam instabilities have been observed with simulations up to 50000 turns. Long term numerical simulations will be performed to study the asymptotic stability of the proton beam, together with simulations to assess the impact of the beam-beam interaction on the dynamic aperture via tune space stability studies.

Table 0-7 Electron-proton parameters for SSBB simulations.

| Parameter | Symbol [Unit] | electrons | protons |
|--------------------------|------------------------------------|----------------|-------------|
| Circumference | C [m] | 3833.845 | 3833.845 |
| Energy | E [GeV] | 10.2 | 250 |
| Bunch population | $N_{e,p}$ [10^{11}] | 3.1 | 1.2 |
| Number of bunches | N_b | 360 | 360 |
| Emittance | $\varepsilon_x/\varepsilon_y$ [nm] | 24/4 | 18/7 |
| β at IP | β_x/β_y [m] | 2.0/0.07 | 2.8/0.04 |
| Bunch length | σ_z [cm] | 0.8 | 8 |
| Beam-beam parameter | ξ_x/ξ_y | 0.1/0.048 | 0.015/0.003 |
| Disruption | ϕ_y | 0.82 | 0.085 |
| Crab cavity RF frequency | f_{crab} [MHz] | 336 | 336 |
| Crossing angle | ϑ [mrad] | 22 | |
| Betatron tune | ν_x/ν_y | 34.08/31.09 | 31.32/32.31 |
| Synchrotron tune | ν_s | 0.025 | 0.002 |
| Radiation damping | τ_s, τ_x, τ_y [ms] | 1.37/0.68/0.68 | |
| Energy spread | σ_δ | 0.001 | 0.00052 |

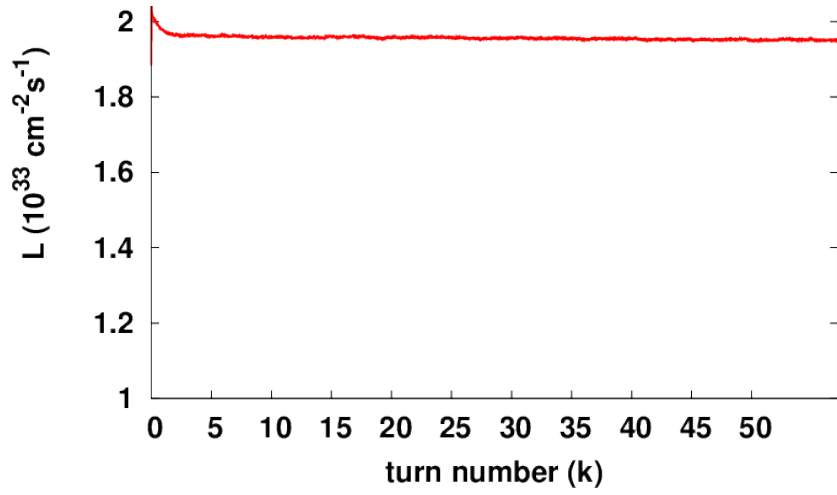


Figure 0-18 Numerical simulation of the SSBB interaction with parameters listed in Table 0-7, showing no significant luminosity degradation up to 50000 turns. The simulation has been done with K. Ohmi's SSBB multi-particle tracking code, and used the following simulation parameters (subscript p stays for protons, e for electrons): $N_p = 10^6$ and $N_e = 2 \times 10^5$ (number of simulation particles), $nslice_p = 15$ and $nslice_e = 2$ (number of longitudinal slices), $N_g = 128 \times 256$ (number of transverse mesh points). The simulation took ~ 5 h on NERSC's supercomputer system Cori using 8 OpenMP threads.

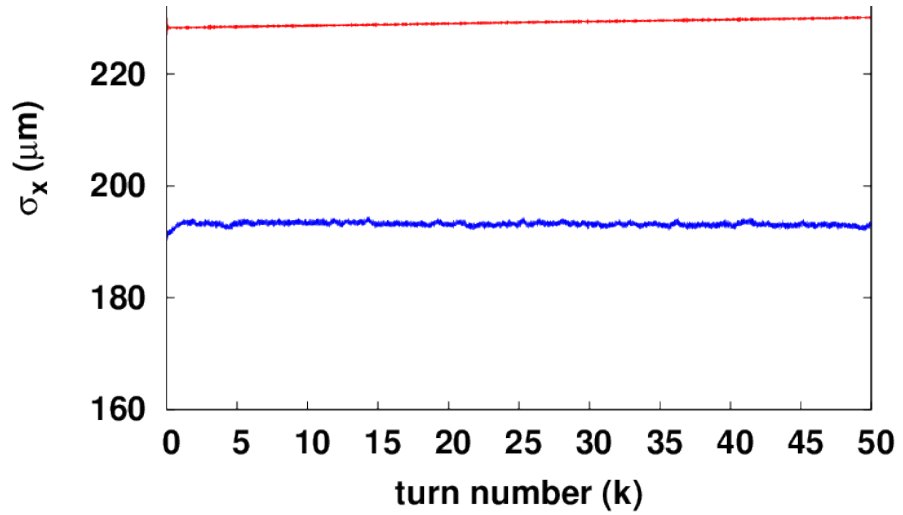


Figure 0-19 Same simulation discussed in Figure 0-18 showing no significant increase in the horizontal bunch sizes.

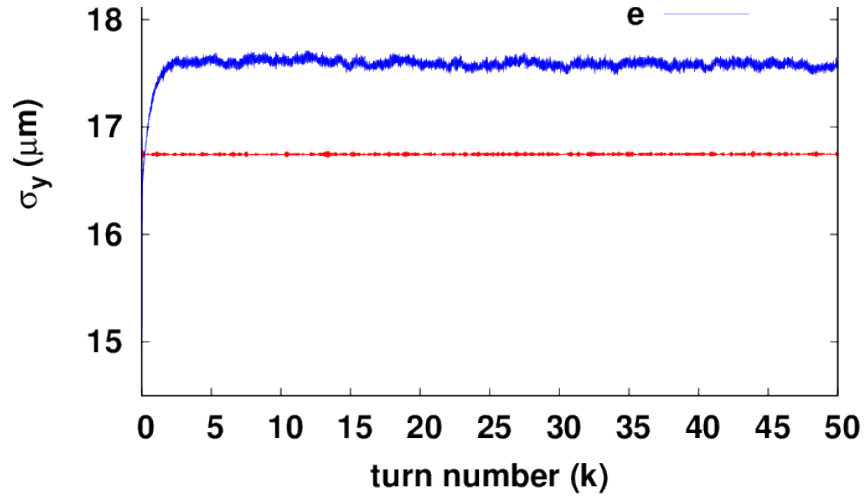


Figure 0-20 Same simulation discussed in Figure 0-18 showing no significant increase in the vertical bunch sizes.

The beam-beam effect of the electron-ion collision is also being evaluated using the self-consistent simulation code BeamBeam3D [12] and faster alternative EPIC [13] using the 2-pass strong-strong approximation. No coherent instability due to beam-beam interaction, such as ‘kink instability’ [14][15], was found with the proposed beam-beam parameters. This is consistent with the results using Ohmi’s SSBB code [9]. Also the codes can be used to study the effect of noise in the crab-crossing scheme and the choice of the working point in the presence of beam-beam effect.

II.5 Dynamic Aperture

The dynamic aperture is defined as the maximum betatron amplitude within which particles are not lost in a given number of turns of single particle tracking. The long-term dynamic aperture converges to the boundary between the regular and chaotic motion. During the RHIC polarized proton operation, 10^6 turn dynamic aperture plays a significant role to evaluate the stability of lattices and to determine the effect of the beam-beam interaction.

The dynamic aperture of the electron ring depends on careful choice and adjustment of sextupole magnets for chromaticity corrections. The chromatic optical distortions caused by the strong focusing in the IR, if left uncompensated, may have a detrimental impact on the dynamic aperture. However, these issues are well known and have been resolved satisfactorily in the past. While the work for the eRHIC electron ring has not yet been completed, there is little risk that satisfactory dynamic aperture can not be achieved.

SimTrack [16] has been intensively used for dynamic aperture calculations for RHIC since 2009. For eRHIC dynamic aperture studies, we plan to use SimTrack as well. SimTrack is a compact C++

code of 6D symplectic element-by-element particle tracking. It provides a 6D symplectic orbit tracking with a 4th order symplectic integration for magnet elements and the 6-d symplectic synchro-beam map for beam-beam interaction. SimTrack is equipped with weak-strong beam-beam simulation for collision with a cross-angle. SimTrack had been benchmarked with MADX, Tracy-II, SixTrack, BBSIM, LifeTrack, etc.

Based on the RHIC experience, the proton dynamic aperture is mainly determined by the nonlinear multipole field errors in the superconducting magnets in the interaction regions and the nonlinear chromaticity. There are 24 independent sextupole power supplies in RHIC. To efficiently correct the second order chromaticities, sextupoles are sorted into a few families. Modern numerical optimization methods are to be used to search the optimum sextupole strengths.

II.6 Collective Effects and Feedback Systems

As of now we have considered instabilities, electron cloud and intrabeam and Touschek scattering. Intrabeam scattering times in the electron ring at radiative equilibrium are more than a second, significantly larger than radiation damping times. Touschek lifetimes are several hours. Instabilities in the electron ring have been studied using a modified version of TRANFT [17], which was used during the design of NSLS-II and evolved into the stochastic cooling simulation code. Simulations were done for electron energies of 5 GeV, 10 GeV and 18 GeV. We assumed nominal partition numbers and other parameters were taken from Table 0-8.

Table 0-8 Electron beam parameters for $|Z/n|=0.2 \Omega$.

| Parameter | 5 GeV | 10 GeV | 18 GeV |
|--|-------|--------|--------|
| Low current | | | |
| RF voltage [MV] | 20 | 40 | 64 |
| γ_T | 27 | 31 | 45 |
| V_{synch} [MV] | 2.2 | 4.3 | 31 |
| Q_s | 0.075 | 0.065 | 0.037 |
| Q_b [nC] | 48 | 48 | 8 |
| $\epsilon_{RMS, norm}$ [μm] | 228 | 129 | 118 |
| σ_s [mm] | 9.5 | 5.8 | 6.6 |
| $\sigma(p)/p$ [10^{-4}] | 9 | 6 | 9 |
| I_{peak} [A] | 606 | 1000 | 145 |
| Full current | | | |
| Effective voltage [MV] | 12 | 23 | 50 |
| σ_s [mm] | 14 | 11 | 7 |
| $\sigma(p)/p$ [10^{-4}] | 9.5 | 8.4 | 9 |

Only single bunch instabilities were considered so far. Given the preliminary stage of design the longitudinal and transverse impedances were modeled as resonators with quality factor 1 and resonant frequency 10 GHz. The longitudinal impedance was adjusted to make $Im(Z/n) = 0.2 \Omega$ at low frequency and the transverse impedance at low frequency was $Z_x = Z_y = 270 \text{ k}\Omega/\text{m}$.

Figure 0-21 shows the wake potentials for the RF cavities for a 2 mm long driving bunch. The wake labeled central RF (red) is for 32 cavities shown with a blue profile in the cavity (Figure 0-22). The black curve in Figure 0-21 denoted end RF is the wake from 2 cavities with the profile shown in red in the Figure 0-22. Note that the difference is due to whether or not the cavity necks down at the ends. The blue curve is the wake for one tenth the assumed value. The cavity contribution to the short range wake is clearly negligible.

The simulations were done with zero synchronous phase with a voltage giving the correct small amplitude synchrotron frequency. Results are summarized in the table. The beam profiles and the parasitic voltages for electron energies of 5 GeV, 10 GeV and 18 GeV are shown in Figure 0-23, Figure 0-24 and Figure 0-25, respectively. Everything is stable.

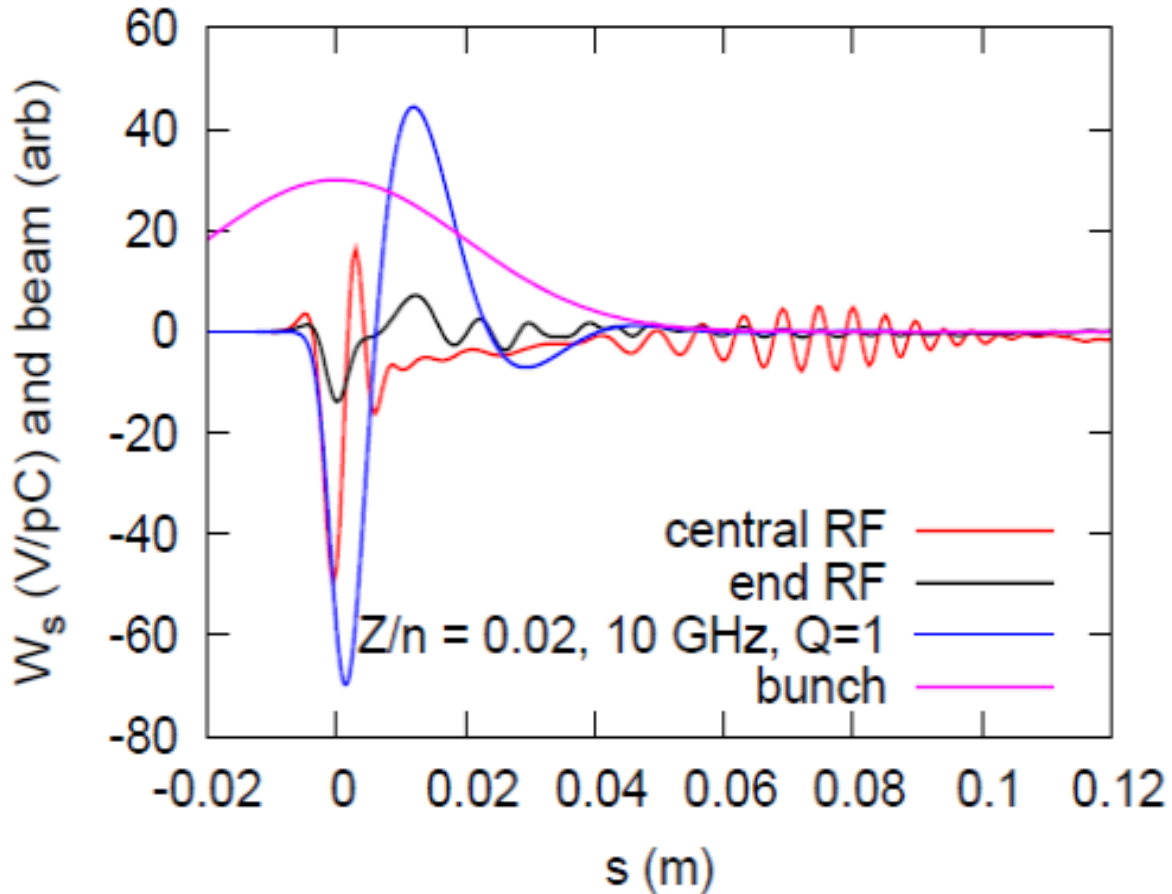


Figure 0-21 The wake potentials for 34 RF cavities for a 2mm driving bunch. The curves labeled ‘end RF’ are the contribution from 2 cavities with the change in radius shown in Figure 0-22, while the contribution from 32 others called ‘central RF’ have the blue profile shown in Figure 0-22. The blue curve corresponds to a wake potential with broadband impedance of 0.02 Ohms, one tenth the value assumed in the simulations. Hence the RF cavities have a negligible impact on the short range wake.

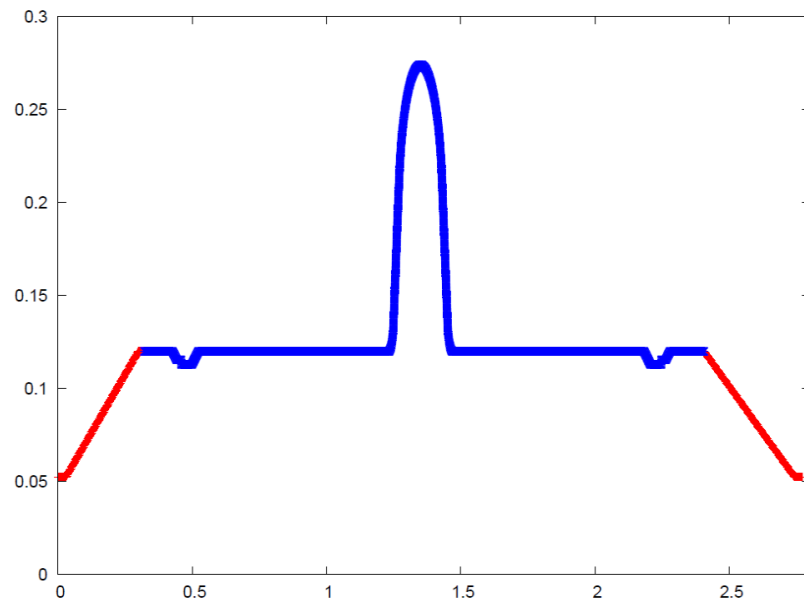


Figure 0-22 RF cavity profile. The change in radius shown in red only occurs at the end of cavity strings while the blue profile is relevant within strings.

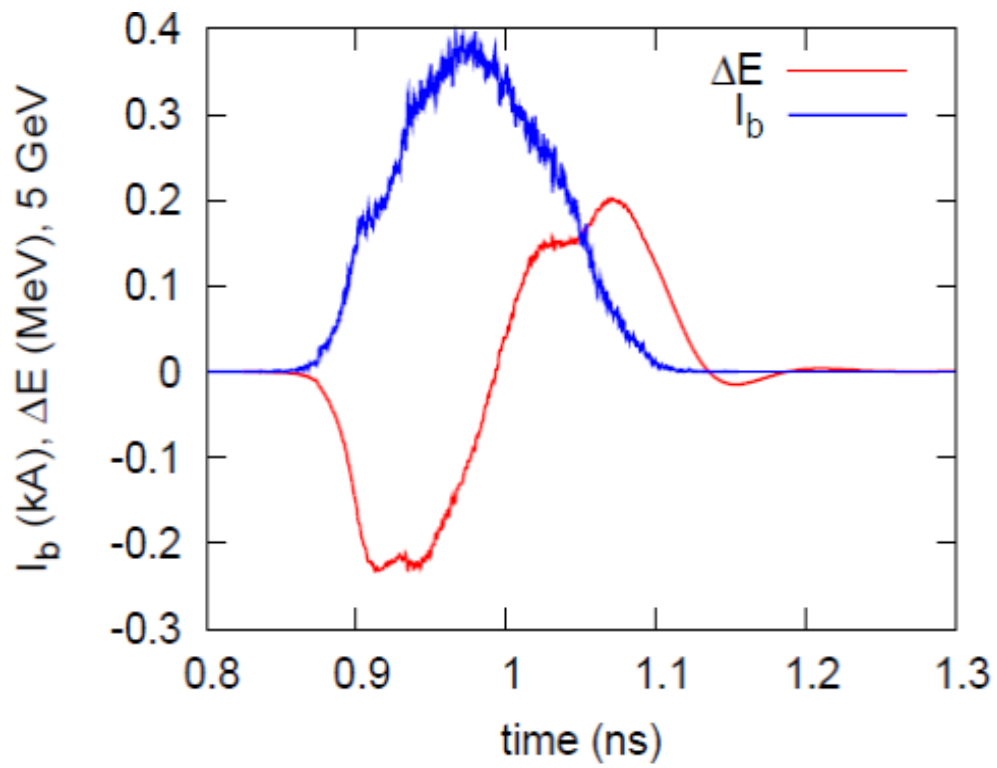


Figure 0-23 The beam profiles and the parasitic voltages for an electron energy of 5 GeV.

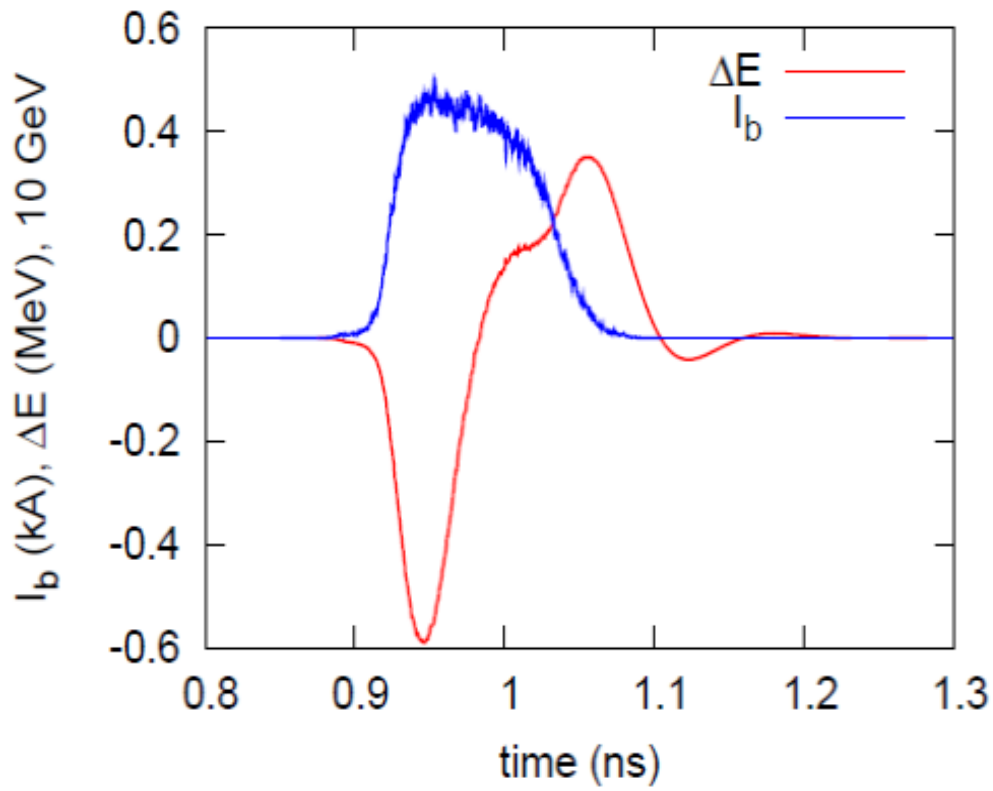


Figure 0-24 The beam profiles and the parasitic voltages for an electron energy of 10 GeV.

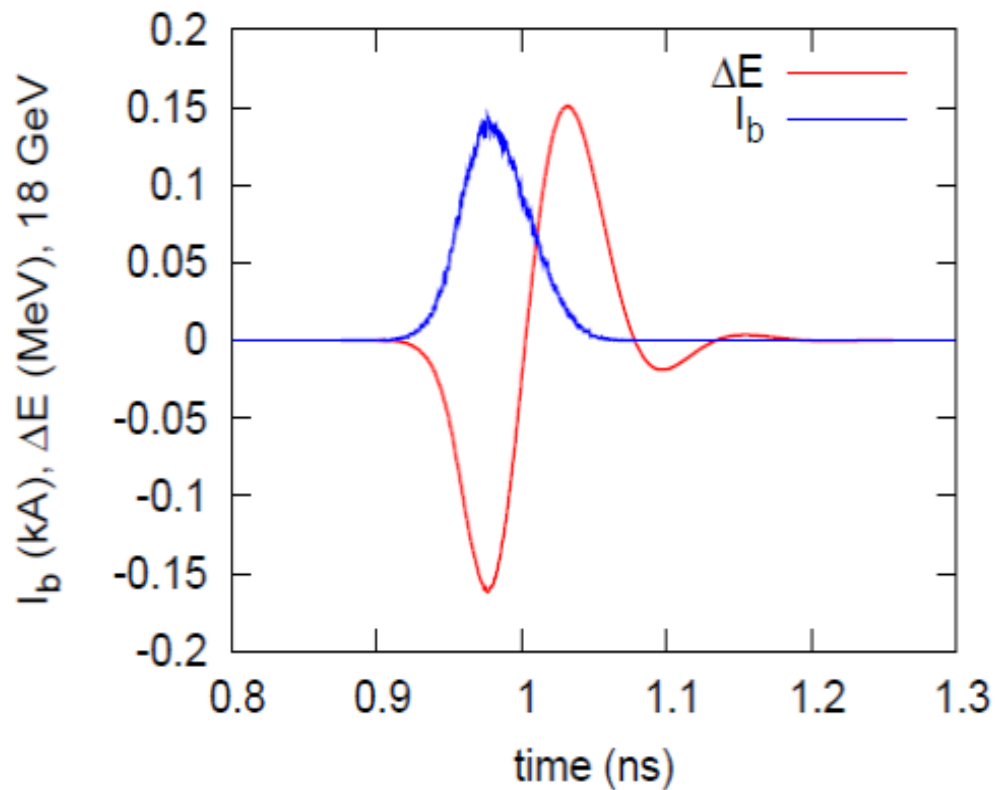


Figure 0-25 The beam profiles and the parasitic voltages for an electron energy of 18 GeV.

Electron clouds are a serious concern for the ion ring with 360 bunches. We assume a copper coated pipe and that we will be able to scrub to the level achieved in the LHC. An initial simulation using CSEC [18] and a best guess model for the wall parameters in the scrubbed LHC showed dangerous electron clouds both for the LHC and for eRHIC, with LHC being slightly worse. For both machines the average dose to the wall was in the tens of watts per meter range but this value depends critically on the assumed secondary emission yield, which was inferred for the LHC using the measured energy deposition. Hence the secondary yield used in our simulation must differ from that used for the LHC. This will be resolved.

Our plan for finishing our study of collective effects is as follows. We will redo our IBS and Touschek calculations using independent codes and verify they are not a concern. Next we will address coupled bunch instabilities and electron clouds.

For instabilities we will continue using TRANFT [17] since it is fast and accurate. We will consider a range of impedance models, expressing our uncertainty, and produce threshold currents for each. For coupled bunch instabilities we will use the higher order mode data for the KEKB cavities and the resistive wall contribution. Other large devices, such as the injection kicker, will also be considered. An active damper will almost certainly be necessary and we will model noise in the system so that any residual oscillations of the electron beam will be accurately reproduced. The system must result in fluctuations that are not harmful to the ion beam.

For electron clouds we will collaborate with CERN, understand, and reproduce their results. In the end we know that electron clouds in the LHC are difficult but tractable. There is currently no reason to believe otherwise for eRHIC.

II.7 Effect of Intrabeam Scattering

Intrabeam scattering (IBS) causes emittance growth that, by reducing luminosity, limits the useful run time and, given a turnaround time of the order 1 hour, efficiency. It is therefore desirable to achieve an IBS growth time of several hours, thus allowing long physics stores.

Table 0-9 lists beam parameters and calculated IBS growth times for nominal design parameters of protons at 50, 100, 160, 200 and 250 GeV.

Table 0-9 Nominal parameters for eRHIC protons beam.

| Energy [GeV] | 50 | 100 | 150 | 200 | 250 |
|---|------|-----|-----|-----|-----|
| Bunch intensity [10^{11}] | 1.5 | 1.5 | 1.5 | 1.3 | 1.5 |
| Horizontal RMS normalized emittance [10^{-6} m] | 4.7 | 4.7 | 4.7 | 4.7 | 4.7 |
| Vertical RMS normalized emittance [10^{-6} m] | 1.8 | 1.8 | 1.8 | 1.8 | 1.8 |
| Longitudinal bunch area [eVs] | 0.6 | 0.7 | 0.8 | 0.8 | 0.8 |
| RF frequency [MHz] | 394 | 394 | 394 | 394 | 394 |
| RF voltage [MV] | 4 | 5.1 | 8.2 | 9 | 14 |
| RMS momentum spread [10^{-4}] | 14 | 9.5 | 8.1 | 6.6 | 6.5 |
| RMS bunch length [cm] | 13 | 12 | 10 | 9 | 8 |
| IBS growth time for longitudinal emittance [hours] | 10.5 | 7.3 | 7 | 6.4 | 6.9 |
| IBS growth time for horizontal emittance [hours] (no coupling) | 9.9 | 7.9 | 7 | 7.3 | 6.9 |

For the nominal parameters as listed in the Table, beam growth due to Intrabeam Scattering (IBS) is not significant so that cooling of protons with such parameters is not required. These parameters assume a new 394 MHz RHIC RF system. An additional assumption is that horizontal and vertical motion in RHIC are fully decoupled, which allows to have unequal emittances in the horizontal and vertical planes. With such fully decoupled motion, longitudinal IBS results only in growth of the horizontal emittance through the lattice dispersion. The vertical growth in such a case is negligible and is omitted from the Table. To achieve the longitudinal bunch area shown in the Table some manipulation in the injectors maybe needed.

II.8 Collimation System

eRHIC needs a highly efficient two-stage proton collimation system as well as synchrotron radiation masks in order to maintain low background conditions for the experiments and to serve as machine protection. In addition to transverse collimation, a momentum collimation system will be added. Momentum collimation can assist with losses caused by the modulation of the beam-beam force experienced by protons with large synchrotron amplitudes in the head or the tail of the bunch due to the crossing angle. Currently RHIC does not have momentum collimators.

The current RHIC two-stage transverse collimation system, consisting of 45 cm single sided copper jaws, is installed between 41 m and 58 m downstream of IP8 [19]. Both primary and secondary collimators are located downstream of the Q3 magnet of the focusing RHIC triplets and upstream of the RHIC Q4 magnet. Figure 0-26 shows a schematic drawing of the collimator assembly around IP8. There are two horizontal secondary collimators and one vertical secondary collimator. The primary, L-shaped, collimator serves both planes. All secondary collimators and the horizontal primary collimator can be rotated to align them with the beam trajectory.

As a rule of thumb the optimum phase advance $\Delta\Phi$ between primary and secondary collimators should be kept approximately to:

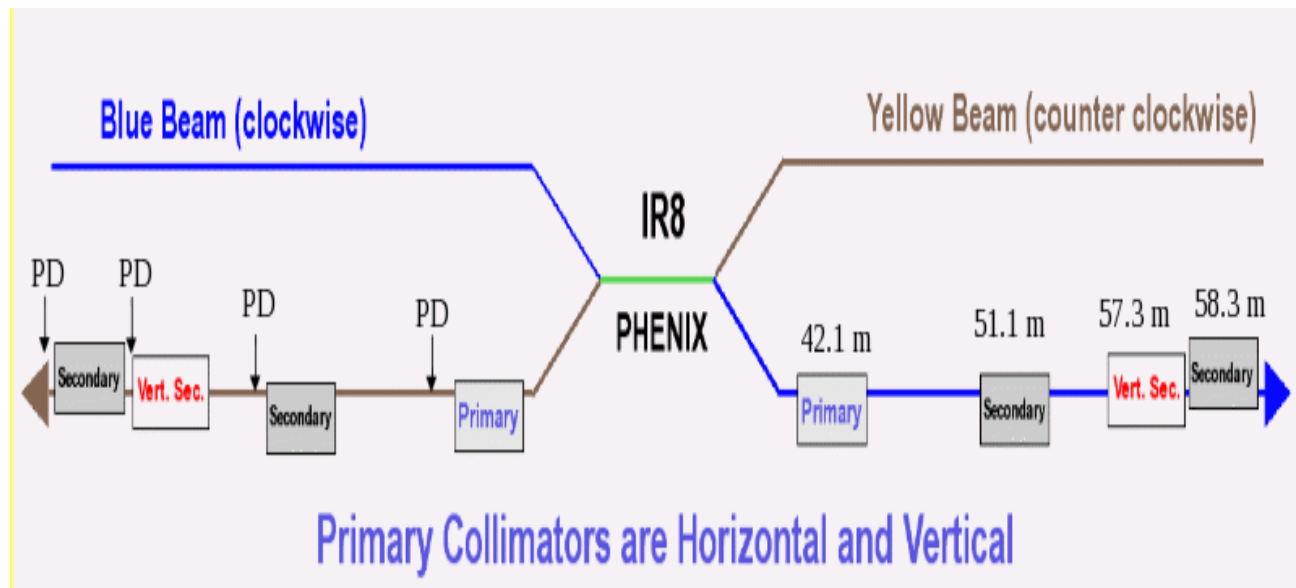


Figure 0-26 Schematic drawing of the current RHIC transverse collimation system.

$$\Delta\Phi \sim n * 180^\circ \pm (20^\circ \text{ to } 30^\circ), n \text{ integer}$$

The \pm sign accounts for secondary collimators to move in from both sides of the beam. For secondary collimators installed one arc or more downstream from the primary collimator such an optimal phase difference could not be kept in RHIC due to the large variety of betatron tunes used for heavy ion and proton operation. Thus the installation of primary and secondary collimators within one straight warm section between the RHIC Q3 and Q4 magnets was chosen. According to [20], 85% to 99% efficiency is estimated for the HERA system. The efficiency of the RHIC two stage collimation system has not been studied systematically. However, an efficiency of no more than 50% for protons is assumed for operation without angular adjustment of the jaws. During routine operation, collimator angles are not changed. A detailed study of the RHIC collimation system efficiency in view of its suitability for eRHIC will be conducted during the 2017 RHIC proton run. In principle, the RHIC collimation system can be upgraded to serve as an eRHIC collimation system. Upgrades could include two vertical secondary collimators, angular adjustment of the primary vertical collimator or a new, HERA-style design [20] with two movable tungsten jaws per vacuum tank. For momentum collimation the eRHIC primary collimators have to be either in a dispersive region or an additional system in such a region has to be added. Due to the multi-turn nature of collimation in general, proton collimators do not have to be close to the experiments and no difficulty in finding such an area is anticipated.

This is different for synchrotron radiation (SR) shielding, or SR masks. SR is generated wherever the e-beam is bent or focused; in particular close to the experimental detectors shielding is required perhaps even inside the experimental detectors (see [21] and [22]) if it is not possible to shield the SR outside. A system of masks and absorbers has to be designed which will leave an aperture large enough for the beam and the SR fan to pass while being small enough to protect the experiment from primary and back-scattered radiation. The fact that the absorbers themselves are sources of back-scattered radiation needs to be taken into account in the design. Extensive simulations (for instance with GEANT) are needed to create a detailed map of the SR profile including direct radiation for the nominal beam orbit and for an offset beam orbit as well as back-scattered radiation. The final design depends strongly on the detector and IR design. In turn, the detector design might be influenced by shielding considerations and an early collaboration of machine and detector experts is not only beneficial but required.

II.9 RF Systems

II.9.1 Electron Ring RF

For 18 GeV electrons the synchronous voltage is 31 MV per turn. The system is designed to handle 10 MW of synchrotron radiation. For these parameters the superconducting cavities used in KEKB [2] and superKEKB [23] are close to ideal. Their frequency is 509 MHz, for our application we will set the RF frequency to 18 times the $h = 360$ frequency in RHIC. The frequency corresponding to high energy protons is 507.04 MHz and 506.94 MHz for 50 GeV protons, a 100 kHz tuning range. The voltage requirements depend on the lattice. Figure 0-27 shows the buckets for 5,10 and 18 GeV electrons.

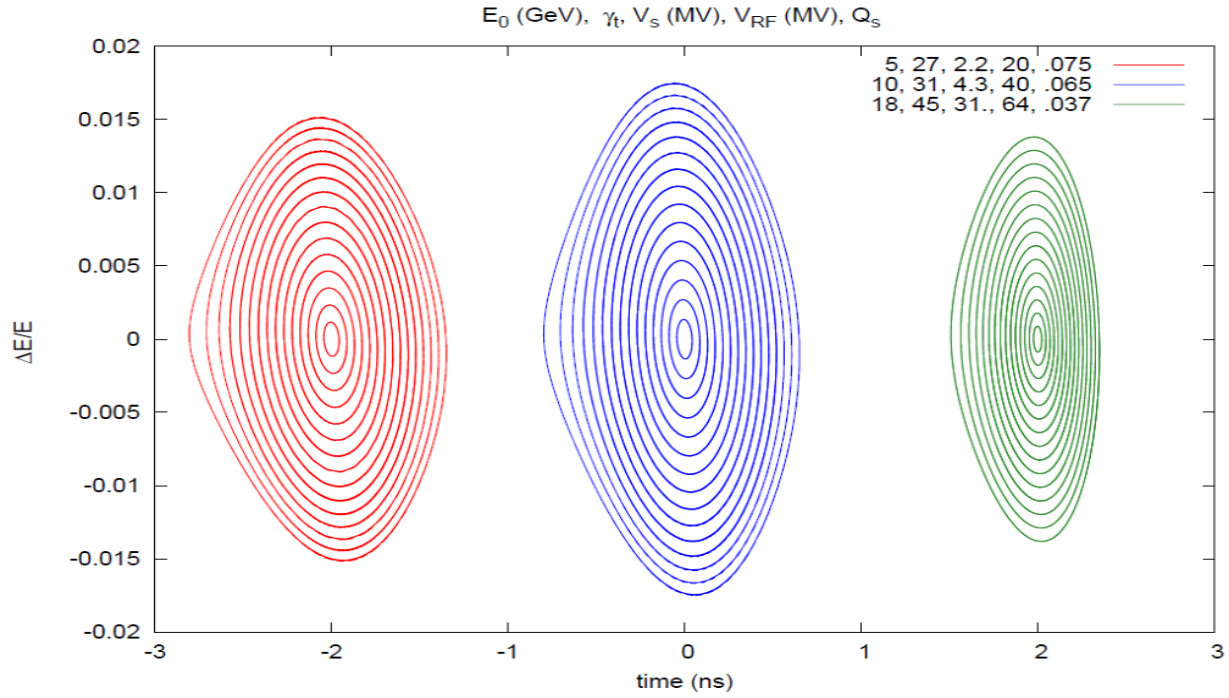


Figure 0-27 Buckets for 5 GeV, 10 GeV and 18 GeV electrons.

For good bucket area at 18 GeV we need 64 MV of installed voltage. The KEKB and superKEKB cavities regularly operate at cavity voltage $V_c = 1.5$ MV and cavity power $P_c = 400$ kW. For 64 MV we need 43 of these cavities. The KEKB cavities operated at up to 2 MV so if running at that level is reliable we would need 32 cavities with 3 or so spares. With 10 MW of synchrotron radiation we need no more than 312 kW per cavity, which is below the 400 kW planned for superKEKB [24]. We will take 35 cavities for what follows.

The effect of beam loading is significant. The cavities have a circuit $R/Q = 50 \Omega$ and a resonant frequency of 507 MHz. The cavity detuning is given by:

$$\delta f = \frac{I_{RF} f_{RF}}{2V_c} \left(\frac{R}{Q} \right) \cos \phi_s \quad (15)$$

where V_c is the cavity voltage, f_{RF} is the RF frequency, $I_{RF} \approx 2eN_b f_{RF}$ is the RF component of the beam current with N_b the number of particles per bunch. Beam loading is worst at 5 GeV. For 3×10^{11} electrons per bunch we get $I_{RF} = 2.8$ A. With $\phi_s = 3.031$ and $V_c = 0.57$ MV we get $\delta f = -62$ kHz.

Along with the ideal frequency one also needs ideal coupling to minimize amplifier power. For superconducting cavities the power required to drive a cavity is

$$P_c = \frac{Z_e}{8} \left(\frac{V_c}{Z_e} + \frac{2P_b}{V_c} \right)^2 \quad (16)$$

where P_b is the power given to the beam by one cavity and Z_e is the external impedance. The power goes entirely to the beam without any reflected power when $Z_e = V_c^2/2P_b$. For 10 GeV the power due to synchrotron radiation is 6 MW for 48 nC bunches and the cavity voltage is 1.15 MV so, ideally $Z_e = 1.8 \text{ M}\Omega$. At 18 GeV the total power in synchrotron radiation is 10 MW and the cavity voltage is 1.8 MV so ideally $Z_e = 5.8 \text{ M}\Omega$. If we optimize the coupling for 18 GeV then the amplifier power per cavity at 10 GeV is only 180 kW. So, it is likely we will be able to use fixed cavity tuning set for 18 GeV. Given the $5.8 \text{ M}\Omega$ impedance the quality factor is 1.2×10^5 , larger than the 5.0×10^4 value for superKEKB and hence easier to achieve. The cavity full width half power bandwidth will be 4.2 kHz. When we run at 5 GeV with a detuning of 64 kHz the h-1 revolution line is only 3.2 cavity bandwidths away. We will need to be very careful about the h-1 coupled bunch instability.

Some R&D is needed for the RF system. While a cavity voltage of 2 MV has been achieved [24] the operating voltage is more like 1.5 MV. Significant work will be required to make the system operational at the higher voltage. The HOM power is challenging. In KEKB the 10nC bunch charge and 250MHz bunching frequency give 37 kW of HOM power per cavity. For eRHIC we have 48 nC and 28 MHz giving 95 kW per cavity. Our bunch length will be of order 10mm, significantly larger than the 5mm length in superKEKB. This will reduce the microwave load on the cavities significantly. Nonetheless this needs to be carefully monitored as does the impedance of the rest of the machine. With regard to beam dynamics, the synchrotron tune reaches 0.075 at 5 GeV. We plan on installing cavities in the 4 and 10 o'clock straight sections to reduce longitudinal chaos but it will be necessary to do a careful analysis of synchro-betatron resonances. At this point single bunch instability is not expected but if we are not careful with our impedance budget a higher harmonic RF system may be necessary. We note that such a system would greatly reduce the synchrotron tune, alleviating synchro-betatron resonances.

II.10 Crab Cavities

The crab cavity needs to compensate the luminosity loss due to a crossing angle of 22 mrad. The required voltage is

$$V = \frac{\theta_c E_b / q}{2k_{cc} \sqrt{\beta^* \beta_{cc}} \sin \Delta\psi} \quad (17)$$

where θ_c is the full crossing angle, E_b is the beam energy, q is the charge of the particle, k_{cc} is the wave number of the crab cavity. β^* and β_{cc} are the β -functions at the interaction point (IP) and crab cavity location respectively, and $\Delta\psi$ is the phase advance between these two locations.

The crab cavity frequency of the ion beam is chosen to be 336 MHz, which is the 12th harmonic of the bunch frequency. The crab cavity frequency of the electron beam is set to 500MHz, the same frequency of the crab cavity in KEK. The required voltage and relevant parameters are listed in Table 0-10.

Along with improving the luminosity crab cavities reduce the synchro-betatron driving terms associated with the bunch position dependent beam-beam force. Figure 0-28 shows the proton offset

as a function of distance from the IP, the RMS electron beam radius, and the proton beam density that experiences that offset.

Table 0-10. Crab cavity parameters.

| Parameter | electron | ion (p) |
|--|------------|------------|
| Crossing angle (Full) [mrad] | 22 | |
| Beam energy [GeV] | 18 | 275 |
| Horizontal β -function at IP, β^* [m] | 2 | 2.8 |
| Transverse beam size at IP [μm] | 212 | 212 |
| Bunch length [cm] | 0.8 | 8 |
| β -function at crab cavity, β_{cc} [m] | ~ 100 | ~ 800 |
| Frequency of fundamental crab cavity [MHz] | 500 | 336 |
| Voltage of fundamental crab cavity [MV] | 1.3 | 9 |

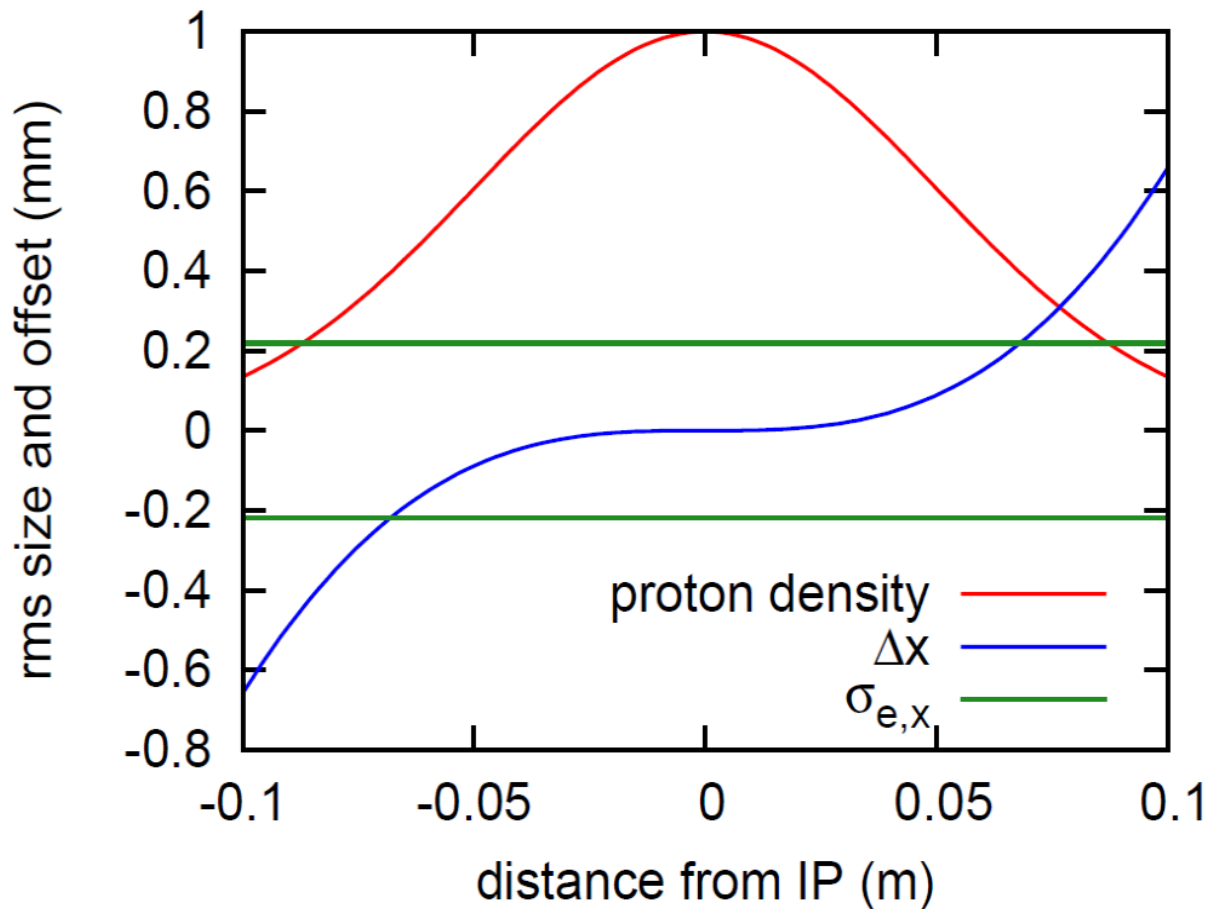


Figure 0-28: RMS effective size, offset and proton-density as function of distance from the Interaction Point (IP). 5% of the protons will see an offset larger than 2σ in the horizontal

direction.

As is clear from Figure 0-28 the proton offsets near the head and tail of the bunch are large. Particles with large synchrotron amplitudes will see significant modulation of the beam-beam force and it is necessary to check whether this will lead to emittance growth or beam loss.

The design of the electron crab cavity can adopt the mature design of the KEK crab cavity with elliptical shape. The cavity for the ion beam is based on the same geometry as the cavity for the LHC high-lumi upgrade [25][26], with necessary scaling and optimizations accordingly. The LHC Accelerator Research Program in the Collider Accelerator Department of Brookhaven National Lab has delivered a successful compact crab cavity design for the Hi-Lumi upgrade of LHC [27], shown in the left of

Figure 0-29 This 400 MHz crab cavity is based on a double quarter wave (DQW) geometry with push-pull tuning system, three higher order mode couplers, and a 50 kW fundamental power coupler. The Proof of Principle DQW crab cavity has reached 4.6 MV of deflecting voltage in a 2 K cold test [28].

For eRHIC, the crab cavity frequency is close to the LHC cavity, which leads to a similar design with simple scaling and less constraints. The radius of the minimum aperture of the crab cavity is set by 10 sigma of the transverse beam size, which is 3.9 cm. Given that the LHC crab cavity has an aperture radius of 4.2 cm, which is already sufficient for eRHIC, the scaled cavity at 336 MHz would have an even larger aperture to satisfy the requirement.

The 336 MHz crab cavity with the DQW design should deliver higher deflecting voltage, depending on the optimization. Multiple crab cavities can be used to provide sufficient voltage for different operation scenarios. The compact size of the DQWCC allows multiple cavities to easily fit in limited space environments. Figure 0-30 shows the dimensions of the LHC 400 MHz DQWCC.

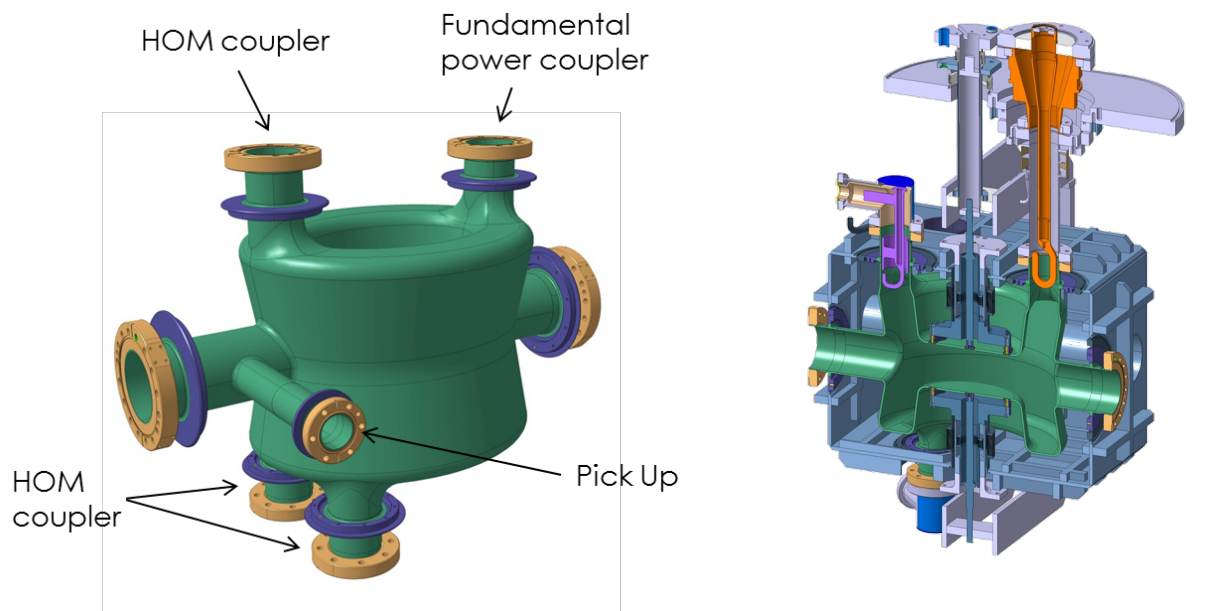


Figure 0-29: Left: DQW crab cavity for Hi-Lumi LHC; right: Cross-section view of the DQW crab

cavity in a helium vessel with HOM coupler (purple), 50kW FPC (orange), and tuner

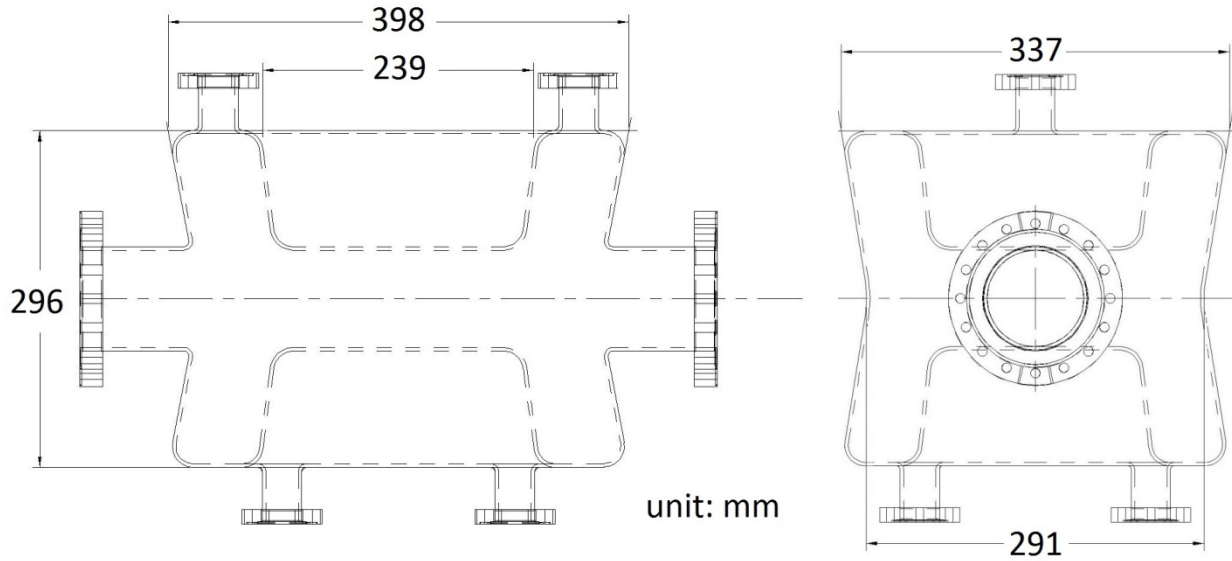


Figure 0-30 Dimensions of the LHC DQWCC at 400 MHz.

II.11 Electron Injection Kickers and Septa

The requirement of arbitrary spin patterns in the electron ring coupled with radiative polarization necessitates regular bunch replacement. We plan to replace electron bunches every 6 minutes. With 360 bunches this corresponds to 1 sec between injections. The kicker will both inject the new bunch and extract the old one. There will be an injection septum on the upstream end and an extraction septum downstream. We envision several stripline kickers, which are independently powered and timed. Take a (very generous) full bunch length of $T_b = 2$ ns, and a bunch spacing of $T_s = 35$ ns. We assume a strip line kicker of length $L = 1.67$ m. The minimum rise and fall times satisfy:

$$T_r = T_f \leq T_s - T_b - 2L/c = 23 \text{ ns} \quad (18)$$

We take a rise time of 10 ns and a fall time of 20 ns, which has been achieved in practice. A flattop voltage of 20 kV is reasonable. If we take a stripline kicker of characteristic impedance 50Ω and a horizontal plate spacing of 6cm then the current in each plate will be 400 A. Assuming a linear rise and fall in current the total energy generated by the pulser is 0.14 joules. When the magnetic field is included a 20 GeV beam is bent by 0.111 mrad. Including things like pumping ports will reduce the effective kick per meter by about 20% so we take an effective kicker strength of $d\theta/dl = k' = 5.3 \times 10^{-5} \text{ m}^{-1}$.

The vertical RMS emittance of the electrons in the storage ring is not more than $\varepsilon = 20$ nm and we assume the injector will satisfy this as well. Take the full length of the kicker section to be L and

optimize the β -functions so that L is the value of the β -function at each end of the kicker. The stored beam size at the end will be

$$\sigma(x) = \sqrt{\varepsilon L} \quad (19)$$

and the RMS angular width of the stored beam will be

$$\sigma(x') = \sqrt{2\varepsilon / L} \quad (20)$$

To separate the beams we want the kick angle to satisfy:

$$\theta_k = M\sigma(x') = M\sqrt{2\varepsilon / L} \quad (21)$$

with M about 10. Now the kick angle is

$$\theta_k = Lk' \quad (22)$$

Setting the two expressions for θ_k equal to each other with $M = 10$ gives $L = 11.2$ m and $\theta_k = 0.594$ mrad. So, we need six kicker modules and the full length of the kicker section will be about $6 \times 1.67 \times 1.2 \approx 12$ m.

Assuming a 12 m drift for the optics in the kicker region the ideal vertical β -function at the center will be 6 m and the β -function at the ends of the kicker will be 12 m. This corresponds to an RMS vertical beam size of 0.44 mm at the ends of the kicker. The vertical offset between the injected and stored beams will be $\Delta y = \frac{L\theta_k}{2} = 3.6$ mm. With a 6 cm full aperture and ± 3 cm clearance for the stored beam this leaves more than ± 2 cm for the injected beam. The stored beam has a 60 σ aperture.

The main R&D considerations are the pulser and in particular whether a half sine wave kicker might be better. The actual electron rms bunch length will be no more than 8 ps if we use a 1.3 GHz linac frequency.

II.12 Electron Beam Injection Complex

II.12.1 Overview

The eRHIC accelerator project requires a full energy injector capable of delivering electron bunches to the storage ring at a rate of approximately 1 Hz. Due to requirements on flexible polarization of the bunches in the storage ring bunch pattern the injector is designed to completely replace every bunch within the 6 minutes period, which is determined by the depolarization time of the circulating electrons. This document describes the “swap-out” injection mode of operations [29] i.e. when the circulating bunch is kicked out of the machine and the incoming bunch with the nominal charge fills the same RF bucket. The “swap-out” mode poses tough requirement on the amount of charge delivered from the injector in one shot (50 nC). To reduce the required amount of charge the accumulation injection mode is also considered with the caveat that the detrimental impact of the accumulating bunch on the proton beam quality due to beam-beam effects needs to be understood. The accumulation mode is not addressed in this document.

General requirements on the eRHIC injector complex are summarized in Table 0-11. The injector parameters are chosen so that the beam entering the ring is matched to the ring RF bucket. The min and max columns list the parameters at the minimum and maximum ranges of performance required for routine eRHIC operations.

Table 0-11 Requirements on eRHIC injector at 18 GeV.

| | min | max |
|--------------------------|-------|-------|
| Energy [GeV] | 5.0 | 18.0 |
| Charge [nC] | 36 | 50 |
| Emittance x/y [nm-rad] | 60/10 | 60/10 |
| RMS Energy spread [%] | 0.2 | 0.2 |
| RMS bunch length [ps] | 3.3 | 3.3 |
| Polarization [%] | 75 | 80 |

The injector block diagram is depicted in Figure 0-31. The photocathode RF gun emits a bunch of polarized electrons, which enters the pre-injector Linac, gets compressed and is accelerated to the energy of 200 MeV. This energy is suitable for preservation of the polarization in the Damping Ring, which accepts the electrons after the Spin Rotator. Once the required charge is achieved by stacking of successive bunches from the pre-injector, the damped bunch is extracted towards the bunch compressor Ch1 that consists of the RF section and a chicane. The RF section imposes an energy chirp, which is then converted into bunching of the electrons so that the bunch length is suitable for acceleration in the 1.3 GHz RF Linac 1. After passing the first Linac section the beam energy increases to 3 GeV. A second stage of compression yields a shorter bunch that circles around the RHIC ring to reenter both Linac sections until the energy of 12 GeV is achieved. Long (total of 3 km) transport lines provide a mild amount of compression to reach the required beam parameters at the injection point of the storage ring.

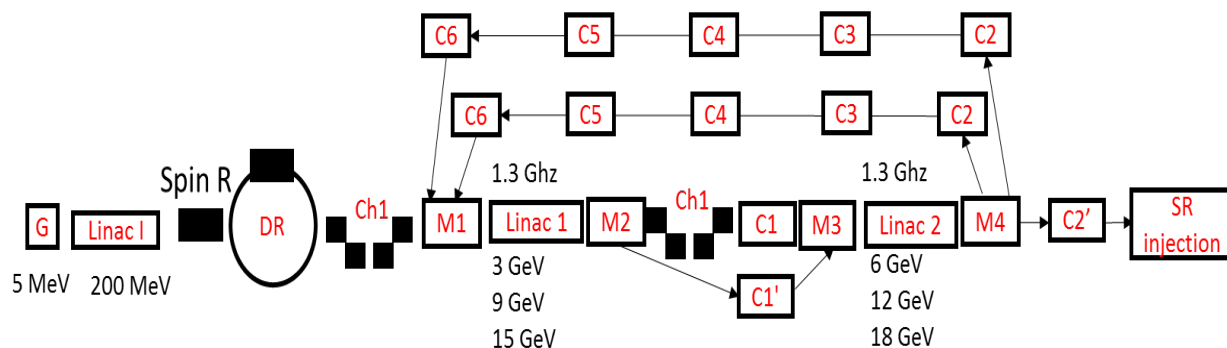


Figure 0-31 eRHIC injector block diagram. G=gun, Linac I = preinjector linac, Spin R = Spin Rotator, DR = Damping Ring, Ch1, 2 = chicanes, M1, 2, 3, 4 = mergers, Linac 1,2 = main linac section, C1, 1', 2, 2', 3...6 = transport line sextants.

Figure 0-32 presents a pictorial view of the eRHIC injector on the actual scale of the RHIC facility. The injector design is based on 1.3 GHz superconducting RF linear accelerators split into 2 sections located in two consecutive straights of the existing RHIC tunnel. Initial assessment shows that the Linac and transport lines will be able to fit into the existing RHIC accelerator enclosure, however much more detailed analysis is due to determine the serviceability of accelerators as well as compliance with the construction codes and potential problems with system installation and testing.

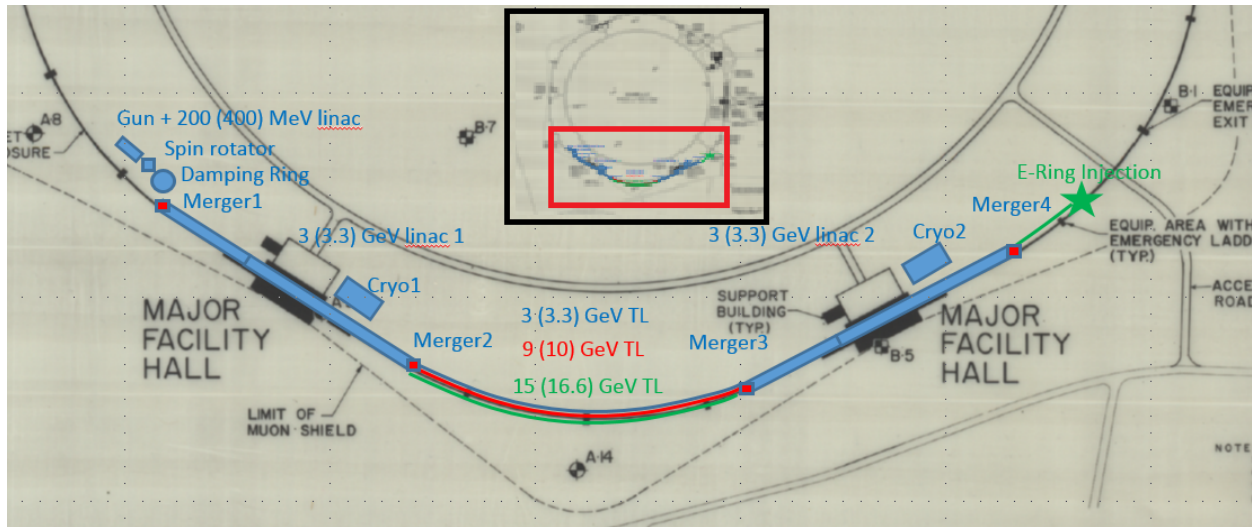


Figure 0-32 Layout of the eRHIC injector facility. The upper box shows a top view of the RHIC facility with the zoom of the future eRHIC injector layout within the red rectangle.

In the following we describe the eRHIC injector subsystems at the level of details available today.

II.12.2 Polarized Gun and Pre-injector

The current design relies on the SLAC SLC type gun [30][31] which had demonstrated reliable performance delivering several nC of polarized electrons (70-75% polarization) at 120 Hz repetition rate. Some gun parameters are listed in Table 0-12 (SLC row).

The next two lines in Table 0-12 describe parameters of two low-energy linear accelerator projects that were developed in the 1990s to accelerate high charge beams for FEL and wakefield-acceleration experiments. Both of them operated at 1.3 GHz RF frequency. The ISIR linac [32][33] and AWA linac [34] were capable to deliver up to 90 nC of unpolarized electrons setting up a decent proof-of-principle of high-charge electron injectors suitable to serve as the basis of the eRHIC low-energy injector design.

Table 0-12 Gun and injector parameters.

| Project | Elements | RF freq [GHz] | σ_s [ps] | Charge [nC] | Energy [MeV] | Emittance [mm-rad] | $\Delta\gamma/\gamma$ [%] | Cathode Material |
|---------|-----------------------------------|------------------|--------------------|----------------|-----------------|-----------------------|------------------------------|---------------------|
| SLC | SLAC gun, 5 mJ laser at 845 nm | DC | 2000 | 12 | 0.12 | 15 | | GaAs |
| ISIR | Gun+Injector | DC+1.3 | 5000 | 90 | <38 | 140 | 2.5 | |

| | | | | | | | |
|-----|------------------|----|------|-------|----|-----------|---|
| AWA | ½ cell Gun+Linac | 13 | 5-30 | 20-90 | 14 | 500--2000 | 2 |
| ANL | | | | | | | |

II.12.3 Damping Ring

A damping Ring (DR) is necessary to increase the charge per bunch from several nC available from the SLC-type gun to the specification for the eRHIC ring of 50 nC. In case the accumulation mode is feasible for the eRHIC RR operations the DR can be bypassed and the gun output be injected to the first 1.3 GHz linac for acceleration.

The low DR energy is defined by the requirement of preserving polarization of electrons while stacking injector pulses prior to the bunch extraction. We are developing a conceptual DR model, which was used as an input for the current design of the eRHIC injector.

Existing examples of the low-energy DR are the SLAC Damping Ring [35] at 1.2 GeV (as seen in Figure 0-33) and APS Positron Accumulation Ring [36] at 0.45 GeV. Both of these are compact (circumference of 30 m) machines and PAR APS demonstrated stacking up to 20 nC of electrons.

These rings may serve as prototypes for the eRHIC injector DR design. We note however that the eRHIC DR design will have to accumulate up to 50 nC of polarized electrons in contrast to both SLC and PAR DRs.

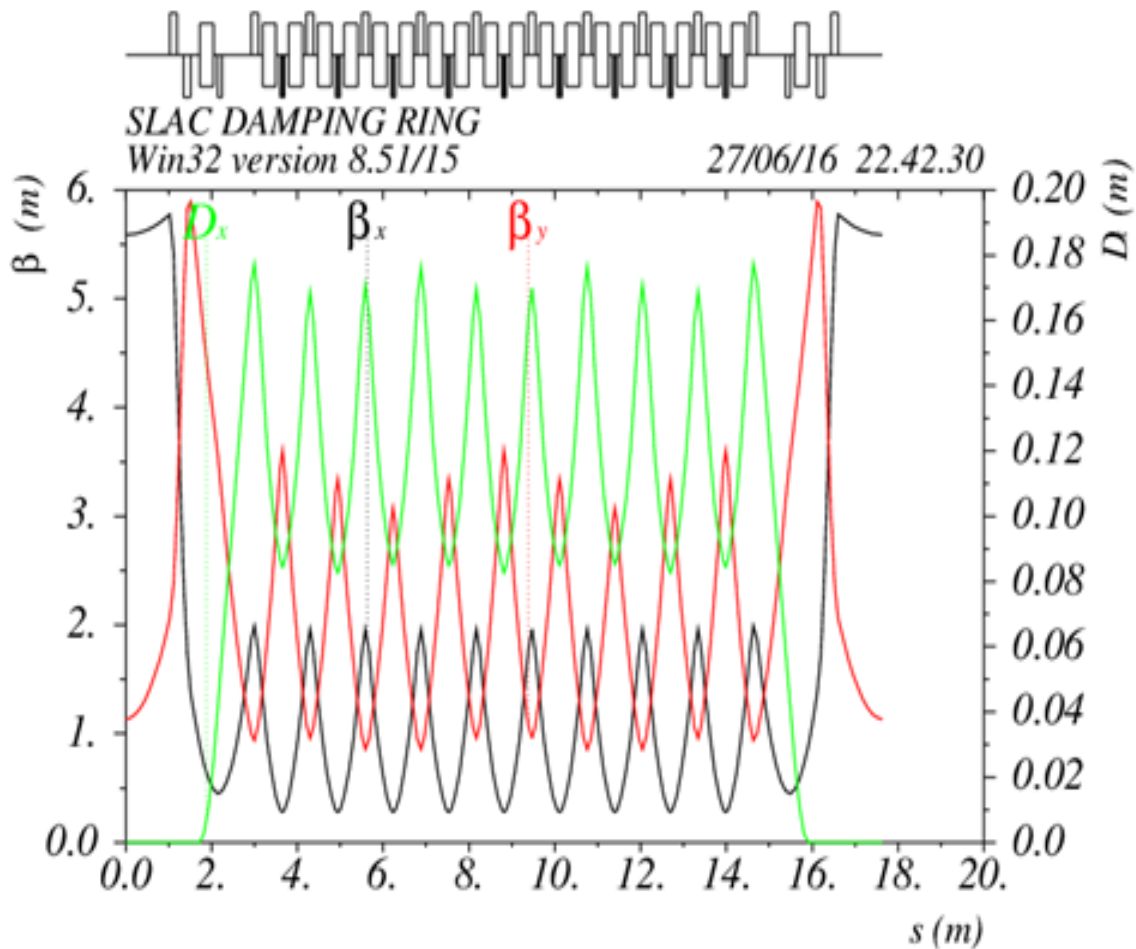


Figure 0-33 SLAC DR lattice functions for ½ ring.

II.12.4 Linac

The current design relies on ILC-type 1.3 GHz superconducting Linac accelerating structures [37] in part due to their availability and reasonably low cost, however an option of using 650 MHz cavities as in the ERL-Ring design [Appendix I], but without energy recovery, is not ruled out. A linac cryo-module consists of 8 modules (Figure 0-34) with 9 RF cells each producing acceleration up to 200 MeV in total at a cavity gradient of 24 MV/m.

A single linac (Linac 1 or 2) will therefore consist of 16 cryomodules providing 3 GeV energy gain per single pass of the electron bunch. These modules will be powered by four MW-class multi-beam klystrons, TH1801 produced by THALES Electron Devices, VKL 8301 by CPI, or E3736 by Toshiba Electron Devices.

Since the average beam current is low (10s of nA) the requirement on the klystron power is following from the chosen level of the field gradient.

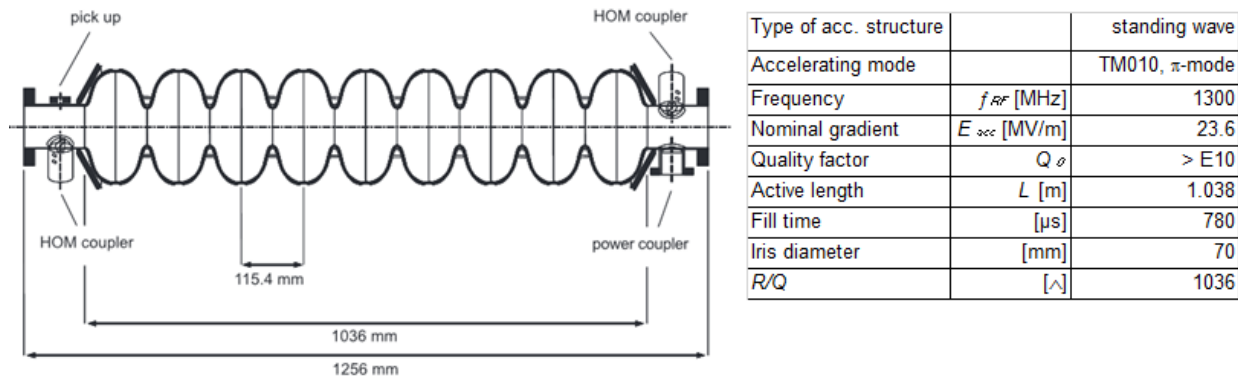


Figure 0-34 European XFEL-type 1.3 GHz linac module with its parameters.

Beam loading from intense bunches in the linac, acceleration of both low-energy and high-energy beams in the same linac structure but 10 μ sec apart will require analytic estimates and simulations to address the performance risks. In contrast to the European XFEL at DESY, or LCLS-2 at SLAC, where the bunch charge is below 1 nC, the eRHIC linac will be accelerating 50 nC in three successive passes.

Since accelerating ~ 50 nC in the 8.6 ps long bunch (RMS) in the DESY 1.3 GHz linac section has never been tested before and may result in strong wake fields we estimated their effects using wake-functions presented in [38]. For the wake we took the following expression:

$$W_t(z) := 41.5 \exp\left(-\sqrt{\frac{z}{d}}\right) \quad (23)$$

in V/pC/m. To get the energy slew along the bunch we convolve it with the Gaussian bunch density distribution normalized to 1:

$$U_g(s) := -Q \cdot \int_{-Ns \cdot s_b}^s W_t(s-t) \cdot \lambda(t) dt \quad (24)$$

in V/m. This function is plotted in Figure 0-35 for the beam parameters corresponding to the Linac 2 on the 2nd pass, i.e. where the beam peak current is near 2 kA while the energy is 9.2 GeV.

For calculating the energy loss we carry out the second integration of $U_g(s)$:

$$\text{TotalLoss1} := -Q \cdot \int_{-Ns \cdot s_b}^{10 \cdot Ns \cdot s_b} \int_{-Ns \cdot s_b}^s W_t(s-t) \cdot \lambda(t) \cdot \lambda(s) dt ds \quad (25)$$

We get 55 MeV of losses due to wakefields in the linac 1 on the 2nd pass.

For calculating the energy chirp we expand $U_g(s)$ into a Taylor series and use the linear term. We get an energy chirp $h = \frac{1}{E} \frac{dE}{dz} = -1.1 \text{ m}^{-1}$. To compensate this energy chirp one needs to run the beam off-crest in the linac 1 by $\phi = 7.6^\circ$, which produces the equivalent energy chirp $h_1 = \frac{E_2}{E} k_{RF} \sin(\phi)$.

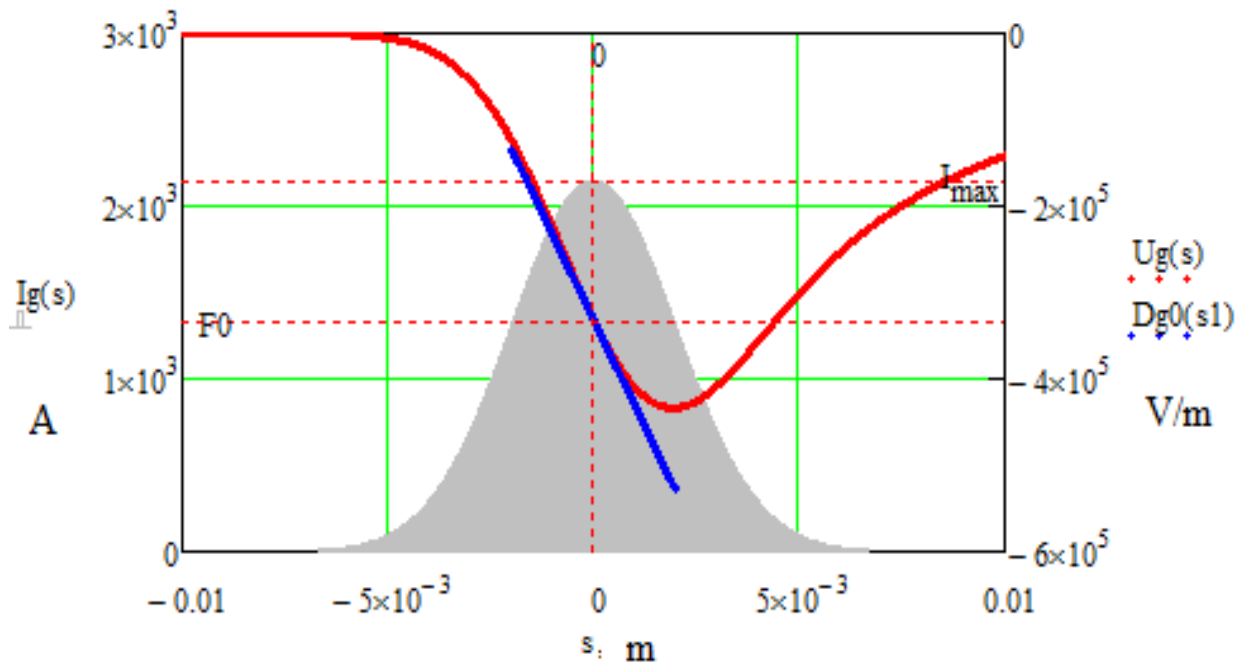


Figure 0-35 Longitudinal energy slew (red curve) along the bunch (grey distribution) per 1 meter of 1.3 GHz accelerating structure. The blue line shows the derivative of the energy slew in the middle

of the bunch, which gives an estimate of the linear energy chirp to be compensated by off-crest acceleration in the linac.

II.12.5 Beam transport

Transport lines (TL) will be designed to deliver the beam between the DR and RF devices and are expected to share the existing RHIC tunnel with both rings. The TL design is focused on getting the longitudinal beam parameters matched with those required at the injection point in the electron storage ring (see Table 0-13).

The beam undergoes acceleration and compression as it runs through the injector. The initial conditions are taken at the DR extraction.

The next steps of the analysis include characterization of 2D longitudinal beam dynamics via simple matrix representation of every element of the injector defined by the vector (ΔE , σ_z , $\Delta\gamma/\gamma$) with following beam 2D beam tracking to account for nonlinearities due to RF wave curvature and high-order transport coefficients in the TLs.

Table 0-13 Longitudinal beam parameters along the eRHIC injector. σ_{in}/σ_{out} is the compression ratio between injector elements.

| | Bunch Length [ps] | Charge [nC] | Energy [MeV] | $\Delta\gamma/\gamma$ [%] | σ_{in}/σ_{out} | I_{peak} [A] | deg. at 1.3GHz |
|--------------------|----------------------|----------------|-----------------|------------------------------|----------------------------|-------------------|-------------------|
| Gun | 2000 | 50 | 0.1 | | | 10.6 | 936 |
| Buncher system | 384.62 | 45 | 10 | 2.50 | 5.2 | 49.8 | 180 |
| Injector linac | 384.62 | 42 | 200 | 0.48 | | 46.5 | 180 |
| Compressor | 85.47 | 40 | | | 4.5 | 199.1 | 40 |
| Damping ring | 72.65 | 40 | 200 | 0.11 | | 234.3 | 34 |
| Chicane 1 | 42.74 | 40 | 200 | | 1.7 | 398.3 | 20 |
| Linac 1, 1 pass | 42.74 | 38 | 3200 | 0.01 | | 378.4 | 20 |
| sextant 2 | | | | | | | 16 |
| Linac 2, 1 pass | 34.19 | 38 | 6200 | 0.01 | | 473.0 | 16 |
| Sextants 3,4,5,6,1 | | | | | | | 4 |
| Linac 1, 2 pass | 8.55 | 38 | 9200 | 0.02 | 4 | 1891.9 | 4 |
| sextant 2 | | | | | | | |
| Linac 2, 2 pass | 8.55 | 36 | 12200 | 0.02 | | 1792.3 | 4 |
| sextants 3,4,5,6,1 | | | | | | | 4 |
| Linac 1, 3 pass | 8.55 | 38 | 15200 | 0.01 | 1 | 1891.9 | 4 |
| sextant 2 | | | | | | | |
| Linac 2, 3 pass | 7.05 | 36 | 18200 | 0.01 | | 2172.5 | 3.3 |
| injection point | 7.05 | 33 | 18200 | 0.02 | | 2003.0 | 3.3 |

II.13 Electron Polarization

II.13.1 Achieving high polarization

The evolution of beam polarization in electron storage rings is defined by two processes related to synchrotron radiation: Sokolov-Ternov self-polarization, and depolarization caused by synchrotron radiation quantum emission. The self-polarization process leads to a slow build-up of electron polarization in the direction opposite to the vertical guiding field, up to a maximum level of 92.4% in an accelerator without spin rotators and with sufficiently weak spin resonances. However, the presence of spin rotators, wigglers, as well as strong spin resonances reduces the achievable polarization level. An important quantity is also the self-polarization time, which has a strong dependence on the beam energy. The self-polarization time for an eRHIC storage ring placed in the present RHIC tunnel is shown in Figure 0-17. It takes into account the split dipole structure which enhances the synchrotron radiation at energies below 10 GeV. Nevertheless the self-polarization time is quite long over the entire energy range, except approaching 18 GeV where it drops to about 30 minutes. This demands a full energy polarized electron injector, so that the electron beam is injected into the storage ring with high polarization ($\sim 85\%$). One benefit of the long self-polarization time is that spin patterns containing bunches of opposite polarization orientation can be efficiently used.

The main challenge of spin dynamics in the storage ring is to preserve the high polarization level of the injected beam, which implies that beam energies must be chosen far from spin resonance conditions. The required timescale of polarization preservation is defined by the time interval between electron beam re-injections. Depolarizing effects are dominated by spin diffusion caused by the quantum nature of synchrotron radiation emission. In the presence of synchrotron radiation

related spin diffusion the equilibrium polarization is described by the Derbenev-Kondratenko formula [39]. The depolarizing time τ_{dpl} is defined by the diffusion rate of the beam energy spread and the sensitivity of the stable spin solution \mathbf{n} to the particle energy:

$$\frac{1}{\tau_{dpl}} \approx \frac{1}{2} \left\langle \left| \gamma \frac{\partial \mathbf{n}}{\partial \gamma} \right|^2 \frac{d \left(\delta \gamma / \gamma \right)^2}{dt} \right\rangle_{\theta} \quad (26)$$

where γ is the relativistic factor and the averaging inside angle brackets is done over the accelerator azimuth θ and, in general, over the beam phase space.

The strength of depolarizing effects generally increases as E^7 , thus making it more difficult to maintain high polarization in storage rings at higher energies. Nonetheless, several accelerators operating above 10 GeV have demonstrated high electron polarization levels exceeding 60% (see Figure 0-36). The accelerator technology used to achieve high polarization at high energies included highly efficient orbit correction, beam-based alignment of Beam Position Monitors relative to quadrupole field centers, and harmonic spin matching [40]. These tools mitigate the effects of imperfection spin resonances and their synchrotron sidebands.

In addition, the intrinsic resonances must be narrow enough to preserve high polarization, at least at energies far enough away from spin resonance conditions. Betatron coupling and unmatched spin rotator insertions can considerably widen the spin resonances, decreasing the achievable polarization. Thorough spin simulation studies have yet to be performed to determine the tolerances on the closed orbit and betatron coupling control, and the required efficiency of spin matching and correction techniques. The eRHIC storage ring uses split dipoles (Section II.3.3) to increase the damping decrement at lower energies. Such wiggler-enhanced synchrotron radiation increases the spin diffusion rate. Thus, careful attention must be paid to the possibility of enhanced depolarization at lower energies. Similarly, the effect of beam-beam interactions on polarization needs attention, since large electron beam tune spreads would effectively widen the intrinsic spin resonances.

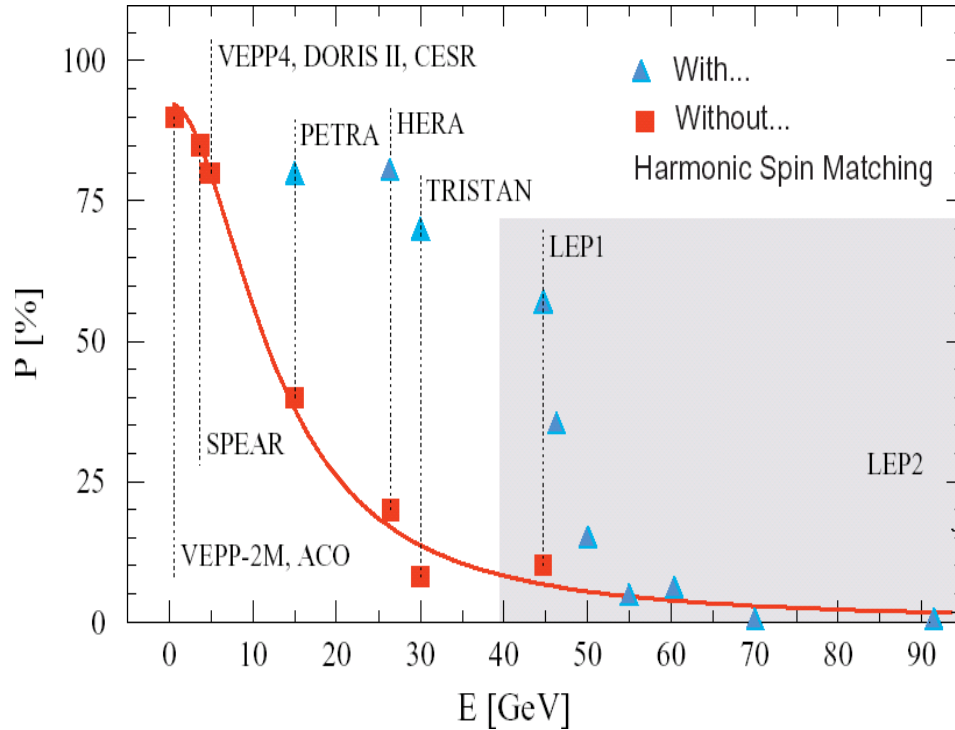


Figure 0-36: Electron polarization levels achieved in various electron storage rings [41].

II.13.2 Spin rotators

Spin rotators are needed to convert the vertical polarization of the electron beam in the arcs to a longitudinal polarization at the experimental detector. The state-of-the-art electron spin rotator that was used in the electron-proton collider HERA (DESY, Germany) [42] employed a 56 m long sequence of interleaved vertical and horizontal dipole magnets to transform the vertical spin of 27 GeV electrons to the required orientation in the horizontal plane. The vertical orbit excursion inside the spin rotator was quite large – about 20 cm – thus requiring some of the rotator magnets to be shifted vertically from the plane of the HERA electron ring.

Spin rotators based on helical magnets have been successfully used for polarized protons in RHIC [43]. The helical magnet design leads to smaller orbit excursion compared with the design based on common dipoles. Helical magnet design of electron spin rotators has been proposed for LHeC [44].

The eRHIC spin rotators must operate over a large energy range, from 5 GeV to 18 GeV. Since the orbit excursion in the dipole magnets (common-type or helical) scales inversely with the beam energy, a HERA-type rotator leads to 1 m orbit excursions of 5 GeV electrons. Furthermore, the synchrotron radiation power (per meter) produced by 18 GeV eRHIC electrons is considerably larger than the 27 GeV electrons in HERA, due to the much larger electron current. Reducing the linear power load requires further increasing the rotator length and, correspondingly, the orbit excursion. Therefore, the most practical solution consists of a spin rotator based on strong solenoid magnets. Solenoidal Siberian Snakes have been used in electron accelerators operating in the 0.5 GeV to 1 GeV range [45].

A solenoid-based scheme for eRHIC using two rotators on each side of the interaction region is shown in Figure 0-37. The combination of rotators (rot1 and rot2) and bending arcs (bend1 and bend2) allows realizing the exact longitudinal orientation of electron spins in the energy range from 5 GeV to 18 GeV. Optimization of solenoidal spin integrals led to the parameters listed in Table 0-14. Figure 0-38 shows the dependence of solenoidal field integrals on the electron energy. The spin rotator will be based on superconducting solenoid magnets with magnetic fields around 7 Tesla. High-temperature superconducting technology might be considered to produce even higher fields.

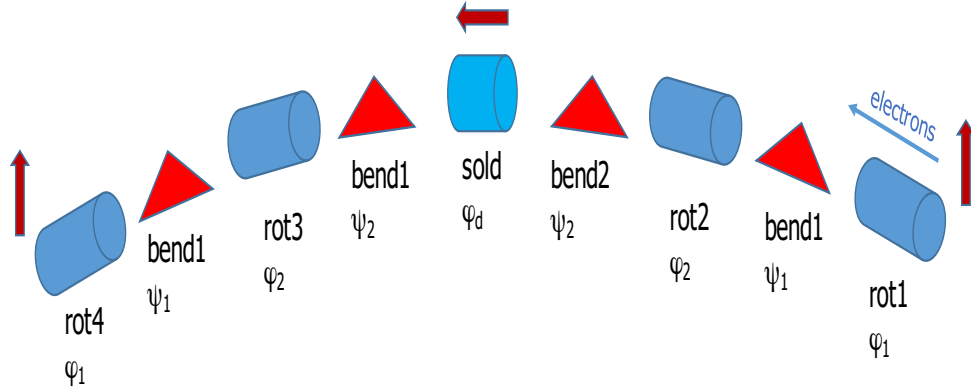


Figure 0-37: Schematic layout of the electron spin rotators.

Table 0-14: Spin rotator parameters.

| Parameter | rot1 | rot2 |
|------------------------------------|-------------------------|------------------|
| Field integral range [Tm] | 2 – 40 | 0 – 127 |
| Solenoid length (at 7 T max field) | 5.7 | 18.1 |
| Bending angle from the IP [mrad] | 92 ($=\psi_1+\psi_2$) | 46 ($=\psi_2$) |
| Location in the RHIC tunnel | D9 – D10 | D6 – Q8 |

Each of the spin rotators, rot1-4, includes two solenoids and several quadrupole and skew quadrupole magnets to compensate for betatron coupling and vertical dispersion, as well as to satisfy, when required, the spin matching conditions. The optics of the rotator insertion on one side of the IR is shown in Figure 0-10. The interaction point is at the right side of the plot. Blue lines are normal quadrupoles, while green lines are skew quads. Blue and light green boxes present dipole bending and solenoidal magnets respectively. The set of β -functions describing this coupled case is given in Mais-Ripken parameterization [46]. Betatron coupling functions and vertical dispersion excursions are limited to the rotator insertions.

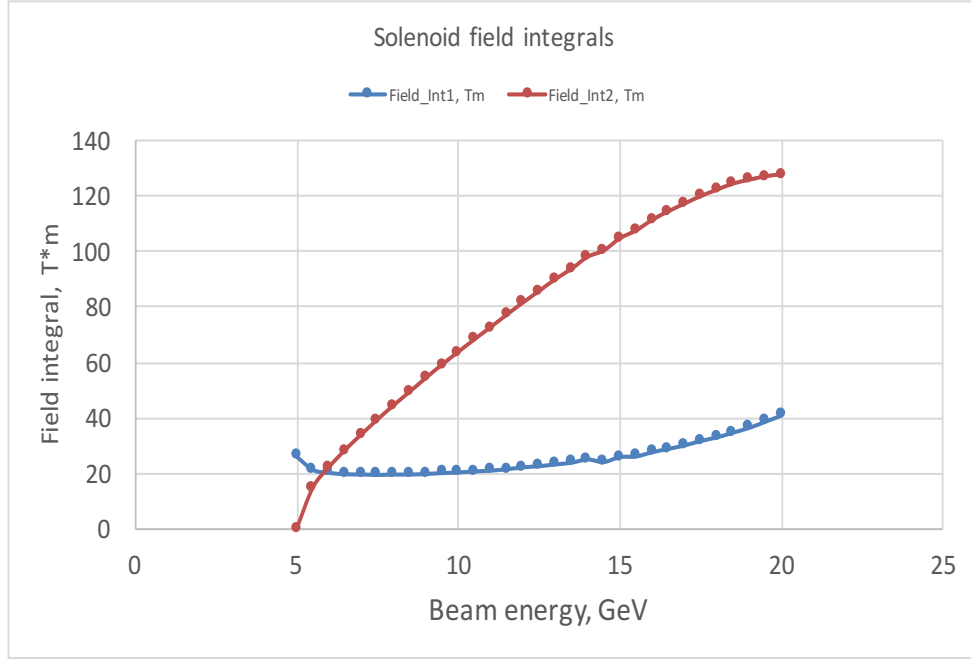


Figure 0-38: Solenoidal field integral of 1st and 2nd rotators.

II.13.3 Spin matching conditions

In order to minimize the depolarization effects caused by synchrotron radiation induced diffusion the spin matching conditions on the rotator optics have to be satisfied. The spin conditions for solenoidal spin rotators can be obtained using general expressions for the function $F_5 = \gamma \partial \mathbf{n} / \partial \gamma$ [47]. Taking into account that the betatron coupling and vertical dispersion are fully compensated for each individual rotator insertion, one obtains the following conditions to nullify $\gamma \partial \mathbf{n} / \partial \gamma$ in the bending arcs of the storage ring outside of the rotator area:

$$\nu_0 H(D') + \sum_{rot:j=1,2} \varphi_j k_{sj} - \nu_0 \sum_{bends:j=1,2} \psi_j k_{yj} = 0 \quad (27)$$

$$H(f_1') = 0 \quad \text{and} \quad H(f_1'^*) = 0 \quad (28)$$

where

$$H(a) = \frac{\varphi_1}{2} (I_{1ent}(a) + I_{1ex}(a)) + \frac{\varphi_2}{2} (I_{2ent}(a) + I_{2ex}(a)) \quad (29)$$

$$I_{nent/ex}(a) = (k_x a_x + k_y a_y)_{nent/ex} \quad (30)$$

Here, $v_0 = G\gamma$ and the solenoidal and bending angles φ_i and ψ_i are as defined in Figure 0-37. Indices x, s, y correspond to horizontal, longitudinal and vertical components. D is the dispersion function and f_l is the eigen function of betatron motion corresponding to the horizontal motion in the arcs with betatron phase advance μ_l . Its components are: $f_{1x} = \sqrt{\beta_{11}}e^{i\mu_1}$ and $f_{1y} = \sqrt{\beta_{12}}e^{i\mu_1}$, where β_{11} and β_{12} through the rotator insertion are shown in Figure 0-37. The functions $I_{l,2}$ are calculated at the entrance and exit of the solenoidal magnets of the first and second rotator, right after or right before the solenoid edge. The spin motion in this formulas is described by components of the spin eigen-vector $k = l - im$, where l and m are spin solutions on the design orbit orthogonal to the stable spin solution n_0 and to each other.

The spin matching conditions are obviously energy dependent, and the first goal is to satisfy them at 18 GeV where, if not taken care of, the depolarization time can be reduced at minimum by factor 3 as compared with the Sokolov-Ternov time. Work on improving the rotator optics for spin matching is underway. We also need to include the effect of the detector solenoid, including induced betatron coupling.

II.13.4 Spin pattern and injectors

To realize arbitrary spin patterns in the electron beam, electron bunches with spins up and down need to be injected into the eRHIC electron storage ring. Assuming that depolarization caused by fluctuations of synchrotron radiation is minimized (that is $\gamma \frac{\partial n}{\partial \gamma} \ll 1$) the depolarization rate is defined by the Sokolov-Ternov time constant shown in Figure 0-17. Above 10 GeV this depolarization affects only bunches with spin “down”, and below 10 GeV it affects all bunches. It gives the timescale on which entire bunches (or bunch trains) need to be replaced on a regular basis.

At the energy of 18 GeV, continuously replacing single bunches with spin “down” at 1 Hz would take 3 minutes. With the Sokolov-Ternov polarization time of about 28 min, the polarization of affected bunches during these 3 minutes changes from -85% to -67%, which is acceptable.

An injector system capable of providing polarized bunches at the required rate can be based on a recirculating linac which can operate in pulsed mode. The injector is described in Section II.12.

II.14 In-situ beam pipe coating and discharge cleaning

To enhance the RHIC luminosity the vacuum chamber resistivity must be lowered and electron cloud formation should be controlled. Solutions are coating the vacuum tube with copper, since stainless steel has high resistivity; and discharge cleaning with high density plasma, since well-scrubbed bare copper can have its peak secondary electron yield reduced to slightly below 1.2. Nevertheless, should experimental testing reveal that discharge cleaning does not reduce the secondary electron yield sufficiently, addition of amorphous carbon coating on top of the copper will be a backup option.

II.14.1 In-situ Beam Pipe Coating

High wall resistivity in accelerators can result in unacceptable levels of resistive heating or in resistive wall induced beam instabilities [48]. This is a concern for the Relativistic Heavy Ion Collider (RHIC) machine, as its vacuum chamber in the cold arcs is made from relatively high resistivity 316LN stainless steel. This effect can be greatly reduced by coating the accelerator vacuum chamber with oxygen-free high conductivity copper (OFHC), which has a conductivity that is three orders [49][50] of magnitude larger than 316LN stainless steel at 4 K. Any coating has to prevent electron cloud formation that has been observed in many accelerators, including RHIC [51][52][53], which can act to limit the machine performance through dynamical beam instabilities and/or associated vacuum pressure degradation.

Formation of electron clouds is a result of electrons bouncing back and forth between surfaces, with acceleration through the beam, which can cause emission of secondary electrons resulting in electron multipacting. Accelerator vacuum chambers and beam pipe surfaces with high enough secondary electron yield (SEY), whose typical maximum value $SEY_{max} > 1.3$, facilitate electron multiplication. Original plans were to add a second coating layer on top of OFHC of TiN or amorphous-Carbon (a-C) to reduce secondary electron yields [54][55]; but later results [56] indicated that amorphous- Carbon (a-C) has lower SEY_{max} than TiN in coated accelerator tubing. Nevertheless, new experimental SEY measurements indicated that there was no need to pursue a-C coating either; since well-scrubbed bare copper can have its SEY_{max} reduced [57] to 1.2. In essence copper coating can resolve the resistivity issue, and after scrubbing can reduce SEY_{max} below 1.3, i.e. detrimental effects of electron clouds can be marginalized.

Applying such coatings to an already constructed machine like RHIC without dismantling it is a rather challenging task due to the small diameter bore of 7.1 cm with access points that are about 500 m apart. A device and technique were developed for *in-situ* coating of the RHIC cold bore vacuum tubes. Experiments proved that the device and technique could successfully be utilized to coat the RHIC cold bore vacuum tubes. But before embarking on the large task of coating RHIC, additional studies are needed to ensure that the expected benefits of coating the RHIC cold bore vacuum tubes with 10 μm of copper are realized. In the non-cryogenic (warm) sections of most accelerators, including RHIC, where high resistivity is not an issue, the electron cloud problem was solved by using non-evaporable getters (NEG) [58].

Since the RHIC geometry is very conducive to cylindrical magnetrons due to the length to radius ratio of the RHIC beam pipe, the choice of a long cylindrical magnetron, similar to that described by A.S. Penfold [59], was made. Ideally, that cylindrical magnetron should be made as long as possible in order to coat sections as long as possible while minimizing or eliminating any need for cathode replacements. The RHIC cold section has a varying curvature with an overall curvature of approximately 1.8 mrad/m, which does not limit the magnetron length. However, mechanical constraint to prevent any sagging does limit the magnetron cathode length to 50 cm.

A 50 cm cathode magnetron mole was developed to in-situ copper coat cold bore RHIC tubes to alleviate unacceptable ohmic heating. The magnetron has a 50 cm long copper cathode, which is shown in Figure II-41. The magnetron is mounted on a carriage with spring loaded wheels that was demonstrated to successfully cross bellows and adjust for variations in vacuum tube diameter, while keeping the magnetron centered. The carriage can also be seen in Figure II-41. Some deposition experiments were performed with spring loaded wheels on both sides of the magnetron, such that a set of wheels rolls over coated areas. No indentation in or damage to coating was observed, i.e. a train like assembly option for coating 500 meter RHIC sections without any interruptions is viable.

Problems that needed to be overcome were developing deposition procedures that result in consistently good adhesion, and maximizing copper utilization. A procedure was formulated for achieving copper coating with excellent adhesion: first is application of a positive voltage of about 1 kV to the magnetron or a separate cleaning anode and to move the discharge down the tube with a pressure of nearly 2 Torr. Second is a conventional deposition process at a pressure of about 5 mTorr.

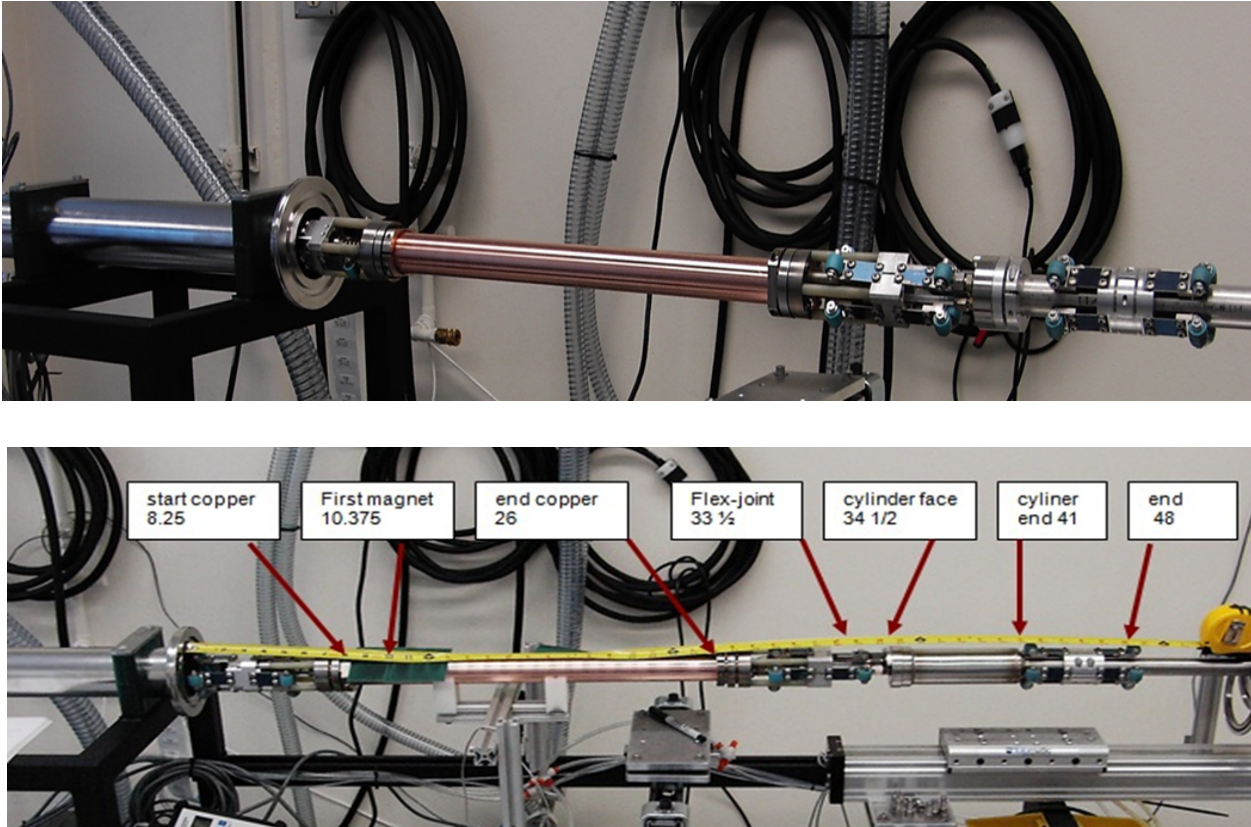


Figure 0-39 Magnetron Coating Mole: Top: 50 cm long cathode magnetron. Bottom: the 50 cm long cathode magnetron assembly; the magnetron carriage has spring loaded guide wheels that crossed bellows and adjusted for diameter variations keeping the magnetron centered.

To maximize copper utilization and minimize reloading needs, a magnetron with moving magnets & thickest possible cathode is used, which reduces the target-to-substrate distance to less than 1.5 cm. The best moving magnetron magnet package moving mechanism was achieved by a miniaturized internal motor.

With the above magnetron mole and procedures, consistent coatings with excellent adhesion are achieved routinely. The optimized results yielded adhesion strength of over 12 kg (maximum capability pull test fixture) or at least $2.9 \times 10^6 \text{ N/m}^2$; and copper utilization reached a remarkable 85%. An assembly of a RHIC magnet tube sandwiched between two types of RHIC bellows

including a shielded bellow with additional sections of RHIC tubing connected to each bellow for a total length of about 20 meters was successfully copper coated. Routine magnetron operation has a coating rate of 3.175×10^{-4} meter/sec in 500 W DC operation. Therefore, it would take 1.57×10^6 seconds or 18.22 days of magnetron sputtering operation to coat a 500-meter-long section of RHIC.

The magnetron assembly was mounted on a carriage (mole) pulled by a cable assembly driven by an external motor. The cable bundle, which is enclosed in 1-inch diameter stranded SS (or braided copper), contains electric power and water cooling feeds, as well as some instrumentation wires. The umbilical spool chamber and cable assembly are under vacuum. Scaling the umbilical motorized spool drive system to a 500 m cable bundle yields a system that is 3 meters or less in any dimension and therefore fits in the RHIC tunnel. The pull cable will be 1/4" diameter stranded SS. This material is very strong (20K tensile) with low elongation.

Room temperature RF resistivity measurements were performed on 32 cm long RHIC stainless steel tubes coated with 2 μm , 5 μm , and 10 μm , thick OFHC with a folded quarter wave resonator structure. Those measurements indicated that for the later 2 coatings conductivity was about 84% of pure copper. Since joints and connectors reduce the experimentally measured Q , the conductivity value of coatings may be even closer to pure solid copper. Computations indicate that 10 μm of copper with 84% of room temperature conductivity will be acceptable for all currently envisioned scenarios.

While the RHIC cryogenic system will be able to handle the increased heat load, reducing this load will reduce operating costs and increase running time. It is therefore worthwhile to consider improving our coating technique to reduce the residual resistance at low temperature. Ion assisted deposition (IAD) has been known to produce deposition with far superior qualities by establishing a gradual transition between the substrate and deposited material resulting in denser, more adherent film, eliminating microstructure and increasing packing densities of optical coatings by an order of magnitude. However, IAD requires simultaneous use of an evaporator and an ion beam source which are too large for use in RHIC.

Future plans are to modify the current deposition system to incorporate IAD; based on a recent breakthrough IAD can be done with End-Hall ion source, which can be miniaturized, and adapted for the mole. To minimize impurities, many of the deposition source components will be fabricated from the metal to be deposited. More details can be found in references [60] and [61].

Additionally, there are two fallback options for lowering the RHIC cold bore resistivity at cryogenic temperatures in case copper coated stainless steel resistivity at cryogenic temperatures remains high even after ion assisted deposition. The two options are:

1. Weaving of a copper wire cage (or ribbons) during deposition; copper deposition adds to conductivity & acts as a glue.
2. A folded cage insertion that opens like an umbrella with disengaging opening mechanism. This may require to modify the mole for spot welding (RSW).

II.14.2 **Copper Scrubbing; in-situ Discharge Cleaning**

Electron clouds, which have been observed in many accelerators [51][52][53], including the Relativistic Heavy Ion Collider (RHIC) at Brookhaven National Laboratory (BNL), can act to limit machine performance through dynamical beam instabilities and/or associated vacuum pressure degradation. Formation of electron clouds is a result of electrons bouncing back and forth between surfaces, which can cause emission of secondary electrons resulting in electron multipacting. The

most effective method to mitigate these effects is proving to be to provide a low secondary electron yield surface within the accelerator vacuum chamber, typically reducing the SEY_{max} to 1.3 or below.

Surface scrubbing of metals is effective in reducing SEY. Extensive studies [57] indicate that SEY is strictly a function of surface condition and independent of temperature. Those studies [57] were performed on copper and aluminum, which showed that well-scrubbed copper can have $SEY=1.2$.

Scrubbing in RHIC is performed with ion beams by filling the rings with 25 GeV proton beams. Short bunches are used to fill RHIC with about 2.2×10^{13} protons, and the increase in pressure is monitored, which can rise to 10^{-7} Torr. However, RHIC scrubbing has not performed satisfactorily as the problem of electron clouds and associated vacuum pressure degradation persists. Surface cleaning by plasmas has been widely used to achieve extremely clean surfaces for many applications [62][63] that include material processing and fusion research. Plasma discharge cleaning has been pursued in accelerators [64][65], though with only limited success at SNS and without success at CEBAF [66].

Conversely discharge cleaning in fusion research devices like tokamaks works extremely well [67][68]. The major purpose of discharge cleaning in tokamaks is to eliminate any possible impurities in fusion plasmas. In hot fusion plasma, heavy impurities can be stripped to high charge state causing large radiated energy loss due to bremsstrahlung. Discharge cleaning in tokamaks is designed, among other reasons, to remove gases adsorbed on vacuum walls. Loosely bound oxygen on walls was shown to be reduced to below 1% of a monolayer[67].

The main reasons for the difference between excellent discharge cleaning results in tokamaks and the need for improvement in accelerators are that the generated discharge cleaning plasmas in tokamaks, for example, properly cover and completely affect every part of every exposed surface, and are of sufficient power and density. Additionally, tokamaks, which are, at first approximation, hollow smooth surface donuts, have adequate pumping with good conductance, while long narrow accelerator tubes have poor pumping conductance.

To ensure effective scrubbing of all surfaces, discharge cleaning with high density plasma is to be performed, i.e. viscous plasma that does not support a large gradient, which reaches all surfaces exposed to vacuum. Normally, the discharge cleaning gas is expected to be argon. In some cases, other gases can be used, e.g. oxygen to remove carbon deposits.

The RHIC cold bore sections have tubes that are 7.1 cm in diameter and access points that are 500 meters apart. Therefore, any microwaves that can be used to discharge clean such a section need to be of a wavelength that is less than 7 cm. Communications & Power Industries Inc. (CPII) for example manufactures [69] gyrotrons having the following frequencies with the respective power: 95 GHz with 30 KW; 110 GHz & 140 GHz with 1MW; 170 GHz with 500 KW; including even higher frequencies at lower power (527 GHz 25 W; 393 & 263 GHz 50 – 100 W). Based on the formula $\lambda = c/f$, 7 cm implies a minimal frequency of 4.3 GHz, while 95 GHz has a wavelength of 0.316 cm (i.e. 3.16 mm). Hence, there are commercially available microwave sources that can satisfy these constraints.

Generating a high density plasma starts in initiation of a low density seed plasma followed by microwave launching and gas density increase. Once the initial plasma is established, microwaves are to be launched from the gyrotron, shown in Figure 0-40, through a waveguide, followed by a Vlasov launcher [70] and a set of mirrors to guide the microwaves into the RHIC tubing. This microwave launching setup converts a TE_{0n} mode to a Gaussian beam. As an example, Figure 0-40 shows a CPII²² VGA 8028 gyrotron that generates a 10 KW 28 GHz TE_{02} mode. Generating plasma between the probes should be done at the Paschen curve minimum. For argon, the product of pressure p and distance between electrodes d is 0.6 Torr cm. For a distance of 500 meters, the

pressure $p=1.2 \times 10^{-5}$ Torr. The Paschen curve is defined for very large plate-like electrodes, whose inter-electrode distance is very small compared to their size. Nevertheless, the above estimate can provide some guidance for establishment of the seed plasma, which is ultimately to be determined by biasing the probes and varying the pressure. Should difficulties in initiating the seed plasma be encountered due to the large distance between the probes, existing beam position monitors (BPMs) or additional probes can be employed to mitigate the problem.

With the microwaves being launched, the vacuum pressure in the tube is then increased to a point above which the microwaves cannot propagate. Cut-off occurs when the plasma frequency, which is given by the formula $f_{pe}=8.98 \times 10^3 n_e^{0.5}$ where f_{pe} is the frequency in Hz and n_e is the electron plasma density in cm^{-3} , reaches the microwave frequency. For example, 95 GHz implies $n_e = 1.1 \times 10^{14} \text{ cm}^{-3}$. In case the plasma is fully ionized, the maximum pressure has to be below 3.1×10^{-3} Torr. These types of plasmas have only a few percent ionization. Thus, maximum discharge cleaning pressure can easily be 10's of mTorr, and with the higher frequency gyrotrons listed above, discharge cleaning pressures can reach 0.1 Torr. Actually, higher pressures are expected, since density to pressure conversion is based on gas being at room temperature. At these pressures sufficient pumping will be necessary. As shown in Figure 0-40, additional pumping, e.g. a roots pump can be added and disconnected by a valve at the end of the discharge cleaning process. Additional high speed vacuum pumping may be necessary to pump on the chamber through which the microwaves are launched. Regardless, a 20-meter long experimental setup similar to Figure 0-40 is to be utilized to test the effectiveness of reducing SEY by discharge cleaning.

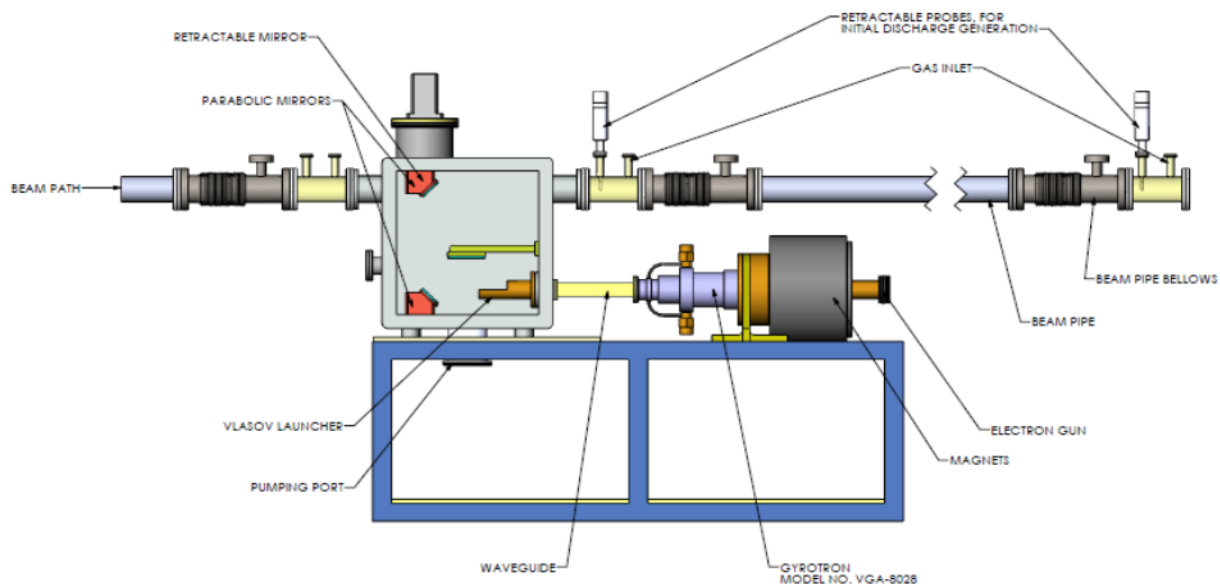


Figure 0-40 Diagram of discharge cleaning arrangement for a RHIC cold bore section.

The microwave power needed for discharge cleaning a 500-meter section of RHIC tubing can be estimated by extrapolating tokamak data. The JFT-2 tokamak [68] was successfully cleaned with CW 2 KW, 2.45 GHz microwave power. That tokamak has a plasma volume of $1.4 \times 10^6 \text{ cm}^3$, and a surface area of $1.1 \times 10^5 \text{ cm}^2$. A 7.1 cm diameter 500 meters of RHIC tubing has a volume of $2 \times 10^6 \text{ cm}^3$ and a surface area of $1 \times 10^6 \text{ cm}^2$. A 20-30 KW microwave discharge in that RHIC tubing can, in principle, approach the JFT-2 plasma cleaning power, a very simplistic extrapolation based on the

fact that the tube and tokamak have comparable volumes, but much larger losses are expected due to the larger surface area of the tube and the lack of a magnetic field, which contains plasma but reduces surface interaction. Nevertheless, a microwave system well below 1 MW suffices for cleaning both of RHIC's rings. The microwave launching arrangement in Figure 0-40 can be setup permanently in a dedicated warm beam pipe section and be available for use after every opening, vacuum break, or any contamination. All components inserted during discharge cleaning are retractable.

II.15 Path to Luminosity Upgrade

It is desirable to increase the luminosity of the eRHIC facility beyond the performance level outlined in this document. As described in Section II.2.1 luminosity levels up to roughly $2 \times 10^{33} \text{ cm}^{-2} \text{ sec}^{-1}$ can be achieved by lowering the horizontal β -function at the interaction point, thus reducing the lower limit on the detectable transverse momentum of scattered protons. This may be acceptable when the momentum distribution of the protons and presence of dispersion are included.

The next upgrade would double the numbers of bunches at all energies to 660. The number of protons per bunch would remain the same at all energies. The number of electrons per bunch might need to be reduced to constrain the total RF power to 10 MW. The luminosity would be increased by a factor somewhat less than two. In the highest energy case, the number of electrons would be halved to keep the synchrotron radiation at 10 MW. As in the Baseline, proton beam cooling is not necessary due to the same long IBS growth times ($\tau_{\text{IBS}} > 7$ hours).

Beyond this intermediate step, upgrading the luminosity to the $10^{34} \text{ cm}^{-2} \text{ sec}^{-1}$ level requires major modifications to the machine. Two possible scenarios are being envisioned, a ring-ring option and an ERL-ring scheme. The ERL-ring upgrade scenario is identical to the Ultimate ERL-ring design as outlined in Section I.5, and requires conversion of the ring-ring electron injector linac to an Energy Recovery Linac (ERL). For this to be cost effective, the same 650 MHz SRF technology has to be chosen for this injector. Furthermore, as described in section I.5, an electron gun capable of providing 50mA of polarized electrons is required, as is Coherent electron Cooling.

The ring-ring upgrade scenario may be thought of as having two conceptual phases. The first, is to lower emittances or raise beam charges to get as many as possible beam-beam tune shifts ζ to their prescribed limits, consistent with the constraints. This increases the luminosity at most energies by a factor up to 3. The IBS times would now be very short requiring active cooling.

The electron bunch charges required to achieve the small proton beam emittances in the ring-ring upgrade scenario are estimated as

$$Q_{\parallel} \propto N_p \frac{\gamma^{2.35} \epsilon^{1.25}}{\beta_{\text{cool}}^{0.5} \delta^{2.5} L_{\text{cool}}} \quad (31)$$

and

$$Q_{\perp} \propto N_p \frac{\gamma^{2.35} \epsilon^{0.3}}{\beta_{\text{cool}}^{0.5} \delta^{0.5} L_{\text{cool}}} \quad (32)$$

where Q_{\parallel} and Q_{\perp} are the required number of cooling electrons for longitudinal and transverse cooling respectively, γ and ϵ are the energy and emittance of the beam being cooled, and β_{cool} is the proton β -function in the cooling length L_{cool} , with dimensions in m.

Using these expressions the estimated charges Q_{100m} needed to cool in a 100 m long section of magnetic cooling are calculated. They are approximate estimates that will require later simulations for the individual cases proposed. After just this first conceptual phase the required cooling charge is 150 nC which is uncomfortably high.

The second conceptual phase is to halve all emittances, β s, bunch lengths, and bunch charges, while doubling the number of bunches. This leaves all divergences and beam-beam tune shifts the same, while further doubling the luminosity. The number of bunches is now 1320. It would use the same IR layout, but would require a higher gradient first quadrupole Q1 that would need R&D. Operation at lower temperatures or the use of High temperature Superconductor might be needed.

With these upgraded parameters, the IBS lifetimes are short, down to 0.2 hours, so active cooling is essential. But now, with lower bunch charges and emittances, the magnetic cooling charges are only 62 nC. This is below the 100 nC for which a simulation of a gun and initial acceleration (see Figure 0-41) has shown acceptable emittances. With the large number of bunches, however, the currents are high, and would require energy recovery.

The upgrade parameters for the energy with highest luminosity were included in Table 0-1. Table 0-15 gives upgrade parameters for all energies.

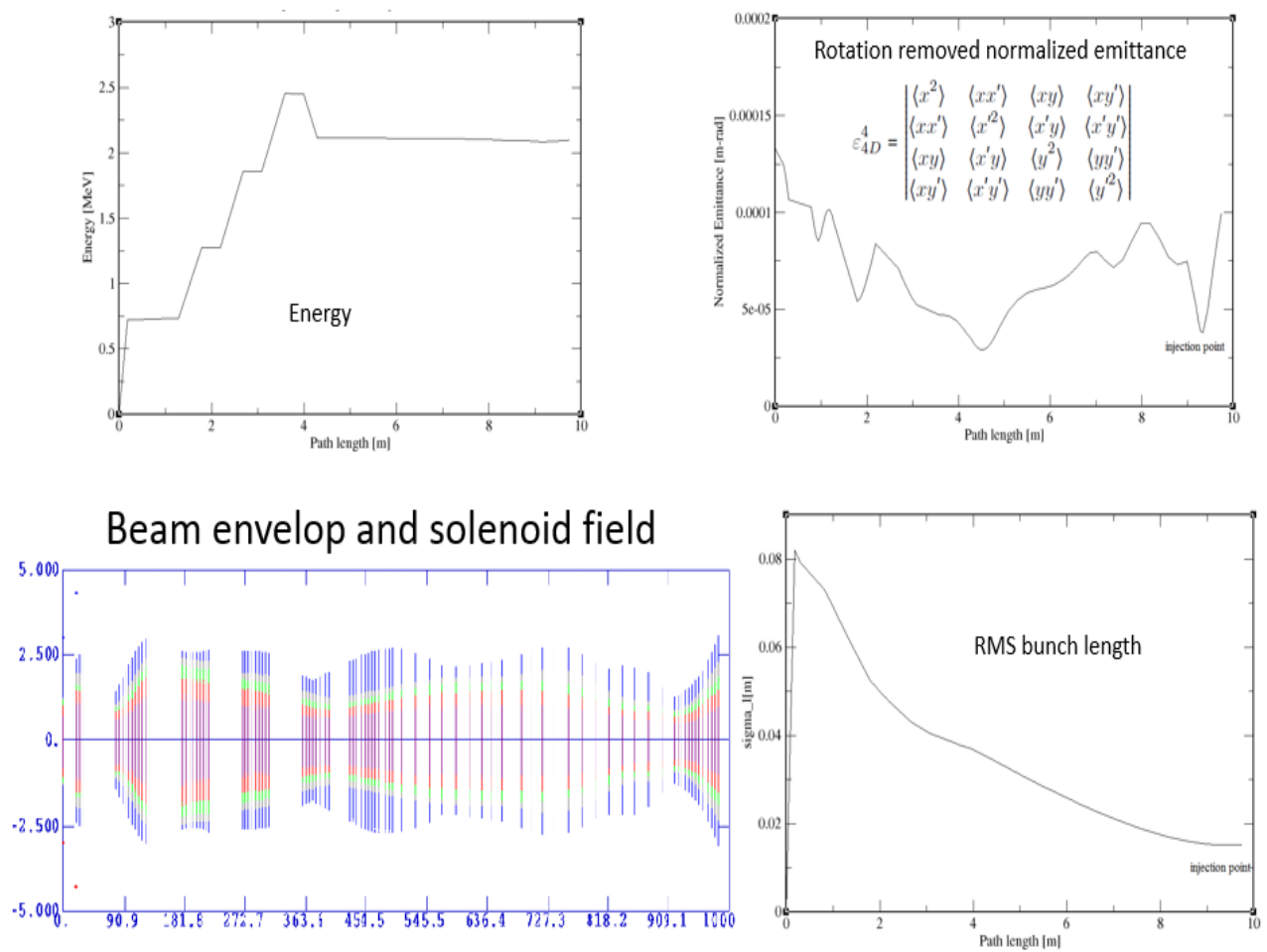


Figure 0-41 Simulation of an electron gun and initial acceleration demonstrating 100 nC electron cooling bunches that meet the requirements.

Table 0-15 Collider Upgrade Parameters.

| | E | N | N_b | ϵ_x | (ϵ_{Nx}) | ϵ_y | (ϵ_{Ny}) | ϵ_x/ϵ_y | β_x | β_y | σ_x | σ_y | σ_x/σ_y |
|------------|-------|---------------|-------|--------------|---------------------|--------------|---------------------|-------------------------|-----------|-----------|-------------------|-------------------|---------------------|
| | [GeV] | [10^{10}] | | [nm] | ([μm]) | [nm] | ([μm]) | | [cm] | [cm] | [μm] | [μm] | |
| \sqrt{s} | 20.0 | | | | | | | | | | | | |
| proton | 30 | 2.3 | 1332 | 43.4 | (1.4) | 28.1 | (0.9) | 1.5 | 111.2 | 17.8 | 220 | 71 | 3.1 |
| electron | 3.3 | 11.0 | 1332 | 26.5 | (173) | 5.36 | (35) | 5.0 | 182.8 | 92.0 | 220 | 70 | 3.1 |
| \sqrt{s} | 29.7 | | | | | | | | | | | | |
| proton | 50 | 4.0 | 1332 | 45.6 | (2.4) | 10.1 | (0.5) | 4.5 | 111.2 | 11.0 | 225 | 33 | 6.7 |
| electron | 4.4 | 15.5 | 1332 | 27.9 | (240) | 3.22 | (28) | 8.7 | 182.8 | 34.1 | 226 | 33 | 6.8 |
| \sqrt{s} | 38.2 | | | | | | | | | | | | |
| proton | 50 | 3.8 | 1332 | 45.6 | (2.4) | 10.1 | (0.5) | 4.5 | 111.2 | 11.0 | 225 | 33 | 6.7 |
| electron | 7.3 | 15.5 | 1332 | 27.9 | (398) | 3.22 | (46) | 8.7 | 182.8 | 34.1 | 226 | 33 | 6.8 |
| \sqrt{s} | 63.4 | | | | | | | | | | | | |
| proton | 100 | 7.5 | 1332 | 22.8 | (2.4) | 5.1 | (0.5) | 4.5 | 111.7 | 5.3 | 160 | 16 | 9.7 |
| electron | 10.1 | 15.4 | 1332 | 19.7 | (388) | 1.73 | (34) | 11.4 | 129.9 | 15.0 | 160 | 16 | 9.9 |
| \sqrt{s} | 77.7 | | | | | | | | | | | | |
| proton | 150 | 7.2 | 1332 | 15.2 | (2.4) | 1.7 | (0.3) | 9.0 | 199.4 | 3.5 | 174 | 8 | 22.5 |
| electron | 10.1 | 15.2 | 1332 | 16.1 | (316) | 0.71 | (14) | 22.8 | 189.7 | 8.2 | 175 | 8 | 23.0 |
| \sqrt{s} | 89.7 | | | | | | | | | | | | |
| proton | 200 | 6.2 | 1332 | 11.4 | (2.4) | 0.8 | (0.2) | 13.5 | 220.1 | 2.6 | 158 | 5 | 33.5 |
| electron | 10.1 | 15.1 | 1332 | 13.9 | (274) | 0.42 | (8) | 32.9 | 181.0 | 5.1 | 159 | 5 | 34.0 |
| \sqrt{s} | 100.2 | | | | | | | | | | | | |
| proton | 250 | 5.6 | 1332 | 9.3 | (2.5) | 0.4 | (0.1) | 22.0 | 283.1 | 2.1 | 162 | 3 | 54.2 |
| electron | 10.1 | 15.2 | 1332 | 12.7 | (250) | 0.24 | (5) | 52.6 | 208.2 | 3.7 | 163 | 3 | 54.5 |
| \sqrt{s} | 140.0 | | | | | | | | | | | | |
| proton | 275 | 7.4 | 1332 | 9.1 | (2.7) | 0.4 | (0.1) | 23.7 | 332.1 | 2.2 | 174 | 3 | 59.9 |
| electron | 17.8 | 1.4 | 1332 | 12.5 | (435) | 0.24 | (8) | 52.6 | 244.2 | 3.9 | 174 | 3 | 57.7 |

Collider Upgrade Parameters (continued)

| | E [GeV] | σ'_x [mrad] | σ'_y [mrad] | ξ_x | ξ_y | Min. p_t [MeV] | ΔQ | σ_s [cm] | I [A] | P_{SR} [MW] | HG [%] | $Lum.$ [$10^{33} \text{ cm}^{-2} \text{ s}^{-1}$] |
|------------|--------------|-----------------------|-----------------------|---------|---------|---------------------|------------|--------------------|------------|------------------|-------------|--|
| \sqrt{s} | 20.0 | | | | | | | | | | | |
| proton | 30 | 0.20 | 0.40 | .015 | .007 | 59 | .071 | 6.5 | 0.38 | | 98 | 0.13 |
| electron | 3.3 | 0.12 | 0.08 | .045 | .071 | | .000 | 0.8 | 1.83 | 0.1 | | |
| \sqrt{s} | 29.7 | | | | | | | | | | | |
| proton | 50 | 0.20 | 0.30 | .014 | .009 | 101 | .076 | 6.5 | 0.68 | | 97 | 0.67 |
| electron | 4.4 | 0.12 | 0.10 | .066 | .085 | | .000 | 0.8 | 2.58 | 0.4 | | |
| \sqrt{s} | 38.2 | | | | | | | | | | | |
| proton | 50 | 0.20 | 0.30 | .014 | .009 | 101 | .070 | 6.5 | 0.63 | | 97 | 0.62 |
| electron | 7.3 | 0.12 | 0.10 | .037 | .047 | | .000 | 0.8 | 2.58 | 2.8 | | |
| \sqrt{s} | 63.4 | | | | | | | | | | | |
| proton | 100 | 0.14 | 0.31 | .014 | .006 | 143 | .038 | 6.0 | 1.25 | | 94 | 3.44 |
| electron | 10.1 | 0.12 | 0.11 | .079 | .092 | | .000 | 0.8 | 2.57 | 10.0 | | |
| \sqrt{s} | 77.7 | | | | | | | | | | | |
| proton | 150 | 0.09 | 0.22 | .015 | .006 | 131 | .039 | 5.0 | 1.20 | | 92 | 6.19 |
| electron | 10.1 | 0.09 | 0.09 | .098 | .099 | | .000 | 0.8 | 2.53 | 9.8 | | |
| \sqrt{s} | 89.7 | | | | | | | | | | | |
| proton | 200 | 0.07 | 0.18 | .015 | .006 | 144 | .031 | 4.5 | 1.03 | | 88 | 9.10 |
| electron | 10.1 | 0.09 | 0.09 | .098 | .096 | | .000 | 0.8 | 2.52 | 9.8 | | |
| \sqrt{s} | 100.2 | | | | | | | | | | | |
| proton | 250 | 0.06 | 0.14 | .015 | .006 | 143 | .032 | 4.0 | 0.93 | | 86 | 12.39 |
| electron | 10.1 | 0.08 | 0.08 | .098 | .095 | | .000 | 0.8 | 2.54 | 9.9 | | |
| \sqrt{s} | 140.0 | | | | | | | | | | | |
| proton | 275 | 0.05 | 0.13 | .001 | .001 | 144 | .036 | 4.0 | 1.23 | | 86 | 1.47 |
| electron | 17.8 | 0.07 | 0.08 | .075 | .066 | | .000 | 0.8 | 0.24 | 9.1 | | |

RF and IBS Upgrade Parameters for 1332 bunches, an RF frequency of 788 MHz, and a crab cavity frequency of 336 MHz.

| γ | $Volts$ [MV] | ϵ_{xN} [μm] | ϵ_{yN} [μm] | σ_z [cm] | dp/p [10^{-4}] | $eV\text{-sec}$ [eVsec] | N_p [10^{11}] | τ_{\parallel} [hr] | τ_{\perp} [hr] | Q_{100m} [nC] | V_1 [MV] | HG [%] | $Lum.$ [10^{33}] |
|----------|-----------------|--------------------------------------|--------------------------------------|--------------------|-------------------------|----------------------------|------------------------|----------------------------|------------------------|--------------------|---------------|-------------|-------------------------|
| 32 | 2.70 | 1.39 | 0.90 | 7 | 14.0 | 0.2 | 0.2 | 3.9 | 3.1 | 0.2 ^a | 4.54 | 98 | 0.13 |
| 53 | 7.87 | 2.43 | 0.54 | 7 | 14.0 | 0.3 | 0.4 | 4.8 | 2.3 | 0.9 ^a | 5.86 | 97 | 0.67 |
| 53 | 7.87 | 2.43 | 0.54 | 7 | 14.0 | 0.3 | 0.4 | 5.1 | 2.5 | 0.8 ^a | 5.86 | 97 | 0.62 |
| 107 | 10.05 | 2.43 | 0.54 | 6 | 9.5 | 0.4 | 0.8 | 2.5 | 1.3 | 8.3 ^a | 8.27 | 94 | 3.44 |
| 160 | 16.23 | 2.43 | 0.27 | 5 | 8.1 | 0.4 | 0.7 | 1.8 | 0.6 | 18 ^b | 7.58 | 92 | 6.19 |
| 213 | 17.91 | 2.43 | 0.18 | 5 | 6.6 | 0.4 | 0.6 | 1.3 | 0.4 | 29 ^b | 8.33 | 88 | 9.10 |
| 266 | 27.60 | 2.48 | 0.11 | 4 | 6.5 | 0.4 | 0.6 | 1.4 | 0.3 | 38 ^b | 8.21 | 86 | 12.39 |
| 293 | 30.40 | 2.67 | 0.11 | 4 | 6.5 | 0.5 | 0.7 | 1.2 | 0.2 | 62 ^b | 7.95 | 86 | 1.47 |

Note:

- a. Non magnetic cooling possible with $\approx 1/3$ charge
- b. Magnetic cooling possible
- c. Only Coherent Electron Cooling possible.

II.16 Risk assessment and mitigation

The leading risks in the ring-ring design are as follows:

1. Crab cavities. Crab cavities are essential in any electron-ion collider design to achieve the required high luminosities while simultaneously allowing the desired detector geometry. They have been successfully used in the electron storage rings of the KEKB B-factory at KEK, Japan, but not in hadron storage rings. A proof-of-principle test with protons is underway in the SPS at CERN, Switzerland, as part of the LHC luminosity upgrade. The finite RF wavelength results in a nonlinear kick along the length of the proton bunches, and therefore a residual offset of the head and tail of that bunch w.r.t. the oncoming electron bunch. This offset may give rise to detrimental synchro-betatron resonances. This risk can be studied in simulations and, if necessary, mitigated by additional higher-harmonic crab cavities, at additional cost.
2. Beam-beam effect. The beam-beam parameters in both the electron and the proton ring of eRHIC have been achieved in e+e- colliders such as the B-factories KEKB and PEP-II, and the hadron-hadron collider RHIC, respectively. However, beam-beam parameters in the only electron-ion collider built so far, HERA at DESY, Germany, were significantly smaller than what is proposed for eRHIC. Simulation studies are underway to address this and demonstrate the feasibility of the proposed parameters. In the event that these beam-beam parameters are unsustainably high, bunch intensities in the oncoming beam have to be reduced. The associated luminosity loss, which is linear in both the proton and the electron bunch intensity, can be partially, but not fully, compensated by increasing the number of bunches in both rings, since the luminosity is proportional to the number of bunches.
3. In-situ RHIC beam pipe copper coating. The three-fold increase of the number of hadron bunches, together with the short bunch length, requires reduction of the resistivity of the stainless steel RHIC beam pipes, and a reduction in secondary electron yield similar to that achieved in the LHC. This can be accomplished by in-situ copper coating. This technique has been successfully demonstrated on a 20 m long beam pipe, resulting in a copper layer that was measured at 85% conductivity of solid copper at room temperature, which is sufficient to reduce the resistive wall cryogenic load at the proposed eRHIC ring-ring parameters to acceptable levels. The risk of a failure in this coating procedure can be mitigated by additional cryo-power, at both additional investment and operating cost.
4. Acceleration of high intensity electron bunches in the injector linac. Rapid bunch replacement in the electron storage ring requires acceleration of high intensity (up to 50 nC) polarized electron bunches in the injector linac. Achieving such high bunch intensities requires accumulation of a small number of bunches from a polarized electron gun in a dedicated accumulation/damping ring at a beam energy around 200 MeV. The transient beam loading effect of accelerating such high intensity bunches in the superconducting injector linac needs to be studied. Alternatively, accumulation in the high energy electron storage ring is being considered. In that scenario, detrimental beam-beam effects as well as detector backgrounds need to be minimized, which can be accomplished by off-energy injection in a dispersive section of the storage ring. To mitigate the risk associated with the polarized high-charge electron gun, we propose to develop and build a prototype to study what performance level is achievable beyond the existing SLC gun at SLAC. The damping ring will be studied in simulations focusing on RF and collective effects. Beam loading

effects in the 1.3 GHz SRF linac can be studied in collaboration with either DESY or FNAL by accelerating high-intensity bunches in their respective existing 1.3 GHz SRF linacs.

5. Electron beam polarization lifetime. In an ideal storage ring the depolarization time of bunches with spin “down” is determined by the Sokolov-Ternov self-polarization time, which in the eRHIC case ranges from 28 minutes to several hours, depending on beam energy. Even at the shortest self-polarization time of 28 minutes, replacing each individual bunch after 6 minutes, which corresponds to an injector linac pulse rate of 1 Hz, is sufficient to maintain an average electron beam polarization of more than 70%. Machine imperfections may reduce the polarization lifetime below the self-polarization time. This can be compensated by a higher repetition rate of the injector complex, thus replacing bunches at a higher rate. Operating the injector at a pulse rate of up to 10 Hz seems feasible at little additional cost.

Bibliography

- [1] arxiv.org/pdf/1212.1701v3.pdf
- [2] National Laboratory for High Energy Physics (KEK). 1995. KEK B-Factory Design Report. Report KEK Report 95-7.
- [3] Stanford Linear Accelerator Center (SLAC). 1993. PEP-II: An Asymmetric B Factory: Conceptual Design Report. Report SLAC-R-418. [doi:10.2172/10112145](https://doi.org/10.2172/10112145)
- [4] J.T. Seeman, SLAC-PUB-14677.
- [5] B. Parker, private communication.
- [6] H. Mais, G. Ripken, *Theory of Coupled Synchro-Betatron Oscillations*, DESY-M 82-05 (1982)
- [7] *The MADX Program*, (2014), <http://mad.home.cern.ch/mad>
- [8] Mane, S. R., Yu. M. Shatunov, and K. Yokoya. 2005. Spin-polarized charged particle beams in high-energy accelerators. Rep. Prog. Phys. 68, pp. 1997–2265. [doi:10.1088/0034-4885/68/9/R01](https://doi.org/10.1088/0034-4885/68/9/R01)
- [9] K. Ohmi, “Simulations of Beam-beam Effects in a Circular e^+e^- Collider”, Phys. Rev. E **62**, 5 (2000).
- [10] K. Ohmi et al. “Response of Colliding Beam-beam System to Harmonic Excitation due to Crab-cavity RF Phase Modulation”, Phys. Rev. ST. Acc. Beams, **14**, 111003 (2011).
- [11] K. Ohmi, F. Zimmermann, “Fundamental beam-beam limit from head-on interaction in the Large Hadron Collider”, Phys. Rev. ST. Acc. Beams, **18**, 121003, (2015)
- [12] J. Qiang, M. Furman, and R. Ryne, “A Parallel Particle-In-Cell Model for Beam-Beam Interactions in High Energy Ring Colliders,” J. Comp. Phys. vol. 198, 278 (2004).
- [13] Y. Hao, Ph.D thesis, “Beam-Beam Interaction Study In ERL Based eRHIC”, Indiana University, 2008.
- [14] R. Li and J. J. Bisognano, Phys. Rev. E 48, 3965 (1993).
- [15] Y. Hao, V. N. Litvinenko and V. Ptitsyn, ‘Study and Mitigation of the Kink Instability in the ERL-based Electron Ion Collider’, Physics Review Special Topics – Accelerators and Beams, 16, 101001 (2013).
- [16] Y. Luo, "SimTrack: a compact c++ code for particle orbit and spin tracking in accelerators", Nuclear Instruments and Methods in Physics Research A 801, 95–103 (2015).
- [17] M. Blaskiewicz PAC07 thpas090 pg 3690 (2007).
<http://accelconf.web.cern.ch/AccelConf/p07/PAPERS/THPAS090.PDF>
- [18] Blaskiewicz, M, Iriso, “How To Use CSEC”, Tech Note C-A/AP/#260 (2006)
<http://public.bnl.gov/docs/cad/Documents/How%20to%20Use%20CSEC.pdf>
- [19] A. Drees et al., “Collimation Experience at RHIC”, HALO '03 conference proceedings, 2003.
- [20] M. Seidel, “The Proton Collimation System of HERA”, DESY HERA 94-103, June 1994.
- [21] U. Schneekloth, “The HERA Luminosity Upgrade”, DESY HERA 98-05, July 1998.
- [22] M. Seidel, “The Upgraded Interaction Regions of HERA”, DESY HERA 00-01, April 2000.
- [23] <https://kds.kek.jp/indico/event/15914/>
- [24] Morita et al, TUPEB011, IPAC2010 p.1536 (2010).
- [25] Q. Wu, I. Ben-Zvi, S. Belomestnykh, R. Calaga, Quarter Wave Crab Cavity Design and Status, Fermilab, IL, CM18/HiLumi Collaboration Meeting, May 7-9, 2012.
- [26] S. Verdu-Andres, et. al., OPTIMIZATION OF THE DOUBLE QUARTER WAVE CRAB CAVITY PROTOTYPE FOR TESTING AT SPS, Proceedings of 16th International Conference on RF Superconductivity, p. 995,
<http://accelconf.web.cern.ch/AccelConf/SRF2013/papers/thp041.pdf>

- [27] F. Carra et. al., CRAB CAVITY AND CRYOMODULE DEVELOPMENT FOR HL-LHC, Proceedings of 17th International Conference on RF Superconductivity, p. 1460, <http://accelconf.web.cern.ch/AccelConf/SRF2015/papers/frba02.pdf>
- [28] B. P. Xiao et al., Design, Prototyping and Testing of a Compact Superconducting Double Quarter Wave Crab Cavity, Phys. Rev. ST Accel. Beams 18, 041004 (2015).
- [29] <http://indico.ihep.ac.cn/event/2825/session/24/contribution/46/material/slides/0.pdf>
- [30] D. Schultz *et al.*, SPAC-PUB-6606, 1994
- [31] J. E. Clendenin *et al.*, SLAC-PUB-9509, 2002
- [32] <http://www.slac.stanford.edu/econf/C000821/MOB20.pdf>
- [33] S. Okuda et al., NIM A318 (1992) 81-84
- [34] M. E. Conde *et al.*, in PR ST AB, Vol. 1, 041302 (1998).
- [35] <http://www.slac.stanford.edu/grp/ad/addr/home.html>
- [36] <http://ieeexplore.ieee.org/stamp/stamp.jsp?tp=&arnumber=72901>
- [37] DESY XFEL TDR, http://xfel.desy.de/technical_information/tdr/tdr/
- [38] T. Weiland and I. Zagorodnov, TESLA Report 2003-19.
- [39] Ya.S. Derbenev and A.M. Kondratenko, Sov. Phys. IJETP 35 2306A (1972).
- [40] R. Assmann et al., EPAC'94, London, p.932 (1994).
- [41] J. Wenninger, as referred in S.R. Mane, Yu. M. Shatunov and K. Yokoya, Report on Progress in Physics 68 1997 (2005).
- [42] D.P. Barber, et al., Phys. Lett. 3434B 436 (1995).
- [43] V. Ptitsyn, Y. Shatunov, NIM A398 126 (1997).
- [44] LHeC Study group, Journal of Phys. G, V.39 N7, p.371 (2012).
- [45] T. Zwart, et al., Proceedings of PAC, Chicago, p.3597.
- [46] I. Borchardt, E. Karantzoulis, H. Mais and G. Ripken, DESY 87-161 (1987).
- [47] V. Ptitsyn, Y. Shatunov, S. Mane, NIM A608 p.225 (2009).
- [48] Covered in many textbooks, e.g. A.W. Chao, "Physics of Collective Beam Instabilities in High Energy accelerators", John Wiley & sons Inc. N. Y. (1993).
- [49] R.P. Reed and A.F. Clark, Editors "Materials at Low Temperatures" American Society of Materials (1983).
- [50] N.J. Simon, E.S. Drexler, and R.P. Reed, "Properties of Copper and Copper Alloys at Low Temperatures", NIST monograph 177, Government Printing Office (1992).
- [51] U. Iriso and S. Peggs, Phys. Rev. ST Accel. Beams 8, 024403 (2005).
- [52] U. Iriso and S. Peggs, Phys. Rev. ST Accel. Beams 9, 071002 (2006)
- [53] W. Fischer M. Blaskiewicz, J. M. Brennan, H. Huang, H.-C. Hseuh, V. Ptitsyn, T. Roser, P. Thieberger, D. Trbojevic, J. Wei, S. Y. Zhang, and U. Iriso, Phys. Rev. ST Accel. Beams 11, 041002 (2008).
- [54] E.L. Garwin, F.K. King, R.E. Kirby, and O. Aita, J. Appl. Phys. 61, 1145 (1987).
- [55] P. Chiggiato, "Surface treatments and coatings for the mitigation of electron clouds", presentation to the 23rd LHC Machine Advisory Committee Meeting, 16 June 2008.
- [56] C. Yin Vallgren, G. Arduini, J. Bauche, S. Calatroni, P. Chiggiato, K. Cornelis, P. Costa Pinto, B. Henrist, E. Métral, H. Neupert, and G. Rumolo, Phys. Rev. ST Accel. Beams 14, 071001 (2011).
- [57] O. Bruning, et al, "Electron Cloud and Beam Scrubbing in the LHC", Proceedings of the 1999, Particle Accelerator Conference, New York, 1999 pp. 2629 – 2631 <http://accelconf.web.cern.ch/accelconf/p99/PROCS.HTM> V. Baglin, I. Collins, B. Henrist, N. Hilleret and G. Vorlaufer, "A Summary of Main Experimental Results Concerning the Secondary Electron Emission of Copper" LHC Project Report 472, CERN CH - 1211 Geneva 23 Switzerland 24 June 2002. Mauro Taborelli, private communication 2012; M. Furman, private communication 2012.

- [58] C. Benvenuti, P. Chiggiato, F. Cicoira, and Y. L' Aminot, J. Vac. Sci. Technol. A **16**, 148 (1998).
- [59] John L. Vossen and Werner Kern Editors, "Thin Film Processes" Academic Press, New York (1978).
- [60] A. Hershcovitch, M. Blaskiewicz, J. M. Brennan, A. Custer, A. Dingus, M. Erickson, W. Fischer, N. Jamshidi, R. Laping, C. J. Liaw, W. Meng, H.J. Poole, R. Todd, "*Plasma sputtering robotic device for in-situ thick coatings of long, small diameter vacuum tubes,*" Physics of Plasmas **22**, 057101 (2015).
- [61] A. Hershcovitch, M. Blaskiewicz, J.M. Brennan, W. Fischer, C-J Liaw, W. Meng, R. Todd. A. Custer, A. Dingus, M. Erickson, N. Jamshidi, and H. J. Poole, "Novel techniques and devices for in-situ film coatings of long, small diameter tubes or elliptical and other surface contours", J. Vac. Sci. Technol. B **33**, 052601 (2015).
- [62] H.F. Dylla, J. Vac. Sci. Technol. A **6**, 1276 (1988).
- [63] J.W. Coburn, IEEE Trans. On Plasma Science 19, 1084 (1991).
- [64] S.-H. Kim, M. T. Crofford, M. Doleans, J. D. Mammoser, and J. Sunders, "R&D Status for In-Situ Plasma Surface Cleaning Of SRF Cavities at Spallation Neutron Source" PAC 2011 proceedings <http://accelconf.web.cern.ch/Accelconf/PAC2011/papers/thocs3.pdf>
- [65] JD Mammoser et al "Large-Volume Resonant Microwave Discharge for Plasma Cleaning of 5 CEBAF 5 Cell SRF Cavity" IPAC 2012 Proceedings.
- [66] Robert Rimmer, private communication (2014).
- [67] L Oren and RJ Taylor NF 17, 1143 (1977).
- [68] Y. Sakamoto et al, J. Nuclear Materials 93-94, 333 (1980).
- [69] <http://www.cpii.com/>
- [70] S.N. Vlasov et al., Radio Eng. Electron. Phys. 20, 14 (1975); Vlasov & Orlova, Radiophys. & Quantum Electron. 17,115 (1975); S.N. Vlasov, M.A. Shapiro, and K.M. Likin, Optical Communications 88, 455 (1992).